Investigation of LDA+U and Hybrid Functional Methods on the Description of the Electronic Structure of $YTiO_3$ under High Pressure

A THESIS

SUBMITTED TO THE COLLEGE OF GRADUATE STUDIES AND RESEARCH

IN PARTIAL FULFILLMENT OF THE REQUIREMENTS

FOR THE DEGREE OF

MASTER OF SCIENCE

IN THE

DEPARTMENT OF PHYSICS AND ENGINEERING PHYSICS

UNIVERSITY OF SASKATCHEWAN

SASKATOON

By

Zhe Song

Abstract

Currently, there are two main methodologies for the calculation of the electronic structure and properties of crystalline solids. Known as the **Hartree-Fock Method (HF)** and the **Density Functional Theory (DFT)** methods**,** they are based on two different theories for the numerical solution of the many electron Schrödinger equation. Unfortunately, in highly correlated electron systems like transition metal complexes, both the HF and DFT methods have severe shortcomings. In some cases they fail to provide the correct description of the electronic structure.

In general, the HF method overestimates the energy band gap due to the neglect of electron correlation effects and the incorrect description of electron interactions in the unoccupied orbitals. In contrast, even though electron correlation effects are implicitly included in the density functional, DFT often underestimates the band gap due to the improper treatment of the electron self-interaction.

To amend these problems, two approaches have been proposed. The deficiency in the HF scheme can be corrected using a hybrid method which adds exchange correlation energy borrowed from DFT to help reduce the band gap energy and bring the predictions in better agreement with experiment. To improve DFT, the LDA+U approach, which uses a model Hubbard-like Hamiltonian including an on-site repulsion parameter U**,** can be employed. This method is a convenient semi-quantitative way to efficiently calculate the band gap of insulators and semiconductors.

In this thesis, the electronic structure of $YTiO_3$ under pressure is investigated using the aforementioned approaches. The performance and reliability of these methods will be examined, compared and discussed.

Acknowledgements

I would like to thank to my supervisor, Professor John S. Tse for his guidance, patience and support throughout this work without which it would have been impossible to complete this work.

I appreciate Dr. Michelle Shaw for her help on Linux, programming and for providing several key references.

I would like to thank Dr. Jianjun Yang for her good suggestions and discussions on the calculations using the VASP program.

I would also like to thank Yansun Yao for his insightful discussions and suggestions.

Contents

Abstract ..... **I**

Acknowledgements ..... **II**

Contents ..... **III**

List of Figures ..... **V**

List of Tables ..... **VII**

Abbreviations ..... **VIII**

Chapter 1 ..... **1**

Introduction **1**

1.1 Theoretical Background 2

1.2 Hartree-Fock Theory 4

1.3 Density Functional Theory 10

1.4 The LDA Theory 13

1.5 The LDA+U Theory 17

1.6 Hybrid Functional Theory 19

1.7 Description of the Project 23

Chapter 2 ..... **27**

Computational Details and Methods of Analysis **27**

2.1 Electronic Band Structure 27

2.2 Density of States (DOS) 29

2.3 Projected Density of States (PDOS) 32

2.4 Crystal Field Theory, High-spin (HS) and Low-spin (LS) States 33

2.4.1 High-spin (HS) and Low-spin (LS) States 35

2.4.2 Spin Unrestricted SCF Formalism 37

Chapter 3 ..... **39**

Electronic Structure of $YTiO_3$ from the LDA+U Method **39**

3.1 The Pseudopotential Approximation 40

3.2 Sampling of *k* points in Reciprocal Space 43

3.3 Optimal U Parameters at Ambient and High Pressures 45

3.4 Total and Projected Density of States 54
3.5 Orbital Ordering 63
3.6 Comparison of Calculated and Experimental Structures 66
Chapter 4 72
Electronic Structure of $YTiO_3$ from the Hybrid Functional Method 72
4.1 Introduction 72
4.2 Computational Details 74
4.3 Optimal Mixing Parameter for the Hybrid Functional Method 77
4.4 Band Structures of High Pressure $YTiO_3$ 80
4.5 Total and Projected Density of States 83
Chapter 5 90
Comparison of LDA+U and Hybrid Functional Methods 90
Chapter 6 97
Summary and Perspectives 97
References 101

List of Figures

Figure 1-1. Coordinate system illustrating the interactions between electrons and nuclei in a multi-particle system. (taken from ref.). 2
Figure 1-2. Comparison between observed band gaps and calculated using B3LYP (data from ref. 2). 22
Figure 2-1. Schematic diagram of the electronic band structure of metals, semiconductors and insulators (taken form http://en.wikipedia.org/wiki/Band_structure). 29
Figure 2-2. Band and DOS of a linear chain of hydrogen atoms (taken from ref. 31). ..30
Figure 2-3. Atomic d orbitals (taken from http://wwwchem.uwimona.edu.jm:1104/courses/CFT.html).....34
Figure 2-4. *d*-orbital splitting under the effects of a crystal field. 35
Figure 2-5. Octahedral splitting of the $[Fe(NO_2)_6]^{3-}$ ion (taken from http://en.wikipedia.org/wiki/Crystal_field_theory).....36
Figure 2-6. Octahedral splitting of the $[FeBr_6]^{3-}$ ion (taken from http://en.wikipedia.org/wiki/Crystal_field_theory).....36
Figure 3-1. Comparison of a wavefuntion in the Coulomb potential of the nucleus (dashed lines) to that of pseudopotential (solid lines). Outside a given radius, r_c, the real and pseudo electron values are identical (taken from http://en.wikipedia.org/wiki/Pseudopotential). 41
Figure 3-2. A perspective view of the structure of $YTiO_3$ at 0 GPa. 46
Figure 3-3. Mid-infrared optical absorption frequency of $YTiO_3$ under pressure at T = 295 K (taken from Ref. 26). 47
Figure 3-4. Comparison of experimental and calculated lattice constants.....48
Figure 3-5. Optimal U parameter with pressures. 51
Figure 3-6. Comparison between calculated and experimental band gaps. 53
Figure 3-7. PDOS of Ti in $YTiO_3$ at 0 GPa using U = 2.700 eV. 55
Figure 3-8. PDOS of Ti in $YTiO_3$ at 8 GPa using U = 2.650 eV. 56
Figure 3-9. PDOS of Ti in $YTiO_3$ at 12 GPa using U = 2.600 eV. 57

Figure 3-10. PDOS of Ti in $YTiO_3$ at 16 GPa using U = 2.500 eV. 58
Figure 3-11. PDOS of Ti in $YTiO_3$ at 25 GPa using U = 2.285 eV. 59
Figure 3-12. PDOS of Ti in $YTiO_3$ at 32 GPa using U = 1.981 eV. 60
Figure 3-13. Total DOS of $YTiO_3$, (a) result from Ref. 46, (b) present calculated result. 62
Figure 3-14. Orientation of the Ti 3*d* orbitals at 0 and 13 GPa (taken from Ref. 26)..... 63
Figure 3-15. Spatial distribution of Ti 3*d* orbitals at different pressure..... 65
Figure 3-16. Experimental x and z fractional coordinates of Y in $YTiO_3$ (from Ref.26). 67
Figure 3-17. x Fractional coordinates of Y atom in $YTiO_3$. 68
Figure 3-18. z Fractional coordinates of Y atom in $YTiO_3$..... 68
Figure 3-19. Ti-O bond lengths in $YTiO_3$. <Ti-O> denotes the average bond length (from Ref. 26). 69
Figure 3-20. Pressure dependence of Ti-O bond lengths in $YTiO_3$. <Ti-O> denotes the average bond length. 70
Figure 4-1. Band structure of $YTiO_3$ obtained from spin restricted DFT calculation. ... 73
Figure 4-2. Band structure using a hybrid B3LYP functional with spin polarized calculation. 73
Figure 4-3. Band gaps calculated with different mixing parameters (A) at 0 GPa (horizontal line indicates the experimental bad gap of 0.66 eV). 78
Figure 4-4. Optimal mixing parameters at different pressure. 79
Figure 4-5. Band Structure of $YTiO_3$ using a mixing parameter A = 0.145 at 0 GPa. ... 80
Figure 4-6. Band Structure of $YTiO_3$ using a mixing parameter A = 0.140 at 8 GPa. ... 81
Figure 4-7. Band Structure of $YTiO_3$ using a mixing parameter A = 0.130 at 16 GPa. . 81
Figure 4-8. Band Structure of $YTiO_3$ using a mixing parameter A = 0.085 at 25 GPa. . 82
Figure 4-9. Calculated band gap at different pressures. 83
Figure 4-10. PDOS of Ti in $YTiO_3$ at 0 GPa using A = 0.145. 85
Figure 4-11. PDOS of Ti in $YTiO_3$ at 8 GPa using A = 0.140. 86
Figure 4-12. PDOS of Ti in $YTiO_3$ at 16 GPa using A = 0.130. 87
Figure 4-13. PDOS of Ti in $YTiO_3$ at 25 GPa using A = 0.085. 88
Figure 6-1. PDOS of NiO for (a) LDA+U, (b) LDA, (c) B3LYP and (d) HF. 98

List of Tables

Table 3-1. Experimental atomic parameters of $YTiO_3$ and standard deviations are given in parentheses (taken from Ref. 44). 45
Table 3-2. Calculated atomic parameters of $YTiO_3$ at 0 GPa. 49
Table 3-3. The optimal U parameters at different pressures. 50
Table 3-4. Band gap comparison for $YTiO_3$. 52
Table 3-5. Electron occupancy of Ti 3*d* t_{2g} below the top of valence band at different pressures. 61
Table 4-1. Definition of variables. 75
Table 4-2. Optimal mixing parameters for $YTiO_3$ at different pressures. 78
Table 4-3. A comparison of calculated and experimental band gap energies at different pressures. 82
Table 4-4. Electron occupancy of Ti 3*d* states at different pressures. 89
Table 5-1. Band widths of Ti-O, lower Ti 3*d* t_{2g} and pseudo-gap below the top of valence band. 92
Table 5-2. Band width of the higher (empty) Ti 3*d* t_{2g} band in the spin-up and spin-down state. 94

Abbreviations

A	Weighting parameter for the Hartree-Fock exchange functional in hybrid functional
AE	All Electron
AO	Atomic Orbital
B3	Becke's 3 parameters method
B3LYP	Becke's 3 parameters method with Lee, Yang and Parr correlation
BF	Bloch Function
CFT	Crystal Field Theory
CO	Crystalline Orbital
CPU	Central Processing Unit
DFT	Density Functional Theory
DMFT	Dynamical Mean Field Theory
DOS	Density of States
GGA	Generalized Gradient Approximation
GGA+U	Generalized Gradient Approximation plus on site Coulomb repulsion method
GTF	Gaussian Type Function
HF	Hartree-Fock
HH	"Half-and-Half" theory
HS	High-spin
LAPW	Linearized Augmented Plane Wave
LDA	Local-density Approximation
LDA+U	Local-density Approximation plus on site Coulomb repulsion method
LFT	Ligand Field Theory
LS	Low spin
LSDA	Local Spin Density Approximation
LSDA+U	Local Spin Density Approximation plus on site Coulomb repulsion method

LYP	Lee, Yang and Parr correlation
PAW	Projector Augmented Wave
PBC	Periodic Boundary Conditions
PBE	Perdew, Bruke and Ernzerhof
PDOS	Projected Density of States
PE	Pentaerythritol
PETN	Pentaerythritol Tetranitrate
PS	Pseudo
PZ	Perdew-Zunger
RDX	Cyclotrimethylene Trinitramine
SIC	Self Interaction Correction
SCF	Self Consistent Field
U	On site Coulomb parameter
US-PP	Ultr-soft Pseudopotential
VASP	Vienna Ab initio Simulation Package
XC	Exchange Correlation
α spin	Spin up
β spin	Spin down

Chapter 1

Introduction

The field of electronic structure calculation is at a momentous stage, with rapid advances in basic theory, new algorithms, computational methods and new computer architectures. Although there are a number of methods that can be used to calculate the electronic structure, they can be grouped into two main approaches, the Hartree-Fock Method (HF), which is commonly used in the Chemistry community, and the Density Functional Theory (DFT), which is more familiar to the Physics community.

Unfortunately, both HF and DFT methods have severe shortcomings for a correct description of the electronic structure of highly correlated systems. The HF method, which neglects electron correlation effects, overemphasizes electron interactions, leading to a wider predicted energy gap between the occupied and conduction bands. Conversely, the DFT ignores self-interaction corrections (SIC) and underestimates the band gap. A well-known example is the failure of DFT to describe NiO as an insulator, erroneously predicting it to be a metal [1]. Therefore, neither method is able to qualitatively and correctly reproduce the electronic structure of highly correlated systems.

Several recent papers [1, 2] have shown that the HF-based methods can be improved substantially with the so-called Hybrid Functional Approach. In essence, the HF Hamiltonian is augmented by introducing an exchange-correlation function computed from the DFT method. However, DFT leads to an underestimation of the band gap due to the improper treatment of electron self-interaction. This tends to

emphasize delocalization of the valence electrons and yields a small gap between occupied and unoccupied states. To amend this problem an *ad hoc* scheme with a semi-empirical correction to the DFT energy functional is introduced to include a model Hamiltonian depending on U – the "on-site" electron-electron (Coulomb) repulsion. This method is known as the LDA+U method.

This work aims to find a theoretical method for the reliable prediction of the energy gap in highly correlated systems. A long term goal is to apply the appropriate method to the investigation of the spin transition (*i.e.,* high-spin (HS) to low-spin (LS) transition) in iron minerals. To achieve this objective, the goal of this project is to explore the electronic properties of $YTiO_3$ at ambient and high pressure. $YTiO_3$ is chosen as a prototype of transition metal oxides due to the considerable experimental and theoretical work already reported. For this reason, this material is ideal for use in a critical evaluation of the ability of different theoretical methodologies to properly describe systems with highly correlated electrons.

1.1 Theoretical Background

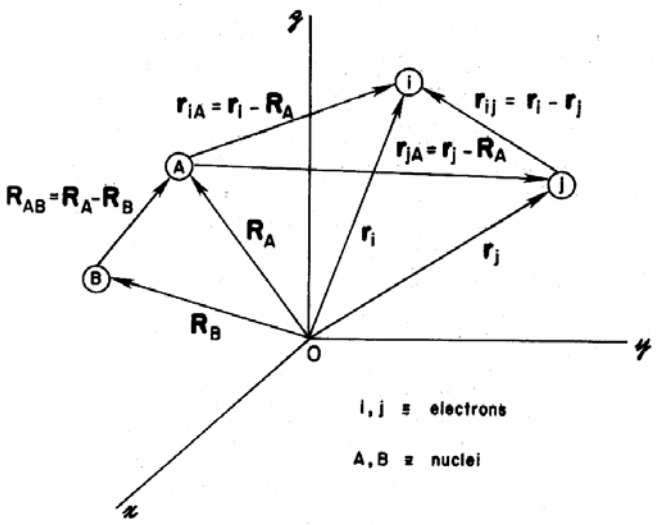

Figure 1-1. Coordinate system illustrating the interactions between electrons and nuclei in a multi-particle system. (taken from ref. 3).

The fundamental equation for non-relativistic description of many-electron system is the Schrödinger equation published in 1926 [4]. It has been applied to multi-electronic atoms and to polyatomic systems such as molecules and solids. Our understanding of the electronic structure of matter is based upon theoretical methods of quantum mechanics. The matter can be unambiguously described as a set of atomic nuclei and electrons interacting via Coulombic and electrostatic forces. Thus the starting point is the Hamiltonian for the system of electrons and nuclei (in cgs unit throughout). The coordinate system is shown in Fig. 1-1.

$$\hat{H} = -\sum_i \frac{\hbar^2}{2m_e}\nabla_i^2 + \sum_{i,I}\frac{Z_I}{|r_i - R_I|} + \frac{1}{2}\sum_{i\neq j}\frac{1}{|r_i - r_j|} - \sum_I \frac{\hbar^2}{2M_I}\nabla_I^2 + \frac{1}{2}\sum_{I\neq J}\frac{Z_I Z_J}{|R_I - R_J|}. \qquad (1.1)$$

Let us define $\hat{T} = -\sum_i \frac{\hbar^2}{2m_e}\nabla_i^2$, $\hat{V}_{ne} = \sum_{i,I}\frac{Z_I}{|r_i - R_I|}$, $\hat{U}_{ee} = \frac{1}{2}\sum_{i\neq j}\frac{1}{|r_i - r_j|}$,

$\hat{T}_n = -\sum_I \frac{\hbar^2}{2M_I}\nabla_I^2$ and $\hat{V}_{nn} = \frac{1}{2}\sum_{I\neq J}\frac{Z_I Z_J}{|R_I - R_J|}$.

The electronic Hamiltonian $\hat{H}_e$ can be abbreviated to

$$\hat{H}_e = \hat{T} + \hat{U}_{ee} + \hat{V}_{ne} = \hat{H} - \hat{T}_n - \hat{V}_{nn}, \qquad (1.2)$$

where electrons are denoted by lower case subscripts and nuclei, with charge Z_I and mass M_I, are denoted by upper case subscripts. Since electrons are fermions, the total electronic wavefunction must be antisymmetric, i.e., it must change sign whenever the coordinates of any two electrons are exchanged. In principle, all properties can be derived with the wavefunctions of the system by solving the time-independent Schrödinger equation,

$$\hat{H}\Psi(R,r) = \varepsilon\Psi(R,r), \qquad (1.3)$$

where ε is the total energy and $\Psi(R,r)$ is the corresponding eigenstate, or wavefunction. Though the antisymmetry in the electronic part is essential, the wavefunction can be symmetric or antisymmetric with respect to exchange of nuclear variables in **R**. The $\mathbf{R} = \{\mathbf{R_1}, \mathbf{R_2},\ldots, \mathbf{R_I}\}$ denotes the set of nuclear coordinates and $\mathbf{r} = \{\mathbf{r_1}, \mathbf{r_1},\ldots,\mathbf{r_i}\}$ denotes the set of i electronic coordinates.

In practice, this problem is intractable to treat within a full quantum mechanical framework. Only in a few cases, such as hydrogenic atoms or the H_2^+ molecule, is a complete analytic solution available. Exact numerical solutions are also limited to a few cases such as atoms and very small molecules. The most important reason for this difficulty is that this is a multi-component many-body system, and the Schrödinger equation which employs the two-body Coulomb interaction, is no longer separable. The presence of an electron in a region of space influences the behavior of the electrons in other regions, so that they cannot be considered as individual entities. In mathematical terms, the wavefunction of a many-electron system cannot simply be written as the product of the wavefunctions of individual electrons. This is the quantum many-body problem. Since solving the Schrödinger equation exactly is impossible, the only practical way is to find approximate solutions.

1.2 Hartree-Fock Theory

The origin of the Hartree-Fock method dates back to the end of the 1920s, soon after the derivation of the Schrödinger equation in 1926. In 1927, Hartree introduced a procedure, called the self-consistent field (SCF) method [5], to calculate approximate wavefunctions and energies for atoms and ions. Hartree was guided by earlier semi-empirical methods of the early 1920s set in the old quantum theory of Bohr. In the Bohr model of the atom, the energy of a state with principal quantum number n is given in atomic units as $E = -1 / n^2$. It was observed from atomic spectra that the energy levels of many-electron atoms were well-described by applying a modified version of

Bohr's formula. By introducing the quantum defect δ as an empirical parameter, the energy levels of a generic atom were well approximated by the formula $E = -1/(n-\delta)^2$. Thus, one could reasonably approximate the transition levels observed in the X-ray region.

Hartree sought a more "first principles" method by approaching the problem from fundamental physical principles. This approach became known as the Hartree method. In 1928 J.C. Slater showed that Hartree's method could be described on a more sound theoretical basis by applying the variational principle and using a trial wavefunction consisting of a product of single-particle functions.

In 1930 Slater and Fock [6] independently pointed out that the Hartree method did not respect the principle of antisymmetry of the wavefunction. Hartree's method used the Pauli exclusion principle in its older formulation, forbidding the presence of two electrons in the same quantum state. However, this was shown to be fundamentally incomplete in its neglect of quantum statistics.

It was then shown that a determinant of one-particle orbitals, called a Slater determinant, trivially satisfied the antisymmetric property of the exact solution and hence was a suitable ansatz for the variational principle. The original Hartree method can then be viewed as an approximation to the Hartree-Fock method without exchange. In 1935 Hartree reformulated the method more suitably for the purposes of calculation.

The Hartree-Fock method, despite its physically more accurate picture, was rarely applied until the advent of electronic computers in the 1950s due to the much greater computational demands over the early Hartree method and empirical models. Initially, both the Hartree and Hartree-Fock methods were applied exclusively to atoms, where the spherical symmetry of the system allowed one to greatly simplify the problem. These approximate methods were (and still are) often used together with the central field approximation, to impose that electrons in the same shell have the same radial part, restricting the variational solution to be a spin eigenfunction. Even so, at the time,

obtaining the solution of the HF equations for a medium sized atom was laborious; small molecules required computational resources far beyond what was available before 1950.

The Hartree-Fock method makes five major simplifications in order to deal with this task,

1. The Born-Oppenheimer approximation is inherently assumed. The full molecular wavefunction is expressed as a function of the coordinates of both nuclei and electrons.

2. Typically, relativistic effects are completely neglected. The momentum operator is assumed to be completely non-relativistic.

3. The variational solution is assumed to be a linear combination of a finite number of basis functions, which are usually (but not always) chosen to be orthogonal. The finite basis set is assumed to be approximately complete.

4. Each energy eigenfunction is assumed to be describable by a single Slater determinant, an antisymmetrized product of one-electron wavefunctions (i.e., orbitals).

5. The mean field approximation is explicitly implied. Effects arising from deviations from this assumption, known as electron correlation, are completely neglected. (Electron correlation should not be confused with electron exchange, which is fully accounted for in the Hartree-Fock method.)

The Hartree-Fock method can be realized through the introduction of a total wavefunction expressed as a product of one electron wavefunctions φ. This approximation assumes that each electron is independent of each other. It is often

referred to as mean-field theory. The total wavefunction of the system is a superposition of each electron wavefunction,

$$\Phi_{HF} = a\prod_i \varphi_i \,, \tag{1.4}$$

where a is the antisymmtrizer. As a result of the Pauli exclusion principle the total wavefunction can be represented by a Slater determinant [7],

$$\Phi_{HF}(x_1, x_2, ..., x_N) = \frac{1}{\sqrt{N!}}\begin{vmatrix} \varphi_1(1) & \varphi_2(1) & \cdots & \varphi_N(1) \\ \varphi_1(2) & \varphi_2(2) & \cdots & \varphi_N(2) \\ \vdots & \vdots & \ddots & \vdots \\ \varphi_1(N) & \varphi_2(N) & \cdots & \varphi_N(N) \end{vmatrix}, \tag{1.5}$$

where $\varphi_i(j)$ refers to the i th one-electron spin orbital, and j indicates the spatial and spin coordinates of electron j condensed in a single variable $x_j = (r_j, \sigma_j)$.

The Hamiltonian for a many-electron system can be represented as

$$\hat{h}_e(R, r) = \sum_{i=1}^{N} \hat{h}_1(i) + \frac{1}{2}\sum_{i=1}^{N}\sum_{j\neq i}^{N} \hat{v}_2(i, j) \,, \tag{1.6}$$

where

$$\hat{h}_1(i) = -\frac{\hbar^2}{2m}\nabla_i^2 + v_{ext}(R, r_i) \tag{1.7}$$

is a one-electron operator, also called the core Hamiltonian, $\hat{h}^{core}$. The $v_{ext}(R, r_i)$ is the external potential, a generalization of the electron-nuclear interaction,

$$\hat{V}_{ne} = \sum_{i,I} \frac{Z_I}{|r_i - R_I|} \,, \tag{1.8}$$

and

$$\hat{v}_2(i, j) = \frac{1}{|r_i - r_j|} \tag{1.9}$$

represents the Coulomb electron-electron interaction.

The Hartree-Fock energy is (given that Φ_{HF} is normalized)

$$E_{HF} = < \Phi_{HF} \mid \hat{h}_e \mid \Phi_{HF} > \tag{1.10}$$

which can be obtained by employing the Variational Theorem. The Variational theorem states that the calculated energy from an approximate wavefunction is always an upper bound to the true energy. Using this procedure a good approximate wavefunction Φ_{HF} can be derived by varying the parameters until the energy is a minimum within a given functional space. The correct one-electron wavefunctions are those which minimize the electronic energy E_{HF}. For molecular or crystal solids, the electronic orbitals can be constructed numerically by solving the Schrödinger equations.

The Hartree-Fock energy can be written in terms of integrals of the one- and two-electron operators as

$$E_{HF} = < \Phi_{HF} \mid \hat{h}_e \mid \Phi_{HF} > = \sum_{i=1}^{N} E_{ii} + \frac{1}{2} \sum_{i=1}^{N} \sum_{j=1}^{N} (\underbrace{J_{ij}}_{Coulomb} - \underbrace{K_{ij}}_{Exchange}) , \tag{1.11}$$

where

$$E_{ii} = \int \varphi_i^*(1) \hat{h}_1(i) \varphi_i(1) dx_1 , \tag{1.12}$$

$$J_{ij} = \iint \varphi_i^*(1) \varphi_j^*(2) \hat{v}_2 \varphi_i(1) \varphi_j(2) dx_1 dx_2 , \tag{1.13}$$

and

$$K_{ij} = \iint \varphi_i(1) \varphi_j^*(1) \hat{v}_2 \varphi_j(2) \varphi_i^*(2) dx_1 dx_2 . \tag{1.14}$$

Here it is noted that the case $i = j$ can be included in the sum because the diagonal Coulomb integrals J_{ii}, corresponding to the self-interaction, are exactly cancelled by the corresponding diagonal exchange integrals K_{ii}.

Equations for the one-electron wavefunctions in the Hartree-Fock approximation are obtained by minimizing E_{HF} with respect to the variation in the orbitals $\varphi_i(r) \rightarrow \varphi_i(r) + \delta\varphi_i(r)$, subject to the orthonormalization constraint of the spin orbitals. The Hartree-Fock equations are given by

$$\hat{F}\varphi_i(x) = \sum_{j=1}^{N} \lambda_{ij}\varphi_j(x)\,, \tag{1.15}$$

where

$$\hat{F} = \hat{h}_1 + \sum_{j=1}^{N} (\hat{J}_j - \hat{K}_j) \tag{1.16}$$

is the Fock operator. The Coulomb $\hat{J}_j$ and exchange $\hat{K}_j$ operators are defined in terms of their action on the spin orbitals,

$$\hat{J}_j\varphi_i(x_2) = \left(\int \varphi_j^*(1)\hat{v}_2(1,2)\varphi_j(1)dx_1\right)\varphi_i(x_2)\,, \tag{1.17}$$

and

$$\hat{K}_j\varphi_i(x_2) = \left(\int \varphi_j^*(1)\hat{v}_2(1,2)\varphi_i(1)dx_1\right)\varphi_j(x_2)\,. \tag{1.18}$$

Equation (1.15) can be solved iteratively. This is commonly known as the self-consistent field (SCF) method.

It is clear that the HF method is a mean field theory and does not contain electron correlations because each electron's wavefunction is only dependent on its own coordinates and is independent of the other electrons.

1.3 Density Functional Theory

The predecessor to density functional theory was the Thomas-Fermi model, developed by Thomas [8] and Fermi [9] in 1927. They used a statistical model to approximate the distribution of electrons in an atom. The mathematical basis used was to postulate that electrons are distributed uniformly in phase space with two electrons in every h^3 of volume. For each volume element d^3r of coordinate space, a sphere of momentum space can be filled up to the fermi momentum p_f,

$$\frac{4}{3}\pi p_f^3(r). \tag{1.19}$$

Equating the number of electrons in coordinate space to that in phase space gives

$$n(r) = \frac{8\pi}{3h^3} p_f^3(r). \tag{1.20}$$

Solving for p_f and substituting in the classical kinetic energy formula then leads directly to the kinetic energy represented as a functional of the electron density,

$$T_{TF}[n] = C_F \int n^{5/3}(r) d^3r. \tag{1.21}$$

This is in fact one of the most important ideas of modern physics, since it is the first introduction of a Local Density Approximation (LDA). When (1.21) is used together with the electron-nuclear attraction energy and the Hartree energy, one obtains the Thomas-Fermi energy,

$$E_{TF}[n] = T_{TF}[n] - Z\int d^3r \frac{n(r)}{|R-r|} + \frac{1}{2}\int d^3r_1 d^3r_2 \frac{n(r_1)n(r_2)}{|r_1 - r|}, \tag{1.22}$$

where Z is the nuclear charge and R is the position vector of the nucleus. For an atom, the total energy functional is then minimized with respect to the density, under the constraint that the spatial integral of the density gives the correct number of electrons.

Density Functional Theory (DFT) is formally exact and in principle does not need assumption of the wavefunction. It is based on the two theorems of Hohenberg-Kohn, which state that all the ground-state properties of a system can be described by the electronic density. The energy functional has its minimum value for the correct ground-state energy for variations in the charge density when the number of electrons is kept fixed. The Hamiltonian in an external potential $V_{ext}(r)$ can be written as

$$\hat{H} = -\frac{\hbar^2}{2m_e}\sum_i \nabla_i^2 + \sum_i V_{ext}(r_i) + \frac{1}{2}\sum_{i\neq j}\frac{1}{|r_i - r_j|}. \qquad (1.23)$$

Hohenberg-Kohn theorems

DFT is based upon two theorems first proved by Hohenberg and Kohn [10]

- **Theorem I**

For any system of interacting particles in an external potential $V_{ext}(r)$, the total energy is determined uniquely, except for a constant, by the ground-state particle density $n_0(r)$.

Corollary I

Since the Hamiltonian is thus fully determined, except for a constant shift of the energy, it follows that the many-body wavefunctions for all electronic states (ground and excited) can be determined. Therefore all properties of the system are completely determined given only the ground-state density $n_0(r)$.

- **Theorem II**

A universal functional for the energy $E[n]$ in terms of the density $n(r)$ can be defined, valid for any external potential $V_{ext}(r)$. For any particular $V_{ext}(r)$, the exact ground-state energy of the system is the global minimum value of this functional, and the density $n(r)$ that minimizes the functional is the exact ground-state density $n_0(r)$.

Corollary II

The functional $E[n]$ alone is sufficient to determine the exact ground-state energy and density.

The proofs of these theorems can be found in [11].

Kohn-Sham Equations

Given an arbitrary N-electron atom or molecule with total electronic density $n(r)$, Kohn and Sham considered a system of N non-interacting electrons in an arbitrary external potential, $V_{ext}(r)$, yielding the same density $n(r)$. Application of the variation on the charge density gives the one-electron density functional equation for each electron. If one assumes that the exchange and correlation are only dependent on the density, a set of equations similar to those from the HF theory can be derived. However, there is one important exception. Since the Coulomb and exchange parts of the energy are computed separately, the self-interactions are not treated properly. The Kohn-Sham Hamiltonian is

$$\hat{H} = -\frac{\hbar^2}{2m_e}\nabla_i^2 + V_{eff}[n] \tag{1.24}$$

and from this one can obtain the one-electron Kohn-Sham equations,

$$\left(-\frac{\hbar^2}{2m_e}\nabla_i^2 + V_{eff}[n]\right)\psi_i(r) = \varepsilon_i\psi_i(r)\,. \tag{1.25}$$

In a similar fashion to the approach used by HF theory, the ground-state energy functional can then be written as

$$E[n] = \int V_{ext}(r)n(r)dr + F[n], \tag{1.26}$$

where *n(r)* denotes ground-state density of the system and

$$\int n(r)dr = N, \tag{1.27}$$

$$F[n] = \iint \frac{n(r)n(r')}{|r-r'|} drdr' + G[n] \tag{1.28}$$

and

$$G[n] = T_{n.i.}[n] + E_{xc}[n]. \tag{1.29}$$

$T_{n.i.}[n]$ is the kinetic energy functional for the system of non-interacting electrons and $E_{xc}[n]$ is called the exchange and correlation energy of the interacting system of density *n(r)*.

In the DFT method, the Coulomb and exchange contributions (see eqs. 1.17 and 1.18) to the total energy are computed separately. Moreover, the exchange term is dependent on the electron density *n*, so that the self-interaction correction is not cancelled properly. This leads to a reduction in the electronic repulsion energy and therefore results in a smaller band gap.

1.4 The LDA Theory

The Hohenberg-Kohn theorem states that the energy of the ground-state of a system of electrons is a functional of the electronic density. In particular, the exchange and correlation energy is also a functional of the density (this energy can be seen as the

quantum part of the electron-electron interaction). This XC functional is not known exactly and must be approximated.

The local-density approximation (LDA) is the first approximation of the exchange-correlation (XC) energy functional in DFT. The basic assumption is that the XC energy of an electron in an interacting homogeneous electron gas of a density is equivalent to the density of the electron in the system being calculated. This approximation was first applied to DFT by Kohn and Sham in an early paper [12].

LDA is the simplest approximation for this functional, it is *local* in the sense that the electron exchange and correlation energy at any point in space is a functional of the electron density at that point only.

The LDA functional assumes that the per-electron exchange-correlation energy at every point in space is equal to the per-electron exchange-correlation energy of a homogeneous electron gas.

The XC functional is the sum of a correlation functional and an exchange functional,

$$E_{xc} = E_x + E_c \,. \tag{1.30}$$

LDA employs the exchange for the uniform electron gas of a density equal to the density at the point where the exchange is to be evaluated

$$E_x = \int d^3r\, n(r) \left(\frac{-3}{4\pi} \right) \left(3\pi^2 n(r) \right)^{\frac{1}{3}} , \tag{1.31}$$

where *n(r)* is the electron density per unit volume at the point *r* and *e* is the charge of an electron. The first local density approximation to the exchange energy was proposed by Dirac [13],

$$E_{x,Dirac}^{LDA}[n] = C_x \int dr\, n(r)^{4/3}\,, \tag{1.32}$$

where C_x is

$$C_x = -\frac{3}{4}\cdot\left(\frac{3}{\pi}\right)^{1/3} = -0.7386\,. \tag{1.33}$$

In 1951, Slater employed a LDA exchange functional to facilitate calculations within HF method [14]. The Slater exchange potential is

$$V_{x,Slater}^{LDA}[n] = -\frac{3}{2}\alpha\left(\frac{3}{\pi}n(r)\right)^{1/3}\,, \tag{1.34}$$

where α was set equal to 1 in the original prescription and when $\alpha = 2/3$, the Dirac exchange potential is recovered. Thus the formula (1.32) is called Dirac-Slater exchange functional.

The strategy to attack the many-body electronic problem consists of dividing the total energy of an electronic system into several different contributions. Among them, the correlation energy is the main problem. The exact expression of this energy is unknown. The idea is to look for appropriate approximations to the correlation. The natural starting point is the simplest model, i.e., the homogeneous electron gas. The LDA is based upon the exact expression for the exchange energy and various approximations. The numerical correlation energies are fitted to those for the homogeneous electron gas. Wigner was the first to address correlation energy in the context of the homogenous electron gas [15],

$$E_c = -\frac{0.44}{r_s + 7.8}\,, \tag{1.35}$$

where

$$r_s = \left(\frac{3}{4\pi n}\right)^{1/3}\,, \tag{1.36}$$

and n is the electron density and r_s in atomic unit . In 1980, Vosko, Wilk and Nusair (VWN) improved the correlation functional [16]. Through the interpolation of the correlation energy data obtained from Ceperley and Alder [17], the parameterization of the functional was done. The correlation functional is shown as follows,

$$E_c^{VWN}(r_s) = \frac{A}{2}\left[\log\left[\frac{y^2}{Y(y)}\right] + \frac{2b}{Q}\tan^{-1}\left(\frac{Q}{2y+b}\right) - \frac{by_0}{Y(y_0)}\left\{\log\left[\frac{(y-y_0)^2}{Y(y)}\right] + \frac{2(b+2y_0)}{Q}\tan^{-1}\left(\frac{Q}{2y+b}\right)\right\}\right], \quad (1.37)$$

where $y = r_s^{1/2}$, $Y(y) = y^2 + by + c$, $Q = (4c - b^2)^{1/2}$, $y_0 = -0.10498$, $b = 3.72744$, $c = 12.93532$ and $A = 0.0621814$.

In 1981, Perdew and Zunger (PZ) obtained a correlation functional by SIC method [18]. The PZ function is given as follows,

$$E_c^{PZ} = \begin{cases} -0.0480 + 0.0311 n(r_s) - m0.0116 r_s + 0.0020 r_s n(r_s), & r_s < 1 \\ -0.1423/(1 + 1.9529\sqrt{r_s} + M0.3334 r_s), & r_s > 1 \end{cases}. \quad (1.38)$$

The three different forms of the correlation functional described above are called the LDA scheme.

As the LDA approximates the energy of the true density by the energy of a local constant density, it fails in situations where the density undergoes rapid changes, as is the case in molecules. For non-uniform charge densities, the exchange-correlation energy can deviate significantly from the uniform result. This deviation can be expressed in terms of the gradient and higher spatial derivatives of the total charge density. For systems where the charge density is slowly varying, this has proven to be an improvement over the LDA. This is the so-called Generalized Gradient Approximation (GGA) and can be written as

$$E_{xc} = E_{xc}\left[n, \nabla n\right]. \tag{1.39}$$

GGA is an improvement to LDA and is now the *de facto* standard of almost all DFT electronic calculations. It has been implemented in many electronic codes. More accurate GGA functionals have been derived in recent years. A most common GGA functional was proposed in 1996 by Perdew, Burke and Ernzerhof (PBE) [19] by enforcing the exchange and correlation functional to satisfy as many formal properties and limits as possible. The PBE functional is given by the following expressions,

$$E_c^{PBE}[n\uparrow, n\downarrow] = \int d^3 r n[E_c^{\text{hom}}(r_s, \zeta) + H(r_s, \zeta, t)]. \tag{1.40}$$

Here E_c^{hom} is the correlation energy per particle of a uniform electron gas, $\zeta = (n\uparrow - n\downarrow)/n$ is the spin polarization, r_s is the local value of the density parameter, t is a dimensionless gradient $|\nabla n|/(2\phi k_{TF} n)$, $\phi = ((1+\zeta)^{2/3} + (1-\zeta)^{2/3})/2$ and

$$H = \frac{1}{a_0}\gamma\phi^3 \log\left(1 + \frac{\beta}{\gamma}t^2 \frac{1 + At^2}{1 + At^2 + A^2 t^4}\right). \tag{1.41}$$

The a_0 is the Bohr radius, $\beta \simeq 0.066725$, $\gamma = (1 - \ln 2)/\pi^2 \simeq 0.031091$ and

$$A = \frac{\beta}{\gamma}\left[\exp\left(\frac{-E_c^{\text{hom}}}{\gamma\phi^3 / a_0}\right) - 1\right]^{-1}. \tag{1.42}$$

1.5 The LDA+U Theory

The LDA+U method is designed to correct for the neglect of SIC in the LDA theory by an additional Hubbard-like Hamiltonian including on-site interactions. This

model depends on the electron occupancy (n). To first order, the total Hamiltonian becomes [20]

$$E_{DFT+U} = E_{DFT}\left[\rho^{\sigma}\right] + E_{U}\left[\left\{n^{\sigma}_{mm'}\right\}\right], \tag{1.43}$$

where ρ^{σ} is the charge density for spin-σ electrons and $n^{\sigma}_{mm'}$ is the density matrix for correlated electrons (σ is the spin index, m and m$^{'}$ are the magnetic number).

The U-parameter is often treated empirically. For *Fe* systems, it is normally between 3.5 – 5 eV. More recently, a theoretical justification of the DFT+U method has been proposed. It was shown that the U parameter can be treated as the curvature of the DFT total energy [21]

$$U \sim \frac{\partial^2 E_{DFT}}{\partial n^2}. \tag{1.44}$$

Using this scheme, the U parameter, in principle, can be evaluated within DFT directly without any additional approximations.

The essence of the LDA+U method is the assumption that one may write the total energy as

$$E_{tot} = E_{DFT} - E_{dc}\ , \tag{1.45}$$

where the HF like interaction replaces the LDA on-site due to the fact that one subtracts a double counting energy (E_{dc}) which equals the on-site LDA contribution to the total energy.

1.6 Hybrid Functional Theory

Since the HF theory completely neglects the correlation effects, an empirical extension to improve the accuracy is to include some form of correlation energy. The hybrid functional theory is based on the adiabatic connection between the HF and DFT. Applying the adiabatic connection, the exchange correlation energy is given as [22]

$$E_{XC} = \int_0^1 U_{XC}^{\lambda} d\lambda \,, \tag{1.46}$$

where λ "connects" the non-interacting Kohn-Sham reference system (λ = 0) to the fully-interacting systems (λ = 1) through a continuum of partially interacting systems ($0 \le \lambda \le 1$) all of which have the same density *n(r)*. The derivation of this adiabatic connection can be found in [23]. The advantage of the hybrid method is that for a given system, if an optimal coupling parameter λ can be found, it will balance the deficiency inherent in both the HF and DFT methods. The introduction of the Hartree exchange compensates for the neglect of SIC in DFT method. The mixing of DFT functional helps to introduce correlation effects into the Hamiltonian.

The "hybrid" method was first introduced by Becke. It is also known as the "half-and-half" (HH) theory [22]. In Becke's HH theory the exchange-correlation energy is expressed as the sum of half exact-exchange Kohn-Sham theory and half the local spin-density approximation (LSDA) exchange-correlation potential (see formula (1.47)),

$$E_{XC} = 0.5E_X + 0.5U_{XC}^{LSDA} \,. \tag{1.47}$$

In tests of this HH theory on atomic systems, HF orbitals, rather than the true Kohn-Sham orbitals were used. Very encouraging results on atomic exchange-correlation energies, atomization energies and ionization potentials have been obtained. This

simple and powerful relationship between HF and DFT points to a promising new development in the future.

Following this, Becke extended the "hybrid" functional formalism using the 3-parameter exchange-correlation expression, where the parameters were obtained in a semi-empirical manner. This is known as the B3 method [24] (Becke's 3 parameters method). The famous exchange-correlation is shown as follows,

$$E_{XC} = E_{XC}^{LSDA} + a_0(E_X^{exact} - E_X^{LSDA}) + a_X \Delta E_X^{B88} + a_C \Delta E_C^{PW91}, \quad (1.48)$$

where E_X^{exact} is the "exact" exchange energy (equal in value to the conventional Hartree-Fock exchange energy), ΔE_X^{B88} is Becke's 1988 gradient correction (to the LSDA) for exchange, and ΔE_C^{PW91} is the 1991 gradient correction for the correlation described by Perdew and Wang. The optimum values for the parameters which were determined by an appropriate fit to experimental data are

$$a_0 = 0.20, \quad a_X = 0.72, \quad a_C = 0.81.$$

If we substitute ΔE_C^{PW91} with the correlation energy of Lee, Yang and Parr (LYP), one arrives at the so-called B3LYP method. In the B3LYP method, the exchange correlation energy is given by

$$E_{XC} = (1-A)(E_X^{LDA} + BE_X^{BECKE}) + AE_X^{HF} + (1-C)E_C^{VWN} + CE_C^{LYP}. \quad (1.49)$$

Thus, the exchange correlation energy becomes

$$E_{XC} = \underbrace{E_X}_{Exchange} + \underbrace{E_C}_{Correlation}, \quad (1.50)$$

and

$$E_X = (1-A)E_X^{DFT} + AE_X^{HF} \\ = (1-A)(E_X^{LDA} + BE_X^{BECKE}) + AE_X^{HF} \ , \tag{1.51}$$

$$E_C = E_C^{DFT} = (1-C)E_C^{VWN} + CE_C^{LYP} \ . \tag{1.52}$$

Using these hybrid functionals, excellent results on the atomization energies of molecules are found in good accordance with experimental values. This investigation has revealed the important role of the exact exchange. The B3LYP functional is the most successful hybrid functional scheme. For isolated molecules the accuracy of this method rivals that of the most sophisticated HF based correlation methods but at a fraction of the computational expense.

This method has been applied to study the band gaps of a number of solid semiconductors. The results are shown in Figure 1-2. The calculated band gap energies for a fairly large set of insulating and semiconducting compounds using the hybrid B3LYP functional are in very good agreement with experiment. Recently [25], Perger performed hybrid functional calculations of band gaps in the molecular crystals anthracene, pentaerythritol (PE), pentaerythritol tetranitrate (PETN) and cyclotrimethylene trinitramine (RDX). Results of these studies show that the B3LYP hybrid functional can efficiently calculate band gaps for molecular crystals.

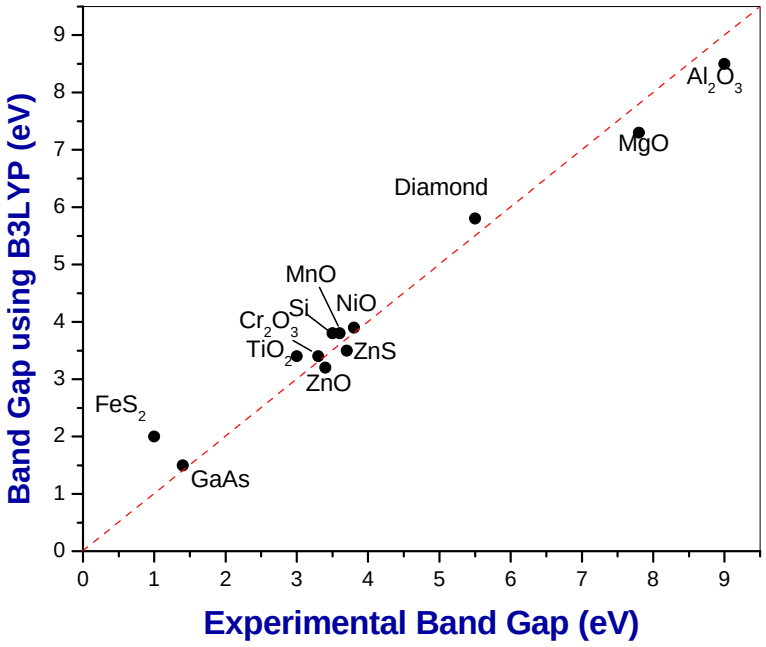

Figure 1-2. Comparison between observed band gaps and calculated using B3LYP (data from ref. 2).

In this study, a more simplified form is employed, where $B = C = 0$. Then the exchange correlation energy becomes

$$E_{XC} = (1-A)E_X^{LDA} + AE_X^{HF} + E_C^{VWN} . \qquad (1.53)$$

The E_{XC} potential is then a simple sum of the individual energy components. By tuning the parameter A between 0 and 1, the progression from pure LDA to pure HF exchange can be followed.

To investigate the role of exact Fock exchange on the description of electronic properties, I. de P.R. Moreira and his collaborators presented another expression for the EX interactions [1],

$$E_{XC} = (1-\delta)E_x^{Slater} + \delta E_x^{HF} + E_{corr}^{LDA} , \qquad (1.54)$$

where the Fock (E_x^{HF}) and Dirac-Slater (E_x^{Slater}) exchange functionals are mixed with the LDA correlation functional (E_{corr}^{LDA}). They employed this hybrid functional method and arrived at the conclusion that ~35% Fock exchange gave good description of structural parameters, magnetic form factors and the band gap [1].

In summary, recent research demonstrates that the hybrid functional method can be a potentially reliable and computationally efficient method to describe the electronic structure of correlated systems. However, the hybrid functional method has not been well tested for transition metal compounds, in particular the metal oxides. Also all the previous studies were focused on systems at ambient pressure without consistent study of the variation of the mixing parameter on a chosen system as a function of pressure. The proposed study will help to expand the scope of hybrid functional methods into this class of materials and investigate variation of the mixing parameter with pressure.

1.7 Description of the Project

The primary objective of this project is to evaluate the performance of the LDA+U and hybrid functional methods for prediction of the electronic structure of highly correlated systems. To this end, $YTiO_3$ was chosen as the test system. There are several reasons for choosing this compound. There is already a large amount of experimental date available in the literature. The electronic properties have been studied with a variety of theoretical techniques. Most importantly, the band gap of $YTiO_3$ as a function of external pressure has been determined from synchrotron infrared experiments [26]. This experimental data is crucial as it offers an unbiased evaluation of the pressure dependence of the electron correlation effects with band gap energies over a wide pressure range. Furthermore, an interesting change in the orbital ordering due to compression has been suggested from the experiment. This possibility will be

investigated. Therefore, $YTiO_3$ contains a wealth of physics and is a suitable system for calibration of the LDA+U and hybrid functional methods.

The electronic structure of $YTiO_3$ has previously been studied by a variety of theoretical methods. A calculation [27] using the full-potential linear augmented plane wave method within the LDA reproduced the experimentally observed ferromagnetism, but erroneously predicted a metallic ground-state. The insulating behavior was attributed to unfounded lattice distortions. Later [28], the electronic structure of $YTiO_3$ was studied using the GGA within the LDA. The calculation failed to reproduce its insulating nature. The band gap only appeared with the introduction of the LDA+U model.

More recently, a calculation [29] on the orbital ordering in $YTiO_3$ at ambient pressure using the local spin-density approximation (LSDA) has been reported. The orbital ordering was found to be in good agreement with the experiment and the HF results. Finally [30], using state-of-the-art dynamical mean-field theory (DMFT), it has been shown that the interplay between correlation effects and cation covalency suppresses orbital fluctuations in $YTiO_3$ and favor the transition to an insulating state. In principle, DMFT is a more exact theory, but the computational effort is significantly more demanding than that of the standard LDA+U and hybrid functional methods.

A disadvantage of the LDA+U method is that the atom-centered Hubbard parameter U needs to be determined empirically. Furthermore, it is not certain whether a unique choice of U is indeed possible. In previous studies employing LDA+U, a constant U parameter was often assumed in the study of high pressure systems. The validity of this assumption has never been tested.

We wish to study the pressure dependence of the empirical parameters, the on-site Coulomb parameter, U, in the LDA+U theory and A, the mixing parameter in the hybrid density functional theory. This will be achieved by fitting the calculated band gap to experiment at select pressures. The magnitudes of U and A are a direct

indication of the importance of electron correlation. It is also important to investigate the consequence of the LDA+U and hybrid functional method in the description of the chemical bonding. The key questions to be addressed are,

1. With a suitable choice of parameters, can the two methods reproduce the correct electronic ground-state?

2. Are there any discernible trends in the U and A parameters with pressure? Can we rationalize these trends?

3. Does the calculated electronic structure of the system depend on the method of computation?

The synopsis of this thesis is as follows,

Chapter 2 presents the computational details and methods of analysis. The concepts of electronic band structure, density of states (DOS), projected density of states (PDOS) and crystal field theory (CFT) are introduced.

In Chapter 3, results from LDA+U calculations are presented and discussed. It has been found that the value of the U parameter decreases with pressure. This trend can be understood as a result of increasing the overlap among neighbouring atoms, which enhances electron delocalization. The LDA+U calculations predicted the metal-insulator transition pressure for $YTiO_3$ is 32 GPa. This is in very good agreement with the extrapolated value obtained from experiment [26]. At zero pressure, fully optimized geometry agrees very well with the experimental structure. However, the LDA+U calculations failed to reproduce the structural anomaly observed at 13 GPa.

Results obtained with the hybrid functional method are presented in Chapter 4. The results show that it is possible to extract an optimal weight (A) for the exact HF exchange at all pressures. The optimal mixing parameter A is found to decrease with

increasing pressure. This trend is due to diminishing HF exchange energy at high pressure. It is significant to note that the estimated band-closure pressure of 32 GPa is the same as that predicted by the LDA+U method and observed in the experiments [26].

Chapter 5 compares the electronic structures of $YTiO_3$ obtained from the LDA+U and hybrid functional methods. The focus is on the analysis of the filled and unfilled Ti 3*d* bands using the calculated density of states. It is shown that even though both methods succeed in reproducing the correct band gap energies, there are significant differences in the description of the nature of chemical bonding.

The thesis ends with a summary and a brief perspective on future work.

Chapter 2

Computational Details and Methods of Analysis

2.1 Electronic Band Structure

The electron band structure describes the range of orbital energies that electrons in a crystalline solid are allowed to occupy. The band structure determines the characteristics of a material, e.g., the electronic and optical properties. The "dispersion" of the energy bands provides information on the nature and strength of chemical bonding. Although, strictly speaking, unfilled (conduction) bands have no real physical meaning, the energy and band profiles often provide valuable information on the nature of excited non-bonding and anti-bonding states.

The formation of energy bands in a crystal can be understood in a qualitative manner from the following discussion. The electrons of a single free-standing atom occupy atomic orbitals, which form a discrete set of energy levels. This produces a number of molecular orbitals proportional to the number of atoms. When a large number of atoms (on the order of 10^{23}) are brought together to form a solid, the number of orbitals becomes exceedingly large and the difference in energy between them becomes very small. The electrons are then filled in the order of increasing energy.

For an insulator or semiconductor, the uppermost occupied band is called the valence band by analogy to the valence electrons of individual atoms. The lowermost unoccupied band is called the conduction band because electrons can be thermally

excited resulting in the flow of current in the material. The energy difference between the uppermost occupied band and the lowest energy conduction band is the band gap energy. Solids with a band gap larger than $k_B T$ (T near room temperature) are called insulators. If the band gap is comparable to $k_B T$, the solid is known as an semiconductor. If there is no band gap in a solid, it has metallic properties. A great deal of information can be extracted from the band structure of a periodic system.

Band dispersion is an indicator of the chemical interactions between atoms in the solid. Mathematically it is defined by the relationship $\varepsilon = \varepsilon(k)$, where k is the electron wave vector. For a crystalline solid, the band dispersions are different for different crystallographic directions and depend on both the crystal symmetry and the nature of the chemical bonding. Another useful quantity is the band width which is a measure of the energy difference between the highest and lowest occupied levels of a given energy band. The width of the band is determined by the overlap between interacting orbitals and the greater the overlap between neighbors, the larger the band width. For example, for strongly covalent systems the dispersion of the valence electron band (i.e., interactions between the valence orbtials of the constituent atoms) is often directional and usually has large band widths. On the contrary, for non-bonding or localized orbitals, the band dispersion and band width are often very small. Therefore, the interactions between atoms in a condensed matter system can easily be characterized from the study of the band dispersions. An illustration of the terminologies and concepts introduced above is depicted in Figure 2-1.

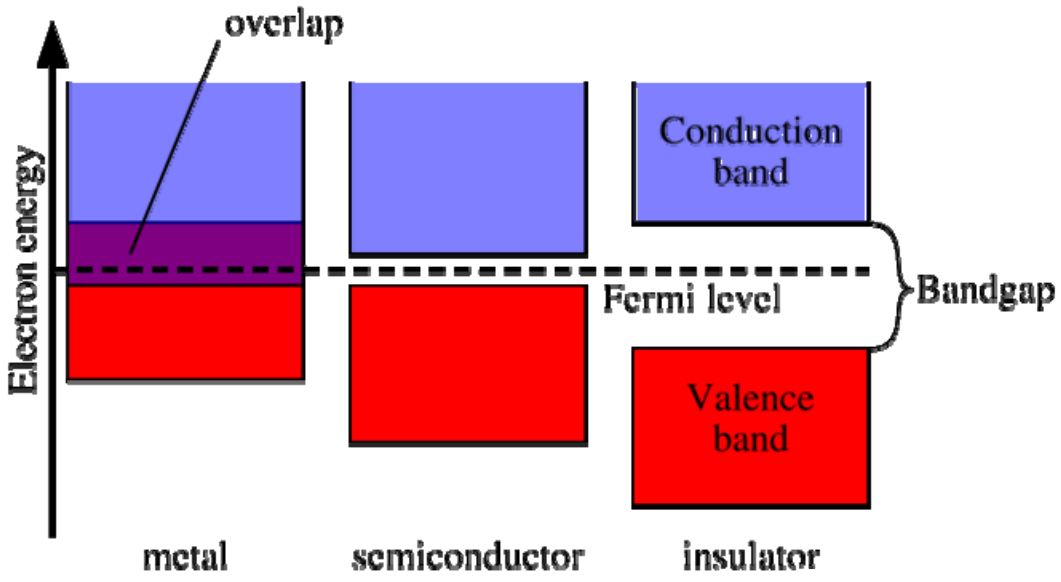

Figure 2-1. Schematic diagram of the electronic band structure of metals, semiconductors and insulators (taken form http://en.wikipedia.org/wiki/Band_structure).

2.2 Density of States (DOS)

Several useful tools have been developed to facilitate the analysis of the electronic structure from a band structure calculation. The density of electronic states (DOS) is defined as,

$$DOS(E)\mathrm{d}E = \text{number of levels between } E \text{ and } E + dE.$$

DOS quantifies how closely packed the energy levels are in a physical system. It is often expressed as a function $g(E)$ of the energy E, or a function $g(k)$ of the wave vector k. It is usually employed to describe the electronic energy levels in a solid. In three dimensions, for example, the density of states in reciprocal space (k-space) is

$$g(k)dk = \frac{V}{2\pi^2}k^2 dk\,, \tag{2.1}$$

where V is the volume of the solid. For a chain of hydrogen atoms, the DOS curve takes on the shape of Figure 2-2

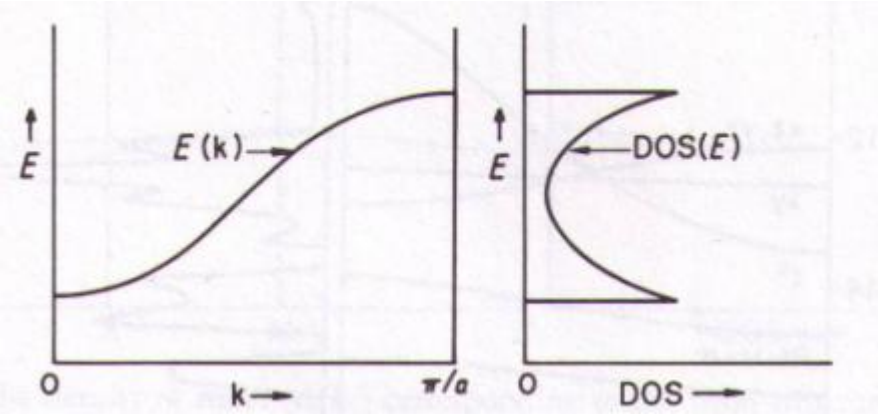

Figure 2-2. Band and DOS of a linear chain of hydrogen atoms (taken from ref. 31).

From Figure 2-2 it is shown that the DOS is proportional to the gradient (*dE(k)/dk*) of *E(k)* with respect to *k*,

$$DOS \propto \left(\left| \frac{dE(k)}{dk} \right|_k \right)^{-1}. \tag{2.2}$$

Therefore, when the gradient is small, the DOS is high conversely and when the gradient is steep, the DOS is low. Small gradients are indicative in localized orbitals (or non-dispersive band, i.e., the orbitals are not strongly interacting). In this case, the close proximity of electrons in a small confined space is a good indication of strong electron correlations and reflected as sharp features in the DOS. As will be illustrated later in this report, this situation is often observed in the *d*-orbitals of transition metal oxides.

To calculate the density of energy states of a particle, the DOS is first computed in reciprocal space (momentum- or *k*-space). The separation between states is fixed by the boundary conditions. For free electrons and photons within a box of size *L*, and for electrons inside a crystal lattice with lattice constant *L*, periodic Born-von Karman boundary conditions can be applied. Using the free particle wavefunction of a plane wave this implies

$$\Psi(x) = \Psi(x+L)\,, \tag{2.3}$$

$$e^{ikx} = e^{ik(x+L)}\,, \tag{2.4}$$

$$1 = e^{ikL}\,, \tag{2.5}$$

$$2\pi n = kL \tag{2.6}$$

and

$$\frac{2\pi}{L} = \Delta k\,, \tag{2.7}$$

where n is any integer and $\triangle k$ is the separation of different k states.

The total number of *k*-states available to a particle is the volume of *k*-space accessible to it divided by the volume of a single *k*-state. The volume accessible is simply the integral from $k = 0$ to $k = k$, and the volume of a k-state is $(\triangle k)^m$ (m is the number of dimension).

In 3-dimension it is given by

$$G(k) = \frac{1}{(\Delta k)^3}\int_0^k d^3k\,. \tag{2.8}$$

These expressions can then be differentiated with respect to k to give the DOS at a given k value,

$$g(k)dk = \frac{dG(k)}{dk}dk\,. \tag{2.9}$$

To find the density of energy states, the relation between energy and momentum for a particular particle is used, and k and dk in $g(k)dk$ are expressed in terms of E and dE. For example a free electron,

$$E = \frac{p^2}{2m} = \frac{(\hbar k)^2}{2m} \tag{2.10}$$

and

$$dE = \frac{\hbar^2 k}{m} dk \,. \tag{2.11}$$

This gives a DOS at energy E per unit volume,

$$g(E) = \frac{d}{dk}\left(\frac{\int_0^k d^3k}{(\Delta k)^3} \right) \frac{dk}{dE} \,. \tag{2.12}$$

2.3 Projected Density of States (PDOS)

Another useful tool is the Projected Density of States (PDOS). The PDOS is defined as the projection of the total DOS into the atom contributions and sometimes even into the contribution of individual atomic orbitals. PDOS is useful to determine the nature of the electronic interaction. Therefore, an energy band can be partitioned into the contributions from the relevant atomic orbtials. For instance, to identify localized *d*-states of a transition metal compound, one often searches for narrow and sharp DOS which have mainly *d*-character. Conversely, highly dispersive bands (i.e., strong overlap between the orbtials of neighbors) will give a broad feature in the DOS with the PDOS comprised of contributions for a large number of orbitals from different atoms. The PDOS can be further decomposed into the different angular momentum

components of the atomic orbitals. Thus in transition metal oxides, the contribution from individual *d*-orbitals (*i.e.,* d_{z^2}, $d_{x^2-y^2}$, d_{xy}, d_{yz}, d_{xz}) can be computed separately. The integration of the PDOS of individual atoms or orbitals gives the occupancy. From the examination of the occupancy of the relevant orbitals, orbital ordering, i.e., the order of occupancy of the orbitals, can be determined. This is the central theme of this research.

2.4 Crystal Field Theory, High-spin (HS) and Low-spin (LS) States

Crystal Field Theory (CFT) is a model that describes the electronic structure of transition metal compounds. CFT successfully accounts for some magnetic properties, colors, hydration enthalpies, and spinel structures of transition metal complexes, but it does not attempt to describe bonding. CFT was developed by physicists Hans Bethe [32] and John Hasbrouck van Vleck [33,34] in the 1930s. CFT was subsequently combined with molecular orbital theory to form the more realistic ligand field theory (LFT) [35], which delivers insight into the process of chemical bonding in transition metal complexes.

The interaction between a transition metal and the attached ligands arises from the attraction between the positively charged metal cation and the negative charge on the non-bonding electrons of the ligand. CFT was developed by considering energy changes of the five degenerate *d*-orbitals (in a free atom) upon being surrounded by an array of point charges consisting of the ligands. As a ligand approaches the metal ion, the electrons from the ligand will be closer to some of the *d*-orbitals and farther away from others causing a loss of degeneracy. The electrons in the *d*-orbitals and those in the ligand repel each other due to repulsion between like charges. Thus the *d*-electrons closer to the ligands will have a higher energy than those further away, resulting in a

lifting of the degeneracy and subsequent splitting of the *d*-orbitals to several levels with different energies.

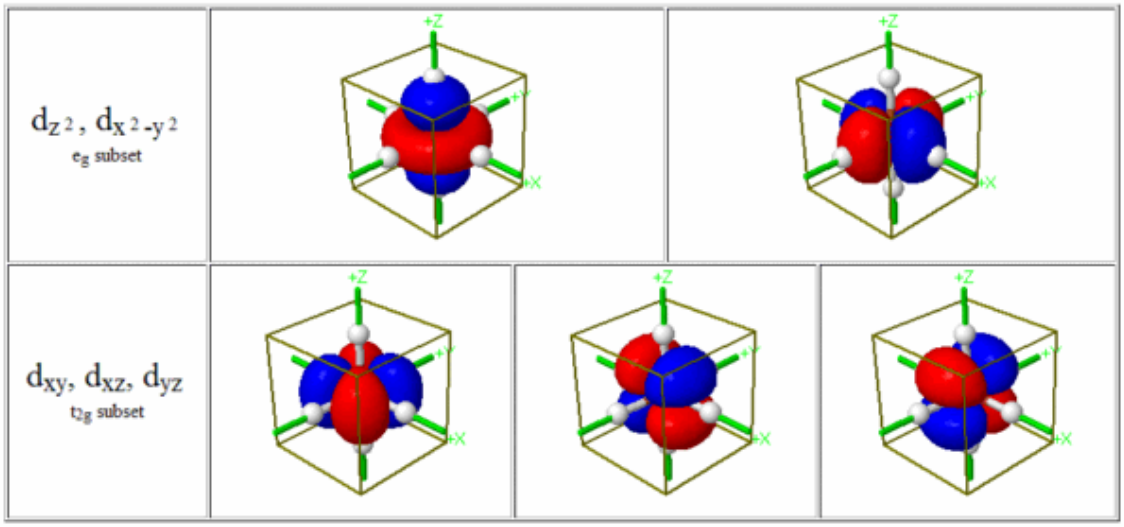

Figure 2-3. Atomic d orbitals (taken from http://wwwchem.uwimona.edu.jm:1104/courses/CFT.html).

In octahedral symmetry (six ligands forming an octahedron around the metal ion), the 5 *d*-orbitals split into two sets, i.e., t_{2g} and e_g, with an energy difference of Δ_{oct}. In the coordinate system shown here, the d_{z^2} and $d_{x^2-y^2}$ orbitals (e_g set) point directly towards the ligand and should have higher energy than the d_{xy}, d_{xz} and d_{yz} (t_{2g}) orbitals. Conversely, in tetrahedral symmetry (four ligands form a tetrahedron around the metal ion), the 5 *d*-orbitals again split into two groups, with an energy difference of Δ_{tet}. The lower energy orbitals will be d_{z^2} and $d_{x^2-y^2}$, and the higher energy orbitals will be d_{xy}, d_{xz} and d_{yz}. It is just the opposite to the octahedral case. Since the ligand electrons in tetrahedral symmetry are not oriented directly towards the *d*-orbitals, the energy splitting will be lower than in the octahedral case.

If the local geometry around the metal ion is not perfectly octahedral, e.g., if there is a tetragonal distortion, the metal-ligand distance in the axial direction will be different from that in the equatorial plane. In this case, the degeneracy will be further

reduced and the t_{2g} set will split into e_g and a_{1g} orbtials. In general, the lower the symmetry, the less degenerate the *d*-orbitals become. However, in a slightly distorted octahedral system, the separation of the degenerate energy levels is still much smaller than the crystal field (Δ_{oct}) and it is still appropriate to describe the splitting of the transition metal *d*-orbitals into the t_{2g} and e_g bands.

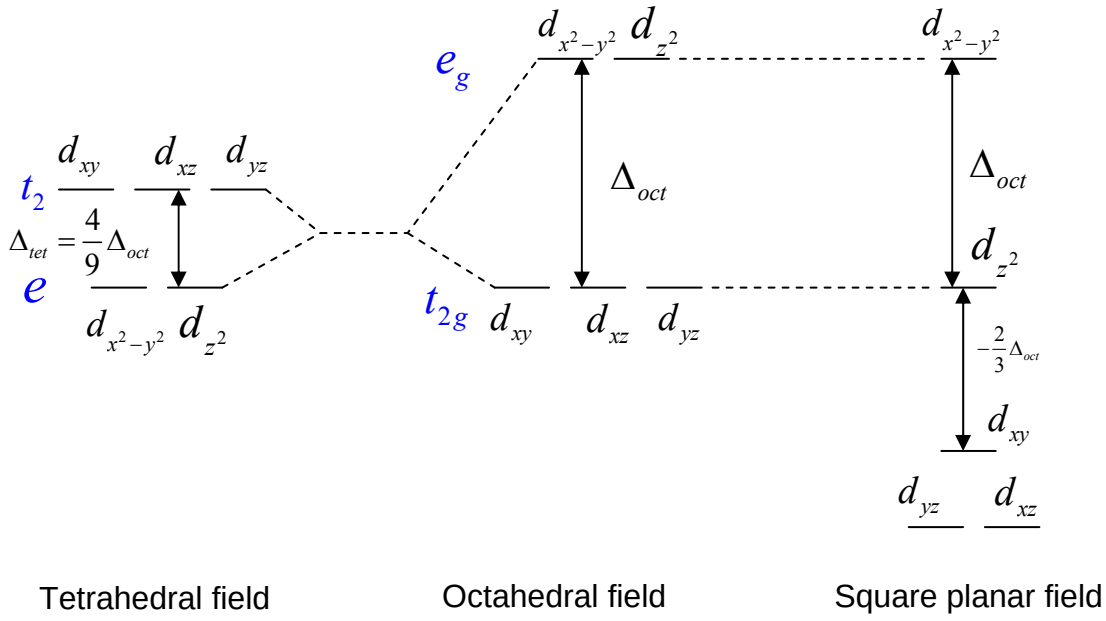

Figure 2-4. *d*-orbital splitting under the effects of a crystal field.

2.4.1 High-spin (HS) and Low-spin (LS) States

Ligands like CN^- and CO which cause a large splitting Δ of the *d* orbitals are referred to as strong-field ligands. In complexes with these ligands, the upper set of orbitals is very high in energy and as such it is unfavourable to populate electrons into them. Therefore, the lower set of orbitals is completely filled before population of the upper set starts - the Aufbau rule is obeyed. Complexes such as this are called LS. For example, NO_2^- is a strong-field ligand and produces a large Δ. The $[Fe(NO_2)_6]^{3-}$ ion has five *d*-electrons and would have an octahedral splitting diagram when electrons are spin-paired leaving a singly occupied orbital.

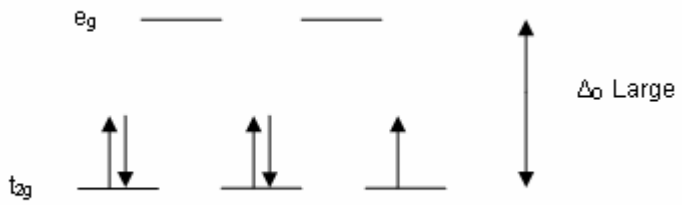

Figure 2-5. Octahedral splitting of the $[Fe(NO_2)_6]^{3-}$ ion (taken from http://en.wikipedia.org/wiki/Crystal_field_theory).

Conversely, ligands (like I^- and Br^-) which cause a small splitting Δ of the *d* orbitals are referred to as weak-field ligands. In this case, it is energetically preferable for the electrons to populate the higher energy set of orbitals first, rather than pairing up in the low-energy orbitals. This occurs because of a higher degree of electron repulsion upon pairing of electrons in the same orbital. In this way, one electron is put into each of the five *d*-orbitals and HS configuration is obtained. For example, Br^- is a weak-field ligand and produces a small Δ. So, the $[FeBr_6]^{3-}$ ion would have an orbital diagram as follows,

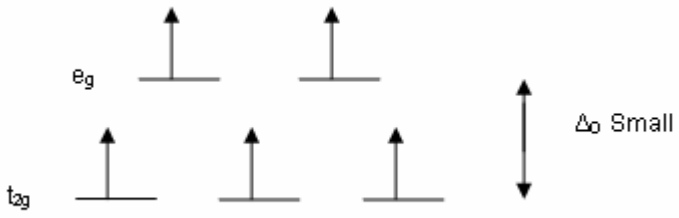

Figure 2-6. Octahedral splitting of the $[FeBr_6]^{3-}$ ion (taken from http://en.wikipedia.org/wiki/Crystal_field_theory).

Finally, orbital ordering refers to the method of electron occupancy of the "*d*" orbitals (or arrangement of the electrons on the *d*-manifold).

The energy gap between the t_{2g} and e_g orbitals is an estimate of the strength of the crystal field. In $YTiO_3$, the Y atom has three valence electrons ($4d^1 5s^2$) and the Ti

atom has four valence electrons ($3d^2 4s^2$). If the charge transition is complete, each oxygen atom can take up to 2 electrons, forming an O^{2-} anion. Formally speaking, all of the electrons in the Y atom will be removed and only one electron will be left in the Ti 3*d* orbitals. According to the CFT, this single electron will occupy the t_{2g} orbital. Therefore, $YTiO_3$ is expected to have a doublet electronic ground-state. Moreover, it is expected that the valence bands mostly consist of Y-O and Ti-O bonding levels with the singly occupied electron in the Ti 3*d* orbitals at the top of the valence bands. In the following discussion, we will only focus on these valence bands.

2.4.2 Spin Unrestricted SCF Formalism

Solving the electronic structure problem in practice, either within DFT or within HF methods, requires choosing a mathematical representation for the one-electron orbitals. The Roothaan-Hall equations [36,37] are a representation of the HF equations in a non-orthonormal basis set. The Roothaan-Hall equations are a set of coupled differential equations derived originally for a closed-shell system where all the electron spins are paired. This set of equations can be expressed in the matrix form and treated as a special case of the generalized eigenvalue problem,

$$FC = SC\varepsilon , \tag{2.13}$$

where F is the so-called Fock matrix, C is a matrix of coefficients, S is the overlap matrix of the basis functions and ε is the (diagonal by convention) matrix of orbital energies.

For open-shell systems with unpaired spins, a straightforward extension to these Roothaan-Hall equations is to consider a restricted many-body wavefunction of the single-determinantal form. The restricted spin orbitals are constrained to have the same spatial function for spin up (α) and spin down (β).

A further improved wavefunction can be obtained by releasing the constraint in restricted open-shell calculation. This is called the unrestricted approach. This theory is the most common molecular orbital method for open-shell molecules. It adopts what has been called the "Different Orbitals for Different Spins" approach, i.e., it uses different molecular orbitals for spin up (α) and spin down (β). This theory results in a pair of coupled Roothaan-Hall equations, known as the Pople-Nesbet equations [38],

$$F^{\alpha}C^{\alpha} = SC^{\alpha}\varepsilon^{\alpha} \tag{2.14}$$

and

$$F^{\beta}C^{\beta} = SC^{\beta}\varepsilon^{\beta}\ , \tag{2.15}$$

where F^{α} and F^{β} are the Fock matrices for the α and β orbitals, C^{α} and C^{β} are the matrices of coefficients for the α and β orbitals, S is the overlap matrix of the basis functions, and ε^{α} and ε^{β} are the matrices of orbital energies for the α and β orbitals. The final result is a set of molecular orbitals and orbital energies for the α spin electrons and a set of molecular orbitals and orbital energies for the β spin electrons. $YTiO_3$ is an open-shell system with a partially filled valence shell. As such, unrestricted open-shell calculations are more reasonable and will thus be performed in this research.

Chapter 3

Electronic Structure of $YTiO_3$ from the LDA+U Method

Previous work has shown the LDA+U method to be a convenient extension to improve the agreement between the band gap computed via DFT and that observed in a variety of transition metal complexes. Central to this approximation is the validity of the empirical parameter U. Several schemes have been proposed recently for the *ab initio* determination of U. However, at least for one method, the results seem to be counter-intuitive and inconsistent [39], as it was found that the U parameter increased with pressure. In this study, we employ a different approach. Instead of evaluating the U parameter from first principles, appropriate values are determined at selected pressures by fitting the LDA+U calculated energy band to the corresponding experimental value. The purpose is to derive the trend of U with increasing pressure and to rationalize the physical implications of this parameter.

The program VASP (Vienna Ab initio Simulation Package) was employed in this study. VASP is a sophisticated software package for performing *ab initio* electronic calculations using pseudopotentials or the projector-augmented wave (PAW) [40,41] method with a plane wave basis set [42]. The approach implemented in VASP is based on the local-density approximation (LDA) with an extension to the LDA+U approximation. VASP uses efficient matrix diagonalization schemes and an efficient Pulay/Broyden charge density mixing. The interaction between ions and electrons is described by ultra-soft Vanderbilt pseudopotentials (US-PP) [43] or by the projector-augmented wave (PAW) method. US-PP (and PAW) allows a considerable reduction of

the number of plane waves per atom for transition metals and first row elements like C and O. VASP uses self-consistency cycles to calculate the electronic ground-state. The combination of this scheme with efficient numerical methods leads to an efficient, robust and fast scheme for evaluating the self-consistent solution for the Kohn-Sham functional. The implemented iterative diagonalization schemes are probably among the fastest schemes currently available and VASP includes a full featured symmetry code which determines the symmetry of an arbitrary configuration automatically. Some details of the approximations and computational parameters are presented in the next sections.

3.1 The Pseudopotential Approximation

It is well known that most physical properties of solids are dependent on the valence electrons to a much greater degree than those of the tightly bound core electrons. It is for this reason that the pseudopotential approximation is introduced. This approximation uses this fact to remove the core electrons and the strong nuclear potential and replaces them with a weaker pseudopotential which acts on a set of pseudo wavefunctions rather than the true valence wavefunctions.

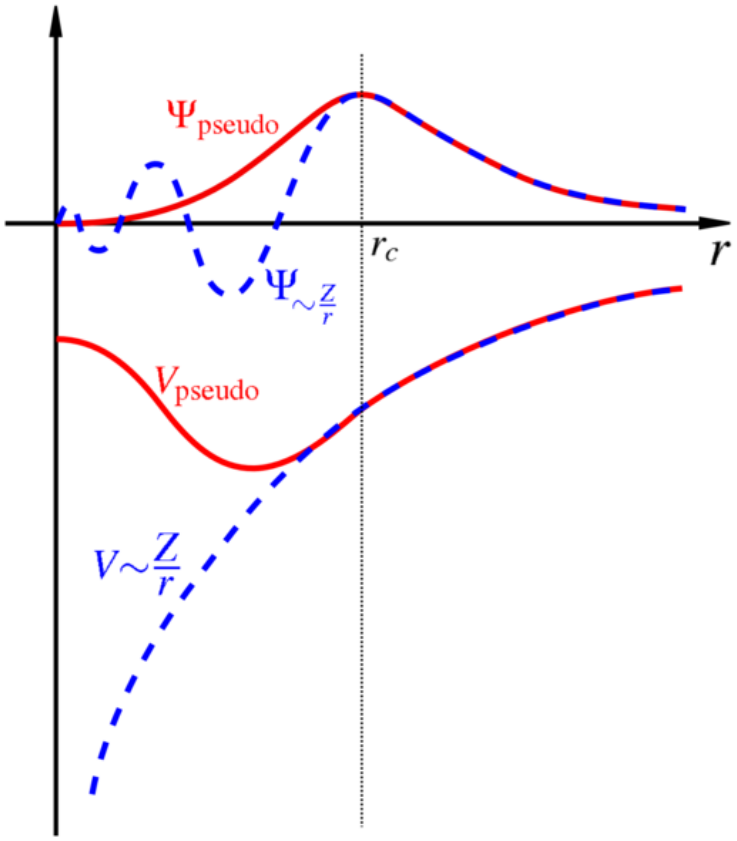

Figure 3-1. Comparison of a wavefuntion in the Coulomb potential of the nucleus (dashed lines) to that of pseudopotential (solid lines). Outside a given radius, r_c, the real and pseudo electron values are identical (taken from http://en.wikipedia.org/wiki/Pseudopotential).

In Figure 3-1, it is shown that the valence wavefunctions oscillate rapidly in the region occupied by the core electrons because of the strong ionic potential. These oscillations maintain the orthogonality between the core and valence electrons. The pseudopotential is constructed in such a way that there are no radial nodes in the pseudo wavefunction in the core region and that the valence pseudo wavefunctions become very smooth and identical to the corresponding all electron wavefunctions outside a radius cut-off r_c.

To obtain the exchange-correlation energy accurately, it is necessary that outside the core region the real and pseudo wavefunctions are identical so that both wavefunctions generate identical charge densities, i.e.,

$$\int_0^{r_c} \psi_{AE}^*(r)\psi_{AE}(r)dr = \int_0^{r_c} \psi_{ps}^*(r)\psi_{ps}(r)dr\,. \qquad (3.1)$$

In this expression, $\psi_{AE}^*(r)$ represents the all-electron wavefunction and $\psi_{ps}^*(r)$ represents the pseudo wavefunction. Formula 3.1 is the norm conserving condition and it guarantees the equality of the all-electron and pseudo wavefunctions outside the core region. Pseudopotentials constructed with these constraints are known as norm-conserving pseudopotentials.

However, many modern pseudopotential calculations use a generalization of the "ultrasoft" pseudopotentials (US-PP) developed by Vanderbilt in the early 1990s [43]. As the name suggests, ultrasoft pseudopotentials attain much smoother pseudo-wavefunctions using considerably fewer plane waves for calculations of the same accuracy. The ultrasoft pseudopotential relaxes the norm-conservation condition and to make up for the resulting charge deficit, localized atom-centered augmentation charges are introduced.

Blöchl [40] further developed the US-PP concept by combining ideas from pseudopotential and the very accurate LAPW (linearized augmented plane wave) method which he called the PAW (projector augmented-wave) method. Some of disadvantages of Vanderbilt's pseudopotentials are avoided in Blöchl's PAW method. The PAW method avoids transferability problems of the pseudopotential approach. Generally, the PAW method can accurately and efficiently calculate the electronic structure of materials within the framework of DFT. The PAW not only contains the numerical advantages of pseudopotential calculations, but also retains the physics of all-electron (AE) calculations, including the correct nodal behavior of the valence electron

wavefunctions and the ability to include upper core states in addition to valence states in the self-consistent iterations.

The PAW method works directly with the full-wavefunctions and potentials and includes the core states. The PAW method also provides a prescription between the PS (pseudo) wavefunctions and the physical AE wavefunctions. PAW is more efficient than US-PP method from the computational point of view because it treats the one-center expansions on radial grids, which effectively eliminates the related computational cost. At very high pressure, it is possible that the core or semi-core orbitals of neighboring atoms overlap. The normal pseudopotentials may not describe this case correctly. Because the PAW method freezes the core orbitals to those of a reference configuration and works only with the valence wavefunctions, it can be used at very high pressure. The PAW method seems to be one of the most powerful approaches at present.

The PAW pseudopotentials for Ti, Y and O atoms used in the present study were taken from the pseudopotential library distributed with the VASP code. Test calculations, as will be discussed later, show that the pseudopotentials are accurate and suitable for $YTiO_3$.

3.2 Sampling of *k* points in Reciprocal Space

The accuracy and the computational effort of electronic structure calculations for solids depend on Brillouin-zone integrations. Properties like the total energy and charge density are obtained from integration performed numerically on discrete points (*k*-points) sampled in the Brillouin zone. Therefore, a proper choice of the *k* points has to be carefully considered for a given accuracy.

In a perfect crystal, any lattice vector, *g*, can be expressed as

$$g = n_1 a_1 + n_2 a_2 + n_3 a_3 \,, \tag{3.2}$$

where a_1, a_2 and a_3 are the basis vectors. The direct lattice is related to a reciprocal lattice by the following orthogonality rules,

$$a_i \cdot b_j = 2\pi\delta_{ij} \,. \tag{3.3}$$

Similar to the direct space, any reciprocal lattice vector, K, can be expressed as a linear combination of the reciporcal basis vectors b_1, b_2 and b_3,

$$K = K_1 b_1 + K_2 b_2 + K_3 b_3 \,. \tag{3.4}$$

Making use of the periodic boundary conditions (PBC) and Bloch theorem and after a series of derivation, it can be shown that

$$k = \frac{n_1}{N_1} b_1 + \frac{n_2}{N_2} b_2 + \frac{n_3}{N_3} b_3 \,, \tag{3.5}$$

where n_1 - n_3 are integers ($0 \le n_j \le N_j$), $N = N_1 \times N_2 \times N_3$ is the number of cells in the finite crystal and b_1 - b_3 are the basis vectors in reciprocal space.

It is generally possible to sample matrix H at a finite number of k-points and solve the Schrödinger equation for a periodic system at the corresponding k-points in the first Brillouin zone,

$$H\Psi_n(r,k) = E_n(k)\Psi_n(r,k) \,. \tag{3.6}$$

The accuracy of the calculation depends on the number of k points .

The number of *k*-points can be reduced by exploring the crystal symmetry. In the Monkhorst-Pack scheme, *k*-points are uniformly distributed in the first Brillouin zone. To reduce the size of the mesh, only symmetry unique *k*-points are retained. This scheme allows the accurate calculation of the electronic structures with a fairly large *k*-point mesh of a system with high space group symmetry. In the calculation, we employed a $8\times6\times8$ *k*-mesh generation reduced with the Monkhorst-Pack scheme [24].

3.3 Optimal U Parameters at Ambient and High Pressures

In this section, we obtain the optimal U parameter at each pressure by matching the calculated band gap energies with those obtained from synchrotron infrared experiments. For $YTiO_3$, the initial parameters are taken from experiment with space group Pnma (space group 62) [26] and lattice constants a = 5.679(2) Å, b = 7.611(3) Å, c = 5.316(2) Å [44] with standard deviations given in parentheses. The atomic positional parameters are shown as follows [44],

	x	*y*	*z*
Y	0.07294(12)	(0.25000)	0.97925(14)
Ti	(0.00000)	(0.00000)	(0.50000)
O1	0.4580(9)	(0.25000)	0.1213(10)
O2	0.3095(7)	0.0579(5)	0.6909(6)

Table 3-1. Experimental atomic parameters of $YTiO_3$ and standard deviations are given in parentheses (taken from Ref. 44).

Using the parameters presented above, the crystal structure of $YTiO_3$ is shown below (see Figure 3-2). Each Ti atom in the crystal structure is surrounded by six O

atoms. There are three distinct, but approximately equal Ti bonds with bond lengths of 2.0161, 2.0232 and 2.0769 Å. The O-Ti-O angles range from $87-90°$. Therefore, the local environment of the Ti atom is only slightly distorted from an octahedron. Consequently, it is not inappropriate to describe the Ti 3*d* orbitals under the effect of the crystal field of the oxygen atoms loosely in the terminology of the ideal octahedral crystal field (i.e., the Ti 3*d* orbitals split into the t_{2g} and e_g set). Moreover, due to the distortion, the t_{2g} band further split into two bands with only the lower band being singly occupied. In the ensuing discussion, we refer the singly filled band as lower "t_{2g}" and the lowest empty band as higher "t_{2g}". The empty e_g band is located at higher energy.

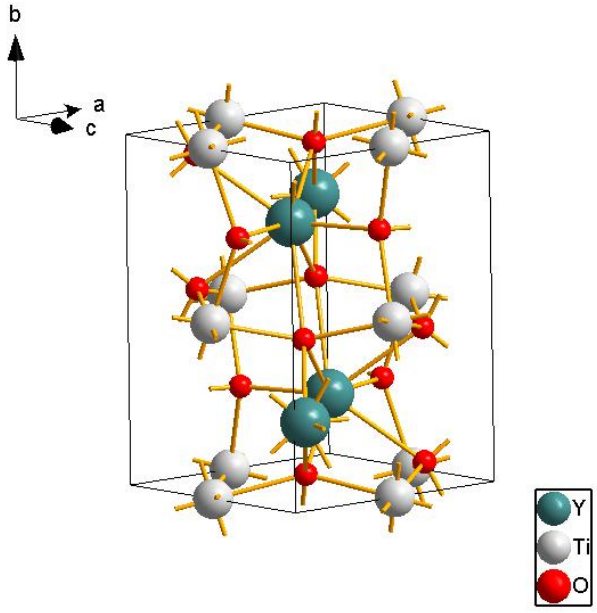

Figure 3-2. A perspective view of the structure of $YTiO_3$ at 0 GPa.

As described in the previous chapter, since only the Ti 3*d* orbitals are expected to be occupied at the top of the valence band, the on-site Coulomb correction, U, is applied to the Ti atom only. At each pressure, the optimal U is treated as an empirical parameter by matching the calculated and observed band gap energies.

The experimental band gaps are taken from Figure 3-3 [26]. Since the maximum band gap energy of $YTiO_3$ is ~0.652 eV or ~5300 cm^{-1}, it can be measured conveniently

with the mid-infrared optical absorption under pressure and at ambient temperature (T = 295 K). Quasi-hydrostatic conditions were ensured by the use of two different pressure transmission media - solid N_2 and KCl. The experimental results clearly show that the band gap decreases with increasing pressure. From 1.6 to 16 GPa, the band gap reduces by ~2000 cm^{-1} (or 0.25 eV). No closure of the band gap is observed in the experiment up to 16 GPa. Since no experimental band gap measurement was available for pressures over 16 GPa, the band gap energy ΔE at pressure P > 16 GPa was obtained from the following extrapolation derived from a fit to experimental data points,

$$E(P)(\text{cm}^{-1}) = 5300 - 145 \times P(\text{GPa}).$$

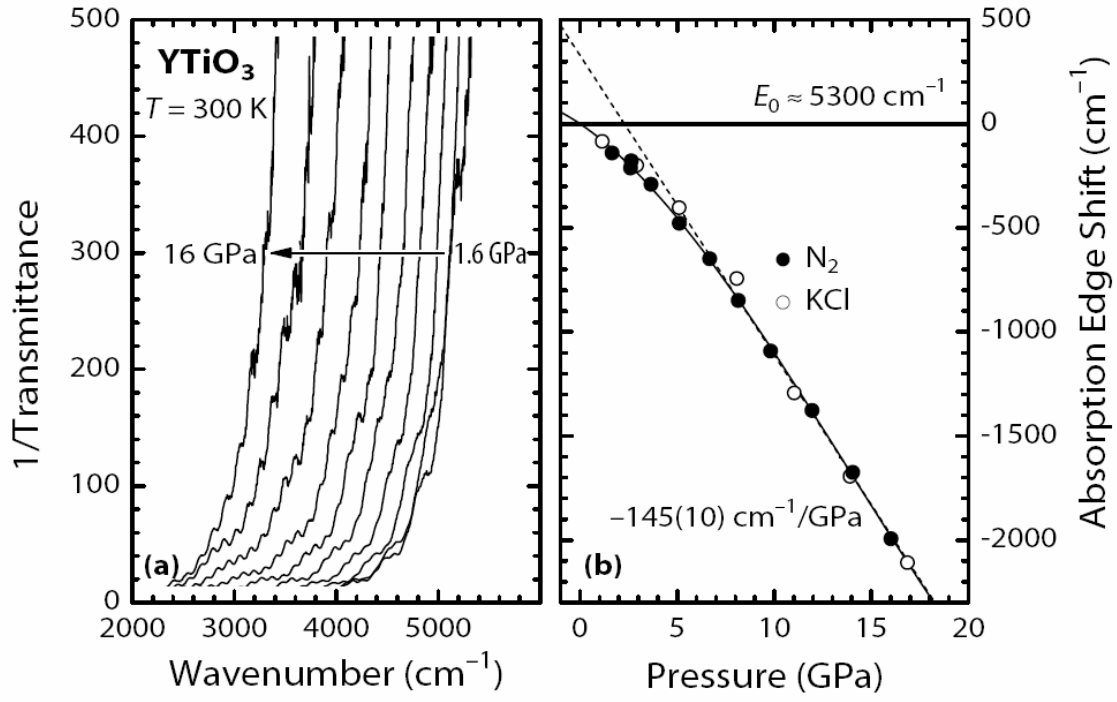

Figure 3-3. Mid-infrared optical absorption frequency of $YTiO_3$ under pressure at T = 295 K (taken from Ref. 26).

Spin polarized LDA+U (or LSDA+U, sometimes also label as GGA+U) calculations started from an initial estimate of U = 3.6 eV at 0 GPa. The U parameter is

then adjusted until the calculated and experimental gaps are in agreement. It is important to mention that during this iterative process, all positional parameters and unit cell constants were fully optimized. The same procedure is then repeated at several selected pressures up to 40 GPa. Through a series of similar calculations, the optimal U parameters at different pressures are obtained.

Before embarking on a detailed analysis of the electronic structure, the reliability of the LDA+U method and the choice of computational parameters used in the present calculations are examined from the comparison of calculated and experimental unit cell parameters. Details of the crystal structure will be discussed in a later section.

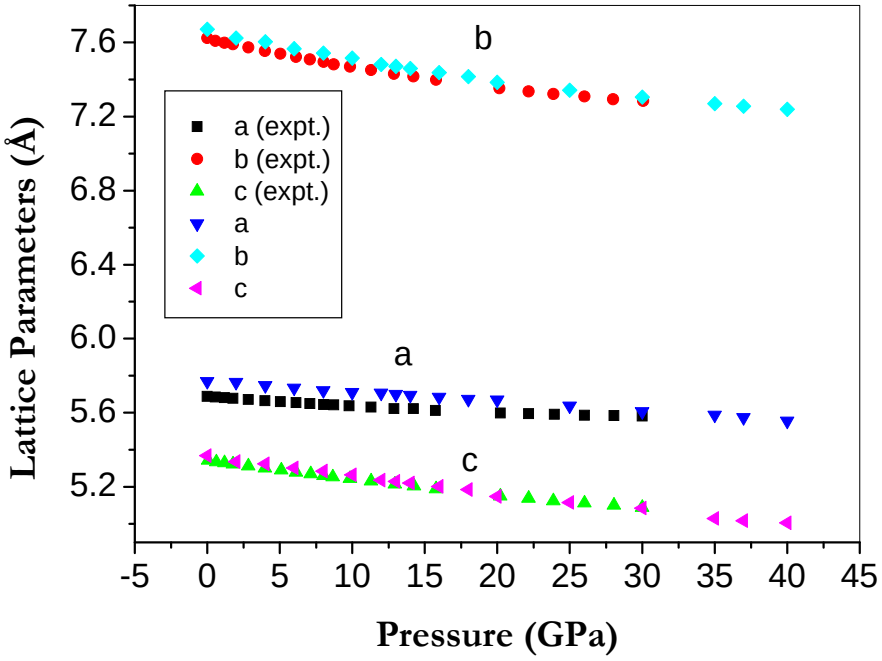

Figure 3-4. Comparison of experimental and calculated lattice constants.

In Figure 3-4, a(expt.), b(expt.) and c(expt.) denote the experimental lattice constants and a, b and c denote the calculated values. The theoretical predicted lattice constants at zero pressure a = 5.7705 Å, b = 7.6719 Å and c = 5.3675 Å, are in exceedingly good agreement with the experiment values of a = 5.6790 Å, b = 7.6110 Å and c = 5.3160 Å. A summary of the calculated atomic coordinates is shown in Table

3-2. It is clear that from a comparison with Table 3-1 that the general agreement between the calculated and measured atomic positions at zero pressure is excellent. The error is on the order of 1.0×10^{-3}. In fact, the absolute error over the entire pressure range studied here is less than 2% which is well within the limit of reliability of DFT.

	x	*y*	*z*
Y	0.0749	0.2500	0.9764
Ti	0.0000	0.0000	0.5000
O1	0.4544	0.2500	0.1260
O2	0.3101	0.0585	0.6904

Table 3-2. Calculated atomic parameters of $YTiO_3$ at 0 GPa.

To the best of our knowledge, the results presented here represent the first comprehensive investigation on the use of the LDA+U method with determination of crystal structure. As the results show, the methodology is quite successful and comparable to the accuracy of the LDA method.

Table 3-3 summarizes the optimal U parameter obtained from the LDA+U calculations. A general trend emerges on the pressure dependence of the optimal U parameters. At low pressures from 0 to 4 GPa, the U parameter is not sensitive to the change in pressure and remains fairly constant at 2.70 eV. This observation helps to justify the assumption of a constant U parameter in previous applications of the LDA+U method to several mineral oxide systems at relatively low pressure. It is likely that the change in electron correlation effects at low pressure is quite small and does not affect the electronic structure to a significant extent. This assumption, however, is certainly not correct over a wider range of pressures. The U parameter shows a steady but slow decrease from 4 to 12 GPa and drops more rapidly for pressures above 12 GPa. An important and new result obtained from the present study is that for compression from ambient pressure to 32 GPa, the pressure at which $YTiO_3$ is predicted to become

metallic (see below), the U parameter changes from 2.70 eV to 1.98 eV - an almost 33% reduction in the absolute magnitude.

Pressure (GPa)	**0**	**2**	**4**	**6**	**8**	**10**
optimal U parameter (eV)	2.700	2.700	2.700	2.680	2.680	2.630
Pressure (GPa)	**12**	**13**	**14**	**16**	**18**	**20**
optimal U parameter (eV)	2.600	2.600	2.600	2.500	2.500	2.431
Pressure (GPa)	**25**	**30**	**31**	**32**	**33**	**34**
optimal U parameter (eV)	2.285	2.071	2.027	1.981	1.934	1.885
Pressure (GPa)	**35**	**37**	**40**			
optimal U parameter (eV)	1.835	1.729	1.561			

Table 3-3. The optimal U parameters at different pressures.

We performed a polynomial fit analysis to the results tabulated in Table 3-3. Figure 3-5 compares the calculated and fitted trend of the on-site Coulomb repulsion parameter with pressure. The equation obtained from the fitted curve is

$$U(P) = 2.70 + 0.00242P - 7.74\times10^{-4}P^2 \,. \qquad (3.7)$$

Using this equation, one would estimate that at *ca*. 60 GPa, the U parameter should vanish. This pressure is significantly higher than the predicted metallization pressure of 32 GPa. Therefore, even in the metallic state, effects of on-site repulsion of the Ti 3*d* electron are not negligible.

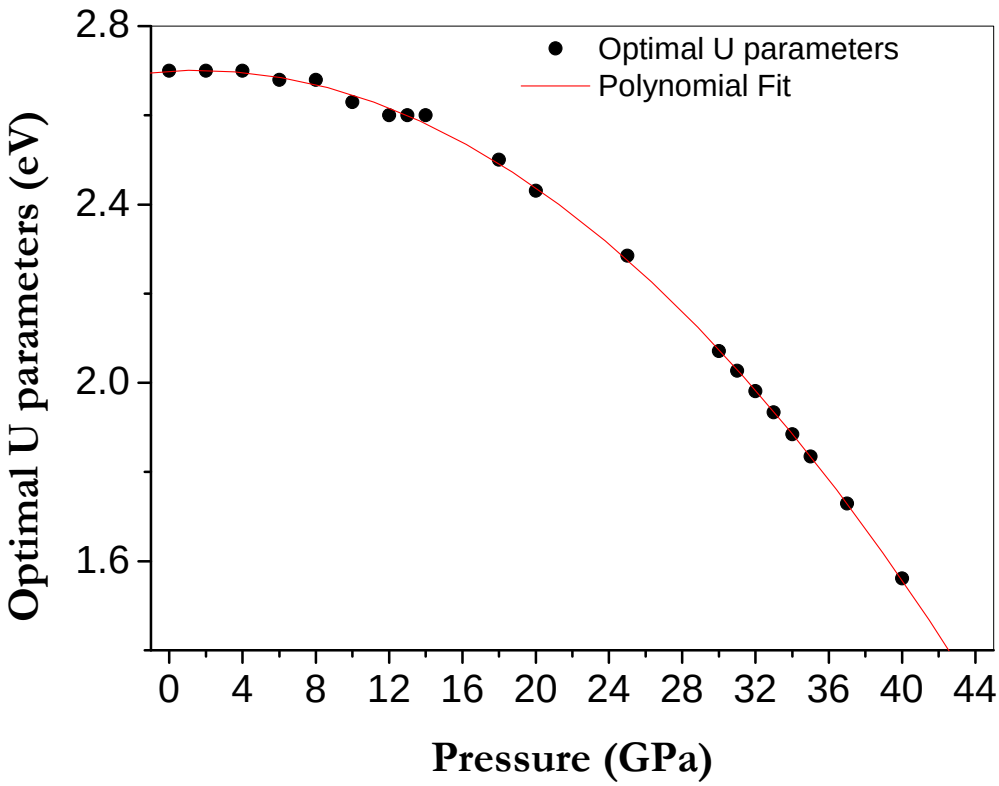

Figure 3-5. Optimal U parameter with pressures.

Table 3-4 summarizes the experimental and predicted band gaps and their difference for $YTiO_3$ from 0 to 40 GPa. From the LDA+U calculations, it is shown that $YTiO_3$ will become metallic at 32 GPa. This value is consistent with the estimation from the extrapolation of the experimental band gap energies. This result, however, disagrees with a recent theoretical calculation [45], where the electronic gap closure was suggested to occur at ~100 GPa - almost 3 times that of the present calculated pressure. It should be noted that in this earlier calculation [45], a constant U parameter was employed throughout the entire pressure range. As shown here, this assumption is invalid and therefore the pressure of the closure of the band gap would be seriously overestimated.

Pressure (GPa)	Calculated band gap (eV)	Experiment (eV)	Exp.- Cal.band gap (eV)
0 (U = 2.700 eV)	0.652	0.660	0.008
2 (U = 2.700 eV)	0.614	0.635	0.021
4 (U = 2.700 eV)	0.606	0.608	0.002
6 (U = 2.680 eV)	0.570	0.577	0.007
8 (U = 2.680 eV)	0.556	0.548	-0.008
10 (U = 2.630 eV)	0.502	0.508	0.006
12 (U = 2.600 eV)	0.46	0.471	0.011
13 (U = 2.600 eV)	0.452	0.459	0.007
14 (U = 2.600 eV)	0.446	0.446	0.000
16 (U = 2.500 eV)	0.372	0.397	0.025
18 (U = 2.500 eV)	0.352	0.347	-0.005
20 (U = 2.431 eV)	0.290		
25 (U = 2.285 eV)	0.176		
30 (U = 2.071 eV)	0.036		
31 (U = 2.027eV)	0.004		
32 (U = 1.981 eV)	no band gap (metallic)		
33 (U = 1.934 eV)	no band gap (metallic)		
34 (U = 1.885 eV)	no band gap (metallic)		
35 (U = 1.835 eV)	no band gap (metallic)		
37 (U = 1.729 eV)	no band gap (metallic)		
40 (U = 1.561 eV)	no band gap (metallic)		

Table 3-4. Band gap comparison for $YTiO_3$.

The calculated and observed band gap energies are compared in Figure 3-6. The pressure where metallization occurs can be estimated by extrapolating the gap energy to 0.0 eV.

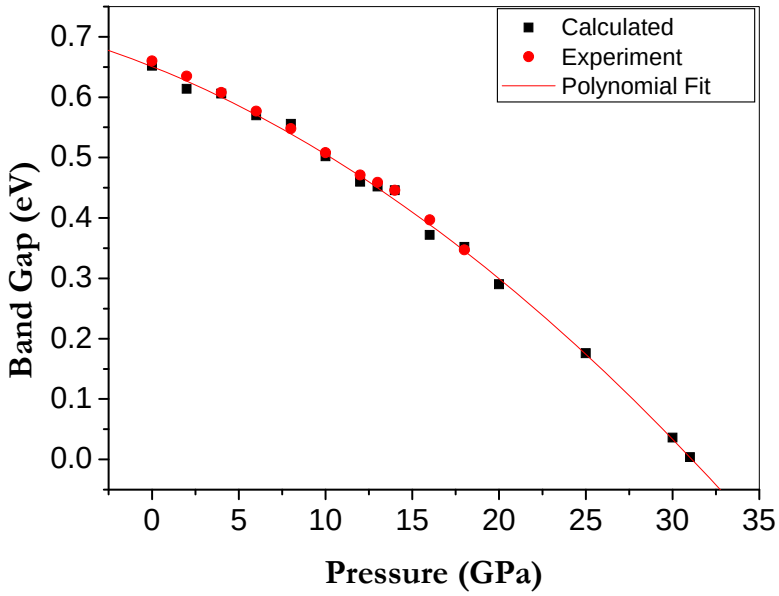

Figure 3-6. Comparison between calculated and experimental band gaps.

The calculated trend of the dependence of the U parameter with pressure provides insights into the behaviour of the electron repulsive interactions in $YTiO_3$. Since the U parameter is added to the Ti atoms to alleviate the problem of overestimated delocalization of valence electrons, a smaller U at high pressure indicates that the effect of delocalization becomes more dominant. It is consistent with the expectation that the overlap between Ti and the surrounding oxygen atoms will become more significant with decreasing Ti-O distances at high pressure. Consequently, the valence electrons should be more delocalized. As a result, importance of the on-site Coulomb repulsion becomes less significant.

3.4 Total and Projected Density of States

In this section, discussion is focused on the electronic structure of the occupied Ti 3*d* band, situated at the top of the valence band using the calculated electronic DOS. The PDOS onto the Ti 3*d* orbitals and their individual components, i.e., d_{xy}, d_{yz}, d_{z^2}, d_{xz} and $d_{x^2-y^2}$, will be used to assist the characterization and interpretation of the electron orbitals. Results of the PDOS calculations on the dominant valence bands of Ti at several pressures are shown in Figures 3-7 to 3-12. For convenience, the vertical lines at $E = 0$ indicate the top of the valence band.

As previously stated, the Ti atoms in $YTiO_3$ are surrounded by 6 oxygen atoms in a distorted octahedral environment. Therefore, the Ti 3*d* atomic orbitals are expected to split into t_{2g} and e_g manifolds under the crystal field. As discussed earlier, the degeneracy of the t_{2g} band is lifted by the local symmetry and t_{2g} band is further decomposed into a singly filled band and an empty band. The band gap is a measure of this splitting. It is shown in the PDOS that the lower t_{2g} band is very tight as indicated by the very small band width of ~0.5 eV. There is a "pseudo" band gap of 2-3 eV between the lower t_{2g} band and the broad band ranging from -3 to -8 eV. This broad band can be assigned to the Ti-O and Y-O bonds. The large band width indicates strong dispersion, *i.e.,* strong bonding interactions. Also the Ti-O bands of spin-up and spin-down are nearly identical at different pressures. There are only Ti 3*d* bands of spin-up below the top of valence bands. In these figures, it is observed that except for the d_{z^2} and d_{xz} orbitals, the highest energy electronic band at the top of the valence level shows a clear dip. This can be attributed to the splitting of the Ti t_{2g} orbitals due to deviation of the local symmetry from the ideal octahedron environment.

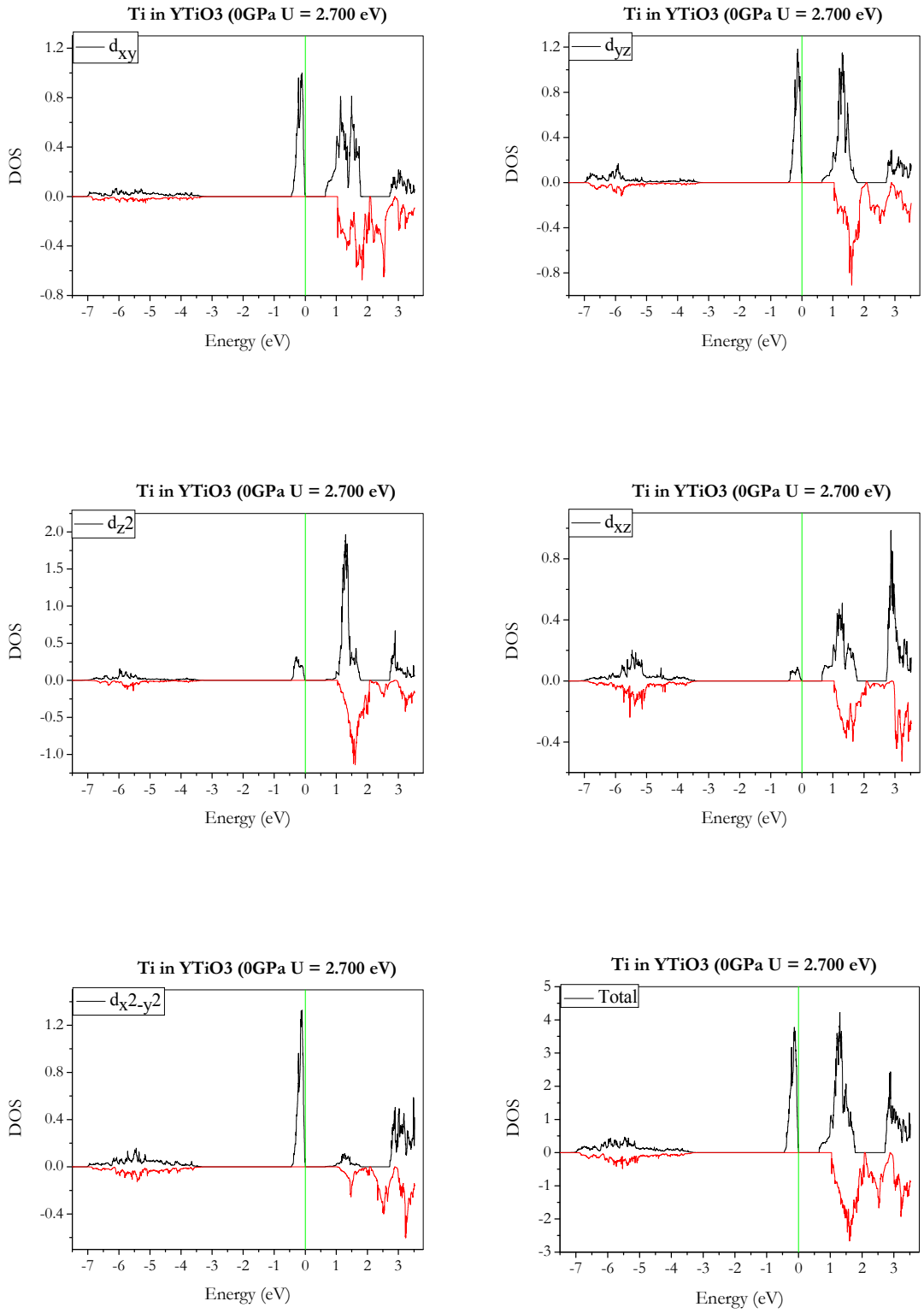

Figure 3-7. PDOS of Ti in $YTiO_3$ at 0 GPa using U = 2.700 eV.

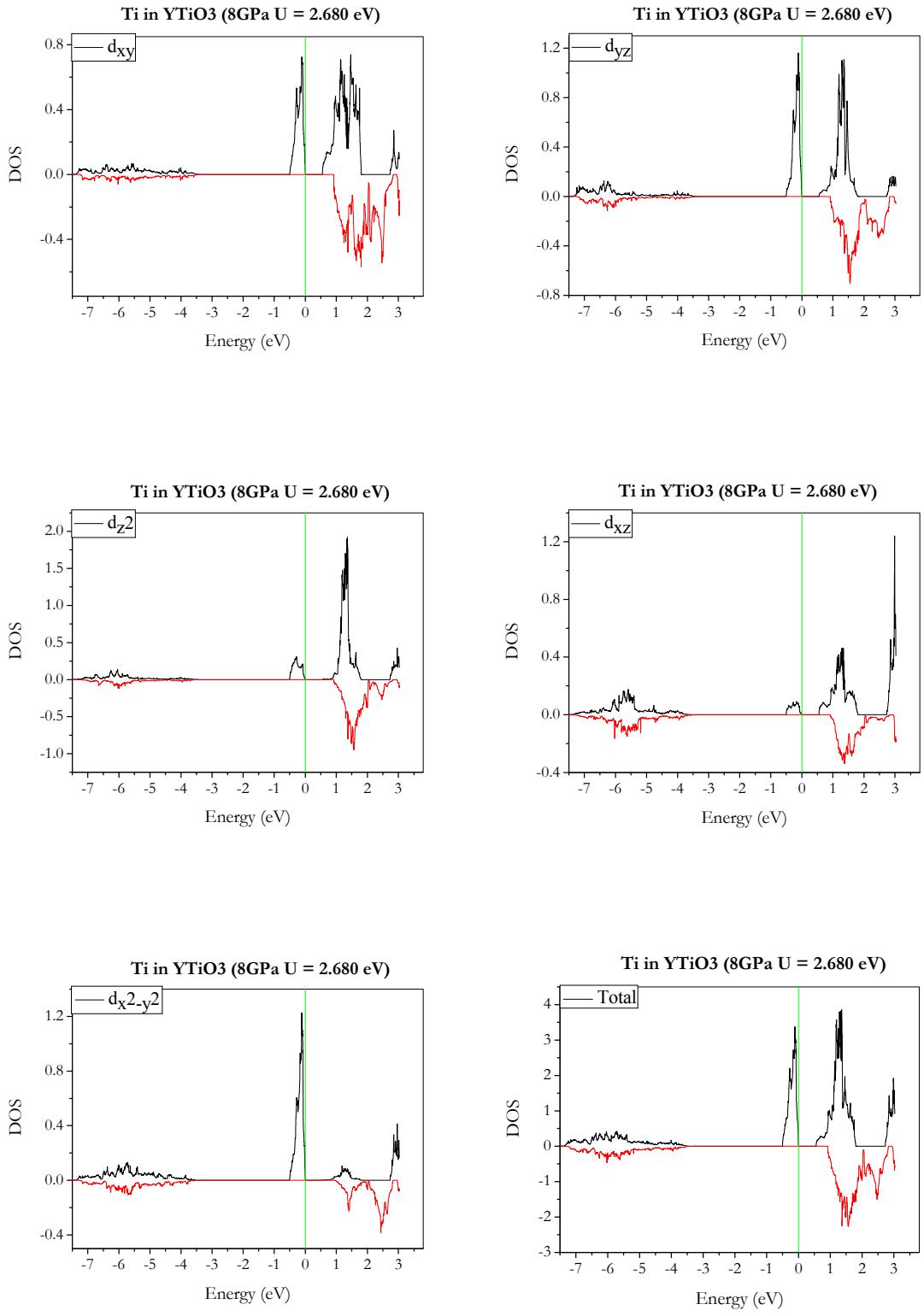

Figure 3-8. PDOS of Ti in $YTiO_3$ at 8 GPa using U = 2.650 eV.

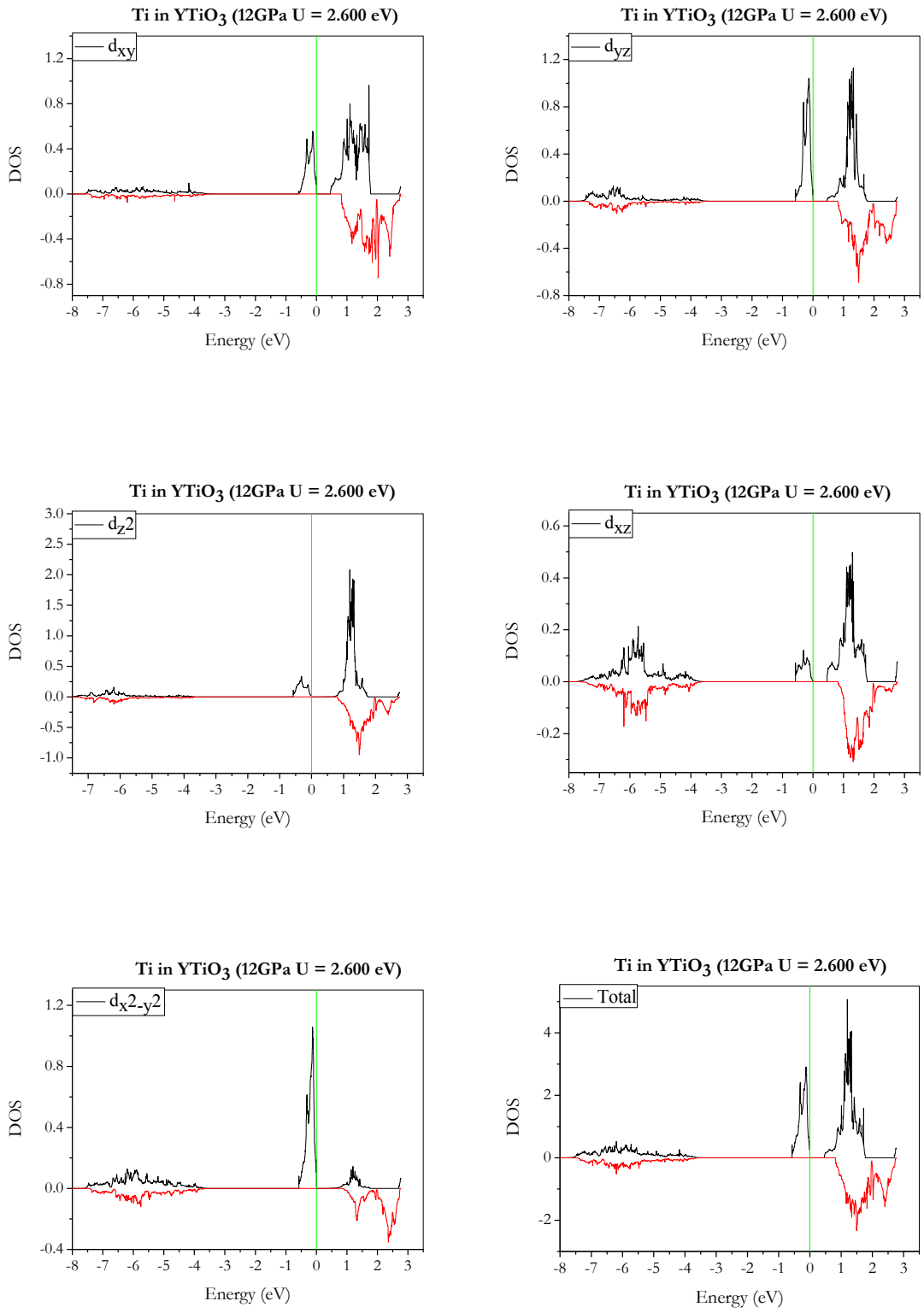

Figure 3-9. PDOS of Ti in $YTiO_3$ at 12 GPa using U = 2.600 eV.

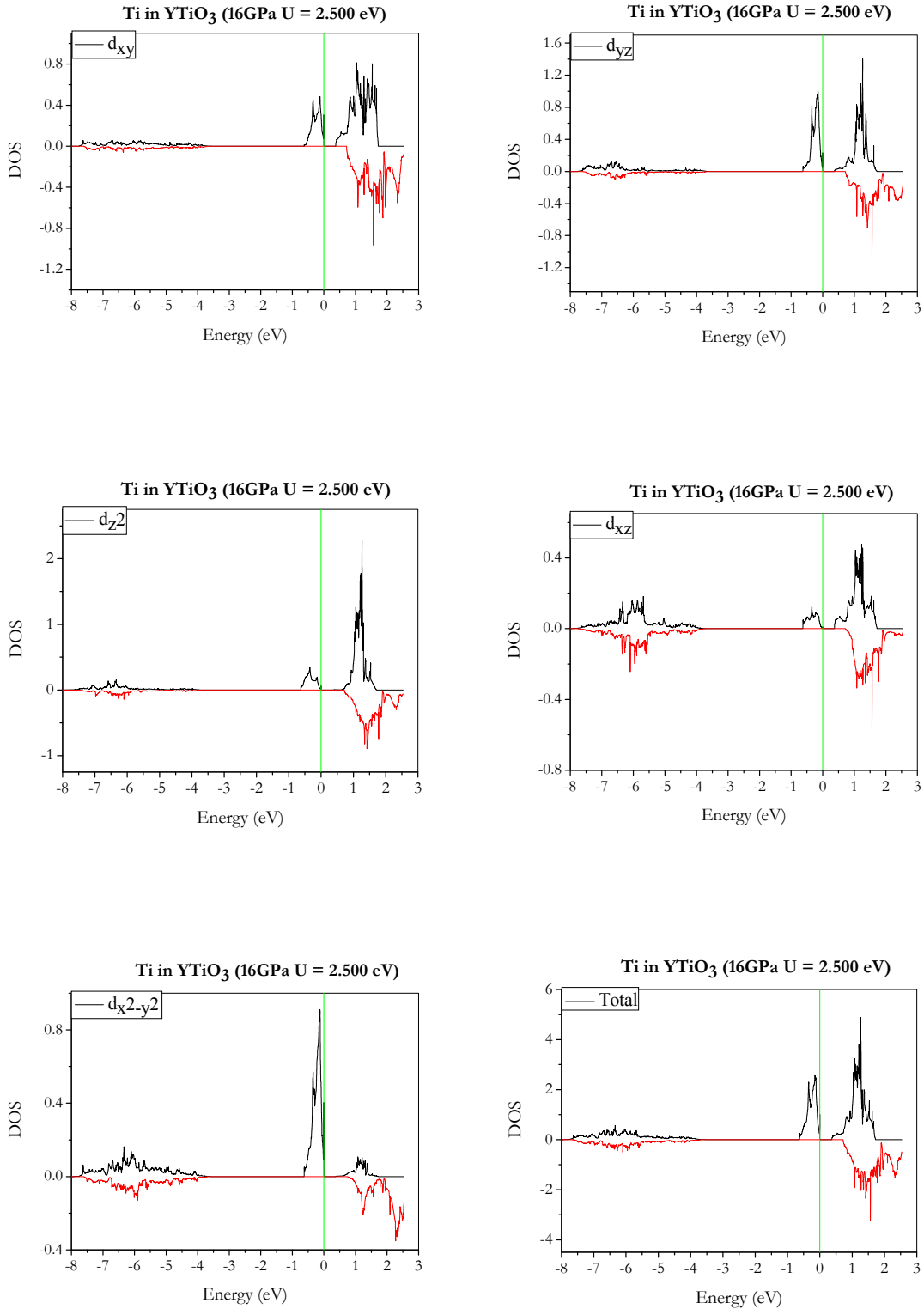

Figure 3-10. PDOS of Ti in $YTiO_3$ at 16 GPa using U = 2.500 eV.

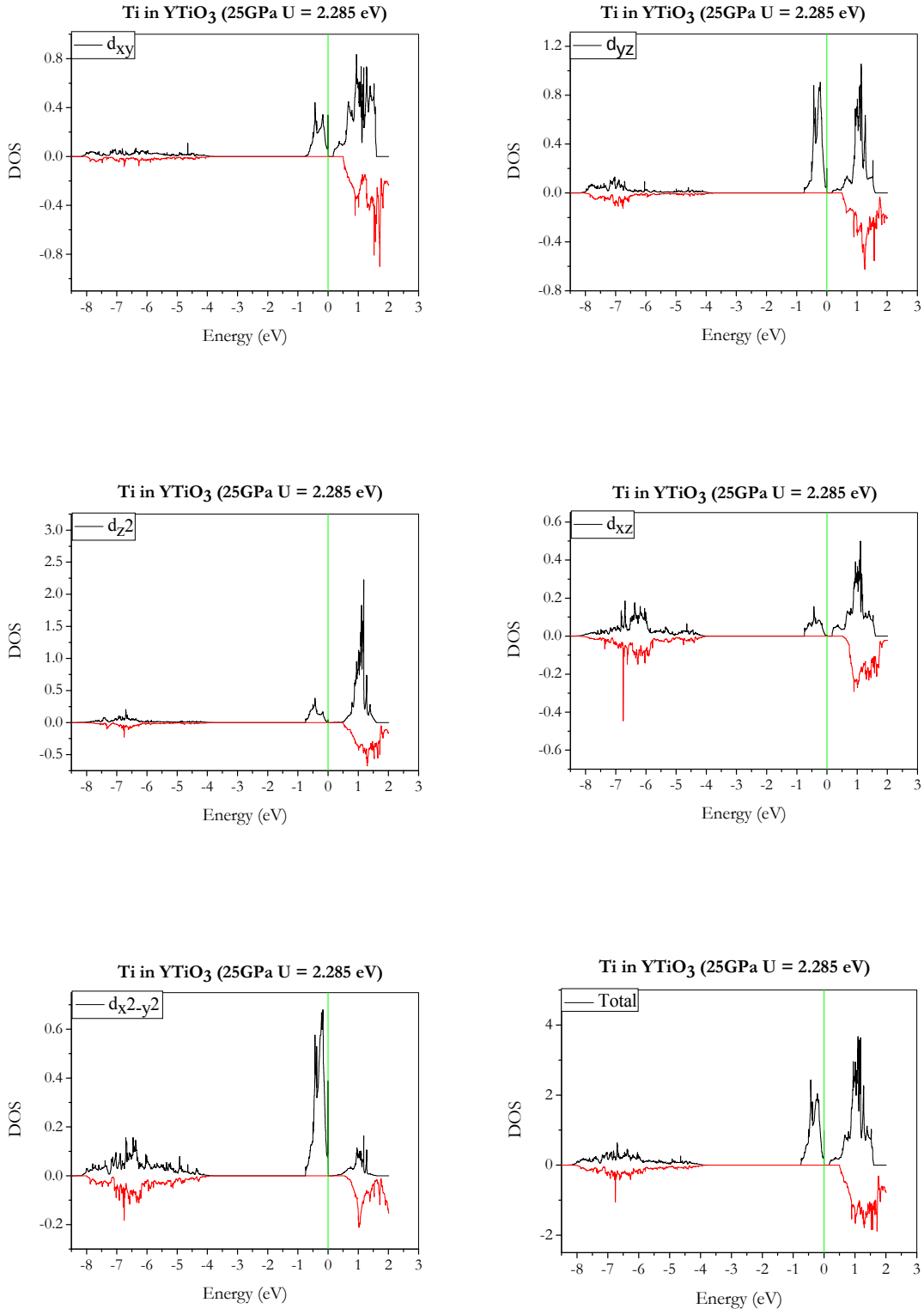

Figure 3-11. PDOS of Ti in $YTiO_3$ at 25 GPa using U = 2.285 eV.

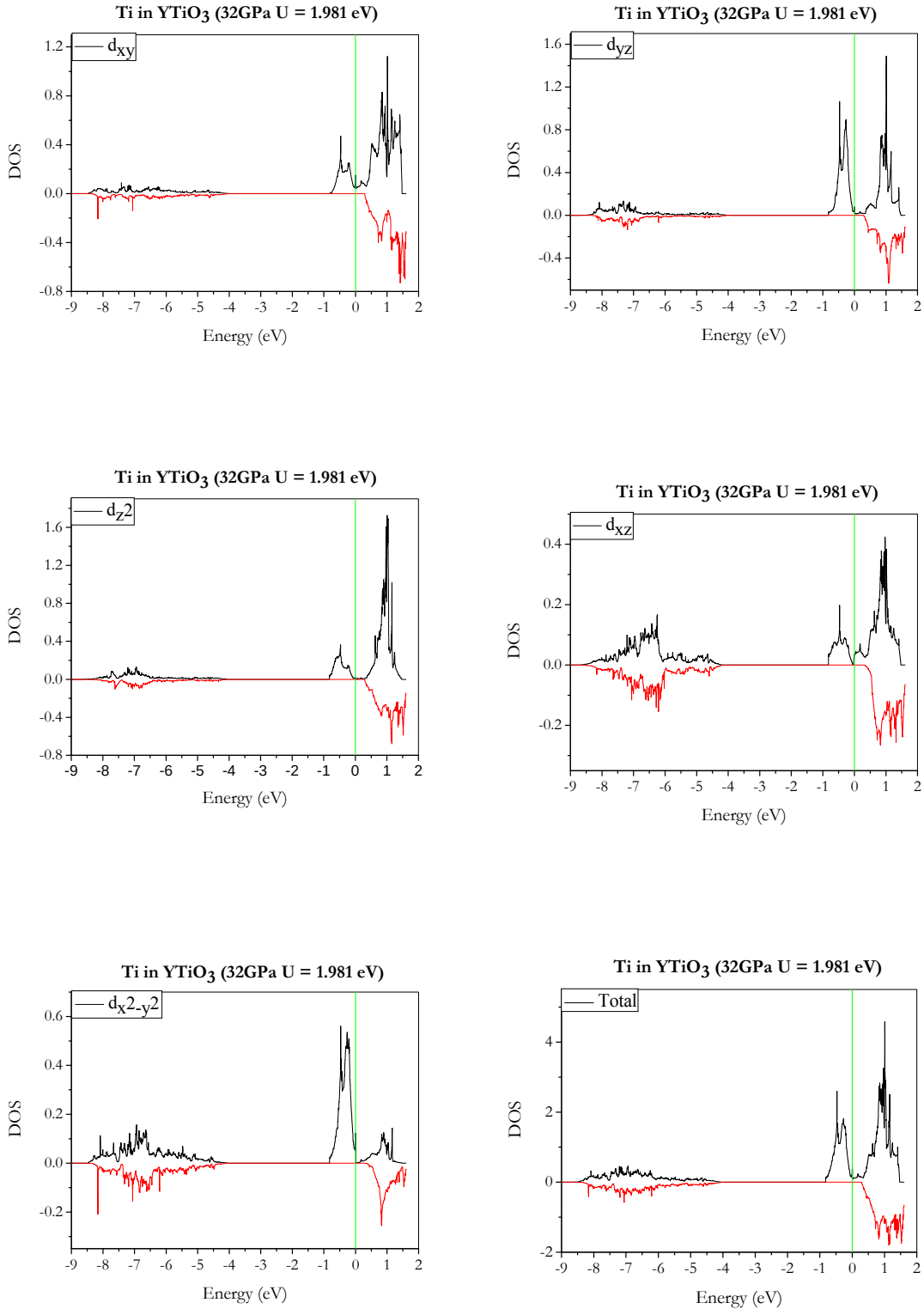

Figure 3-12. PDOS of Ti in $YTiO_3$ at 32 GPa using U = 1.981 eV.

The population of the Ti 3*d* t_{2g} orbitals can be evaluated from integrating the DOS in an energy window comprising only the uppermost Ti 3*d* valence band. The results are summarized in Table 3-5. At zero pressure, the population of the t_{2g} orbitals is 0.723 *e*. From the crystal field analysis on the formal charges in $YTiO_3$, one would expect only one electron to remain in the Ti 3*d* orbitals. The theoretical calculations confirm the estimate from this very crude analysis.

From Table 3-5, it is clear that the orbitals d_{xy}, d_{yz} and $d_{x^2-y^2}$ are the main contributors to the electron occupancies of Ti 3*d* states. Also, the electron occupancies of the orbitals d_{xy} and $d_{x^2-y^2}$ decrease with increasing pressure. Conversely, the electron occupancy of orbital d_{yz} increases with increasing pressure.

	0 GPa	**8 GPa**	**12 GPa**	**16 GPa**	**25 GPa**	**32 GPa**
d_{xy}	0.197	0.159	0.139	0.132	0.119	0.112
d_{yz}	0.208	0.220	0.230	0.234	0.245	0.255
d_{z^2}	0.073	0.085	0.090	0.093	0.099	0.106
d_{xz}	0.020	0.027	0.033	0.036	0.042	0.048
$d_{x^2-y^2}$	0.227	0.227	0.223	0.219	0.209	0.191
sum	0.723	0.718	0.714	0.714	0.714	0.712

Table 3-5. Electron occupancy of Ti 3*d* t_{2g} below the top of valence band at different pressures.

In passing, it is interesting to compare the total DOS at zero pressure obtained here with that of a previous LDA+U calculation [46] employing a slightly different U parameter of 3 eV as a check on the computational procedure. It is reassuring that, although not unexpected, the calculated total DOS are almost identical. For example, there is a clear dip at the top of valence band in Figure 3-13 (b). The lowest energy band

ranges from -8 to -4 eV and is predominantly of O-2p character in (a), whereas in figure (b), the lowest energy band is about from -7 to -3 eV. In figure (a), the e_g band is situated at 2 eV, and in figure (b), the e_g band is obviously situated above 2 eV. Finally, the calculated band gap reported in Ref. [46] is 0.6 eV which is very close to 0.652 eV obtained here.

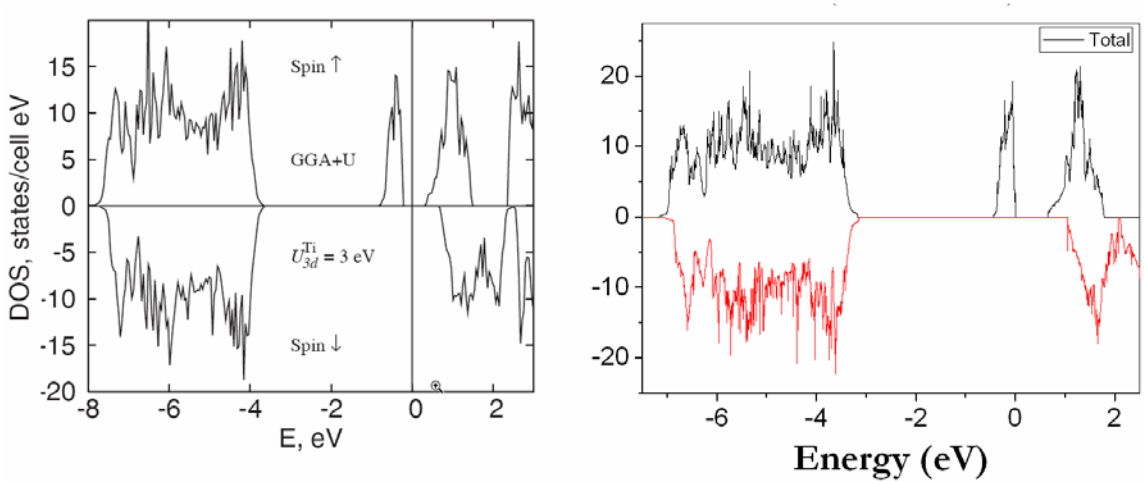

Figure 3-13. Total DOS of $YTiO_3$, (a) result from Ref. 46, (b) present calculated result.

3.5 Orbital Ordering

A focus of the present study is to investigate the proposal of a change in orbital ordering in the Ti 3*d* orbital of $YTiO_3$ at approximately 13 GPa. Recently, the investigation of the orbital ordering of *d* electrons in transition metal perovskites has attracted much interest due to the novel magnetic properties of these materials.

In the experimental work [26], based on the apparent change in the atomic positions, it was conjectured that there is redistribution of the Ti 3*d* electrons (i.e., orbital reordering) at pressure higher than 13 GPa. The proposed orbital reordering scheme is shown in Figure 3-14. At low pressure, it was suggested that the electron of Ti occupies the $3d_{xy}$ and $3d_{xz}$ hybrid orbitals. However, at pressures higher than 13 GPa, a predominant change in the occupancy was observed, favoring the $3\,d_{xy}$ orbital. (It should be noted that the labels of the *d*-orbital components are dependent on the choice of the coordinate system).

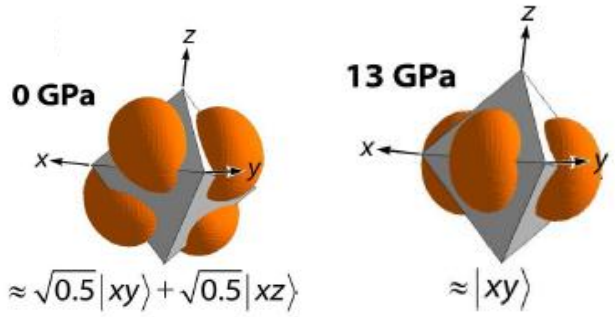

Figure 3-14. Orientation of the Ti 3*d* orbitals at 0 and 13 GPa (taken from Ref. 26).

To investigate the possibility of orbital reordering, the spatial distributions of the Ti 3*d* electrons, obtained from integration of the charge density within an energy window from -2 to 0 eV of the Ti 3*d* valence band, are calculated at several pressures.

The 3D iso-surfaces (contour level at 0.3 e/Å^3) of the charge distribution are shown in Figures 3-15.

The Ti 3*d* electron density, centered around the Ti atom, is highly symmetric and resembles a 2D "rhombus" pattern. However, the symmetry plane of the charge distribution does not coincide with any of the atomic *d*-orbital components of the Ti atom. This is not too surprising as it has already been shown in the calculated orbital populations reported in Table 3-5 that the Ti 3*d* band is comprised mostly of d_{xy}, d_{yz}, and $d_{x^2-y^2}$ orbitals. Therefore, this band is not expected to resemble any of the individual *d* components. It is noteworthy that the electron density is located spatially between the surrounding oxygen atoms. This is exactly as expected for the occupancy of the t_{2g} set based on the crystal field theory. The proposal that at low pressures the Ti 3*d* electron is a combination of the d_{xy} and d_{yz} orbitals is not entirely correct.

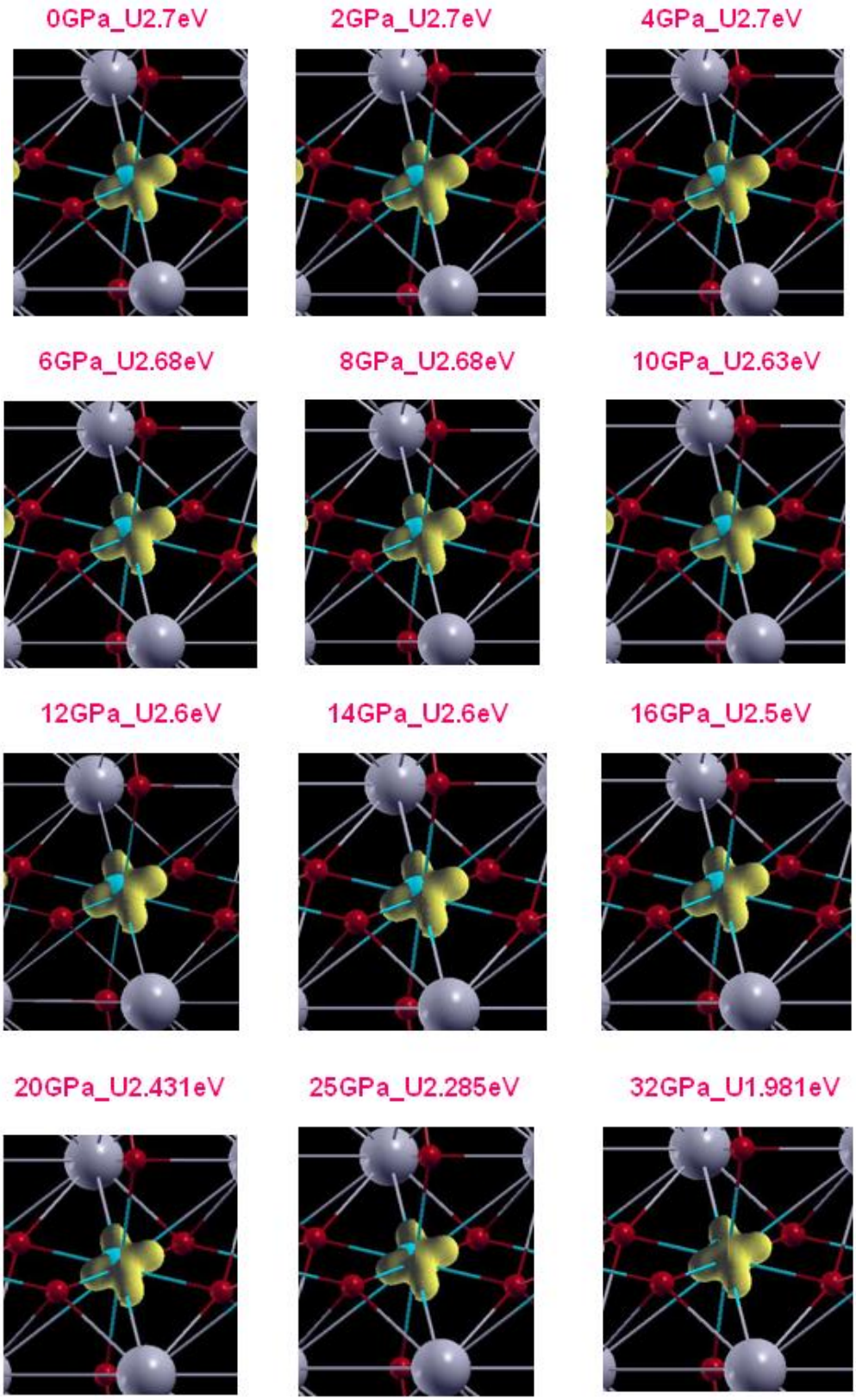

Figure 3-15. Spatial distribution of Ti 3*d* orbitals at different pressure.

The most important observation from the analysis of the electron density distribution is that the topology is not significantly affected by the pressure. Needless to say, no orbital reordering is observed in the present calculations. This conclusion is contradictory to the conjecture derived from the experiment. The discrepancy between theory and experiment is due to details of the crystal structure in $YTiO_3$ and will be elaborated in the following section.

3.6 Comparison of Calculated and Experimental Structures

The atomic positions of $YTiO_3$ have been determined up to 24 GPa from Rietveld refinement of in-situ powder diffraction patterns obtained in a diamond anvil cell with synchrotron X-rays. As already described earlier, $YTiO_3$ has a Pnma space group and the Y atoms are located in the special Wyckoff position 4c with the Y y-coordinate fixed at 1/4 by site symmetry. The variable positional parameters for the Y atom are x and z. The experimentally derived coordinates for Y are shown in Figure 3-16.

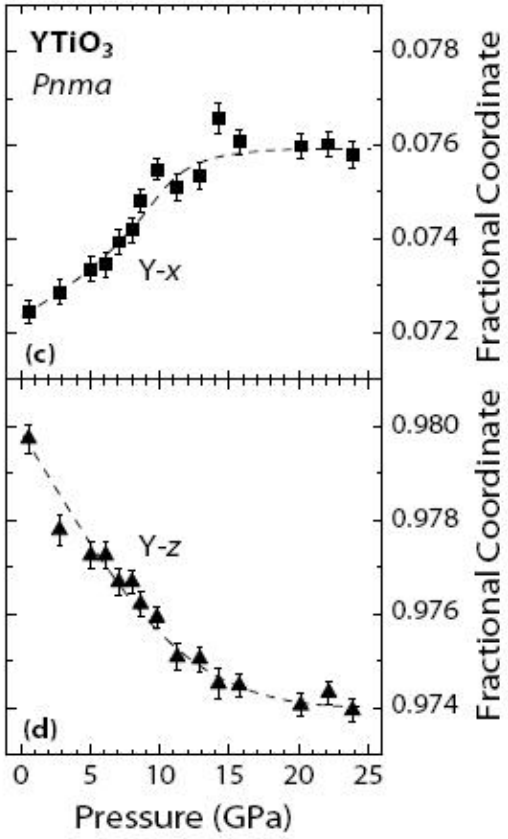

Figure 3-16. Experimental x and z fractional coordinates of Y in $YTiO_3$ (from Ref.26).

The results show that the Y-x coordinate increases initially with pressure until 13 GPa. Upon further compression the x-coordinate remains close to 0.076. The Y-z coordinate decreases with pressure and also seems to flatten out to 0.974 at pressures higher than 13 GPa.

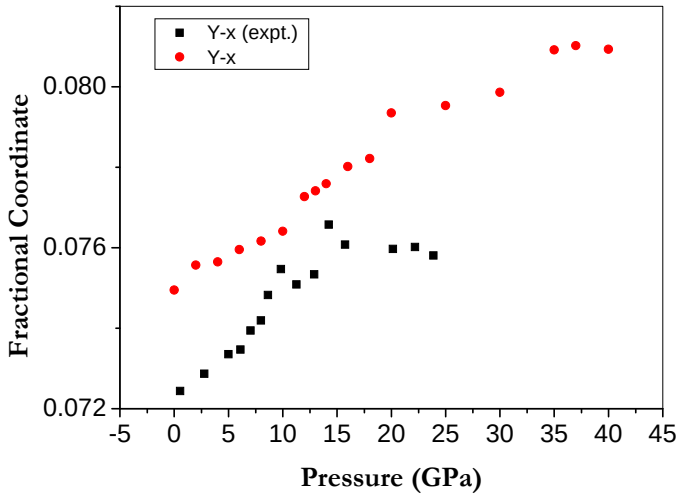

Figure 3-17. x Fractional coordinates of Y atom in $YTiO_3$.

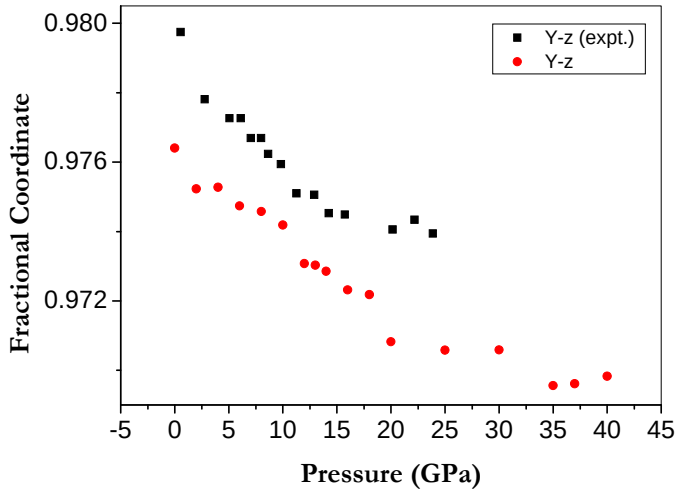

Figure 3-18. z Fractional coordinates of Y atom in $YTiO_3$.

The calculated Y-x and Y-z coordinates are shown in Figures 3-17 and 3-18, respectively. As already shown in Table 3-2, the absolute agreement of the calculated and observed positions at zero pressure is excellent and the error is $< 10^{-3}$. At pressures below 13 GPa, the theory reproduces the experimental observation very well showing an increase in Y-x and a decrease in Y-z. However, beyond 13 GPa, the theoretical and experimental results start to deviate. The theory predicts a continuing trend from the

low pressure which is different from the experimental results. Possible explanations for this discrepancy will be discussed later.

We now turn to the comparison of the calculated and observed Ti-O bond lengths. It should be noted that only Ti-O distances were reported in the experimental work and no information has been given on the atomic positions.

As mentioned earlier, the Ti atom is located in the center of a slightly distorted octahedron formed by six oxygen atoms. There are three distinct Ti-O distances, Ti-O1, Ti-O2(a) and Ti-O2(b). The relevant experimental Ti-O distances are shown in figure 3-19. Both Ti-O1 and Ti-O2(a) show the normal behaviour that the interatomic distances should be shorten with increasing pressure. It is significant to point out an anomaly that was observed in the experiment, namely that the Ti-O2(b) distance increases abruptly from 2.00 Å to 2.02 Å at 13 GPa.

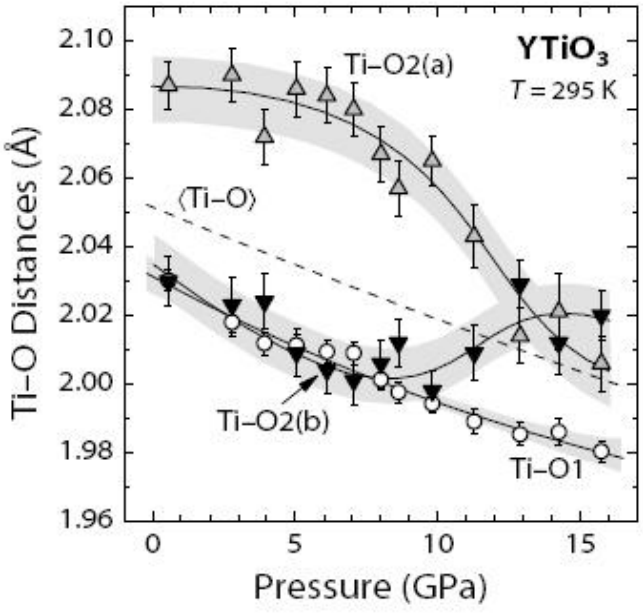

Figure 3-19. Ti-O bond lengths in $YTiO_3$. <Ti-O> denotes the average bond length (from Ref. 26).

The theoretical results reproduce some of the observed trends. The calculated Ti-O bond lengths are shown in Figure 3-20. The Ti-O bond lengths are found to decrease steadily over the pressure range from 0 to 18 GPa. The theory correctly predicts that the Ti-O1 and Ti-O2(b) bonds are almost identical up to 4 GPa. Although the Ti-O2(b) bond distances increase compared to Ti-O1 as revealed in the experiment, they did not lengthen at pressures above 13 GPa. Over the pressure range from 0 to 15 GPa, calculations predict the T-O1 distance shortens by 0.060 Å and the Ti-O2(b) by 0.025 Å.

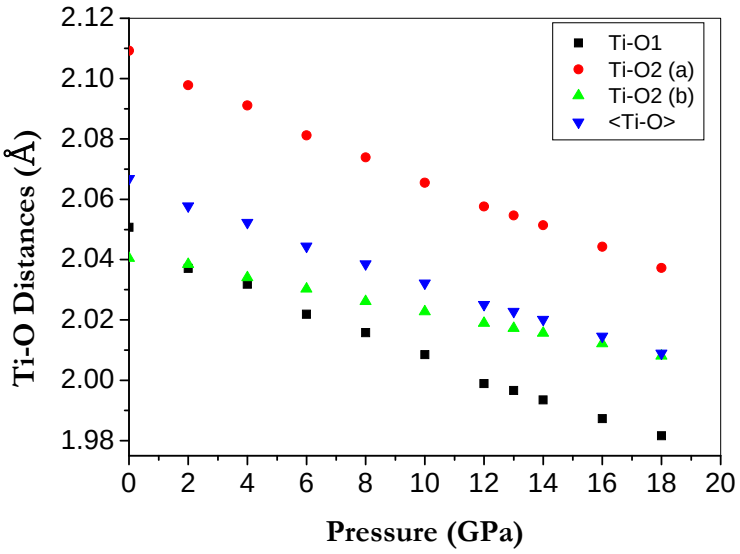

Figure 3-20. Pressure dependence of Ti-O bond lengths in $YTiO_3$. <Ti-O> denotes the average bond length.

It is obvious that the major discrepancy between theory and experiment starts to appear at 13 GPa. We found no sign of possible alternate solutions to the electronic structure calculations at this pressure. We believe the present LDA+U calculations are accurate over the entire pressure range in this study. Therefore, it is not improbable to speculate that the error may arise from the determination of the atom positions from the experimental diffraction pattern. According to the experimental finding [26], the Ti-O2(a) and Ti-O2(b) distances change suddenly at 13 GPa. If this indeed occurs, the Ti 3*d* orbitals have to rehybridize. This would result in a change in the immediate environment around the Ti atom and affect the local symmetry and the crystal field.

The electronic band gap is determined by the crystal field and dependent on electronic transitions from the filled lower t_{2g} to the empty higher t_{2g} states. These transitions should be very sensitive to the crystal field and the local symmetry. No obvious anomaly in the band shape of the infrared spectra was observed near this pressure. As shown in Figure 3-6, the band gap energies continue to follow a smooth downward trend. In the Rietveld refinement of the powder diffraction data, the most crucial input information is the accuracy of the intensities of the Bragg reflections. Moreover, since the method is a multivariate least-squares procedure, the variables to be refined can be highly correlated. Therefore, there are reasonable doubts on possible errors in the refined atomic positions. More experimental and theoretical work may be needed to resolve this discrepancy unambiguously.

In this chapter, the optimal Coulomb repulsion parameter U in the LDA+U method has been determined for $YTiO_3$ at pressures up to 40 GPa. It is found that the U parameter decreases with increasing pressure. This trend can be explained by an increase in the orbital overlaps leading to delocalization of the valence electrons. The metallization pressure for $YTiO_3$ is estimated to be 32 GPa which is in good agreement with the value obtained from extrapolation of the experimental data. The theoretical results fail to detect the anomaly in the structural parameters at 13 GPa. Consequently, no orbital reordering as suggested by the experimental study is observed. Finally, the occupancies of the Ti 3*d* orbitals in $YTiO_3$ were found to change significantly under pressure.

Chapter 4

Electronic Structure of $YTiO_3$ from the Hybrid Functional Method

4.1 Introduction

As discussed in Section 1.6, the hybrid functional method is capable of giving reliable predictions of the band gap energies for a large number of semiconductors. However, this approach has not been thoroughly tested for transition metal compounds. Results of the investigation on the electronic structure of $YTiO_3$ using this method will be presented. From experiment [26], it is known that at ambient pressure $YTiO_3$ is an insulator with a band gap of 0.66 eV (Figure 3-3). The electronic band structure of $YTiO_3$ computed using a standard DFT method is shown in Figure 4-1, which erroneously predicts the ground-state to be a metal. This result reinforces the notion that the DFT is not appropriate for calculation of the band structure of a system with localized *d*-states such as $YTiO_3$.

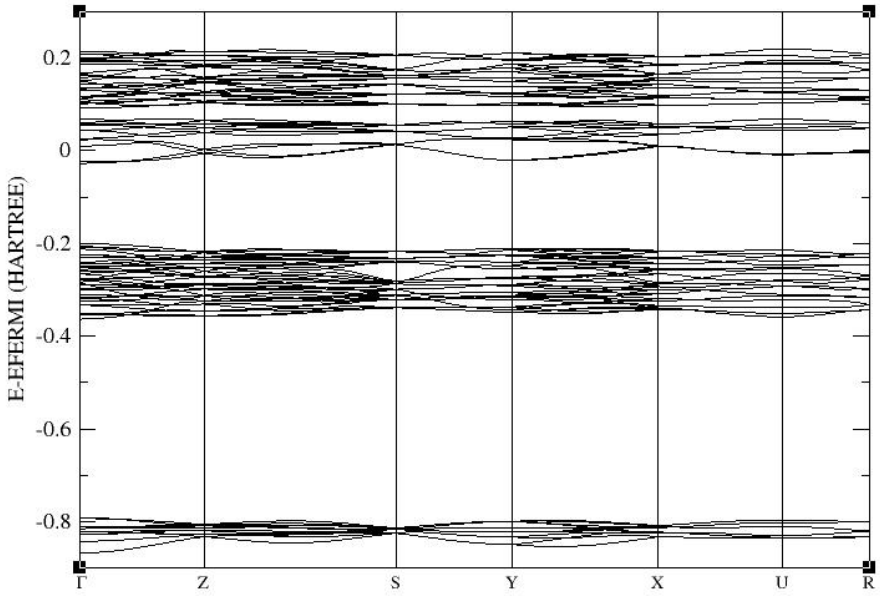

Figure 4-1. Band structure of $YTiO_3$ obtained from spin restricted DFT calculation.

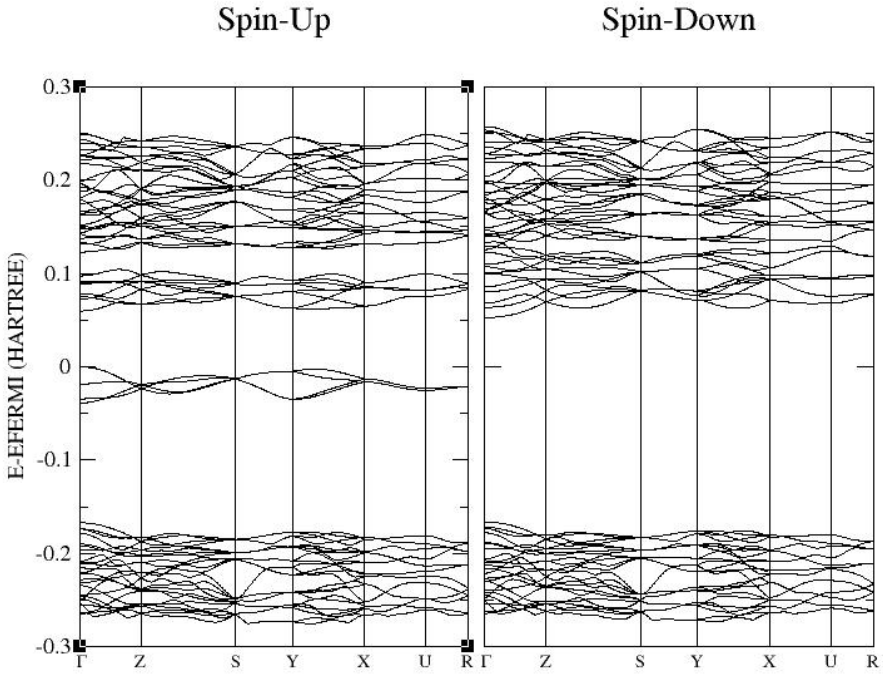

Figure 4-2. Band structure using a hybrid B3LYP functional with spin polarized calculation.

As a prelude for the ensuing investigation, it is instructive to investigate the reliability of the popular B3LYP hybrid functional scheme. Calculations are performed with a localized basis set method on the experimental structure at ambient pressure. The computational details will be provided in a later section. As shown in Figure 4-2, an energy gap is predicted in both the spin-up and spin down states. Therefore, the correct insulator electronic structure is recovered with the hybrid B3LYP functional. Moreover, the narrow band of the spin-up state from -0.04 to 0 Hartree (1 Hartree = 27.2 eV) is found to be predominantly Ti 3*d*. This result is in complete agreement with the LDA+U calculations reported in the preceding chapter. Thus, the hybrid functional method indeed successfully captures the essential physics of the system. However, upon careful examination, the predicted band gap of 1.46 eV (Figure 4-2) is still too large compared to experiment. Even though the first result is promising, the standard B3LYP scheme is not sufficiently reliable and still seriously overestimates the band gap energy. This indicates that more exchange-correlation energy contributions are needed to mix with the Hartree-Fock component. In this chapter, results on the search for an optimal mixing ratio of the Hartree-Fock and exchange-correlation functionals of $YTiO_3$ under pressure will be reported. The resulting electronic band structure will be discussed in light of the calculated DOS and band structures.

4.2 Computational Details

A localized basis set program CRYSTAL [47] was used in this study. As previously mentioned, a localized basis set facilitates the calculation of the HF exchange and Coulomb integrals which are needed in the hybrid functional approach. The CRYSTAL program computes the electronic structure of periodic systems within HF, density functional or various hybrid functional approximations. The program employs a local basis set of Gaussian-type functions to construct the sets of Bloch functions in which the one-electron crystalline orbitals are expanded. The crystalline

orbitals (CO) are treated as linear combinations of Bloch functions (BF), $\phi_\mu(r,k)$, defined in terms of local functions, $\varphi_\mu(r)$ (referred to as Atomic Orbitals, AOs),

$$\Psi_i(r,k) = \sum_\mu a_{\mu i}(k)\phi_\mu(r,k), \tag{4.1}$$

where $a_{\mu i}(k)$ is coefficient and

$$\phi_\mu(r,k) = \sum_g \varphi_\mu(r - A_\mu - g)e^{ik\cdot g}. \tag{4.2}$$

Those local functions are expressed as linear combination of a certain number of Gaussian type functions (GTF),

$$\varphi_\mu(r - A_\mu - g) = \sum_j^{n_G} d_j G(\alpha_j; r - A_\mu - g), \tag{4.3}$$

where the variables are defined in Table 4-1.

r	Coordinate of an electron.
g	Direct lattice vector; the sum over g is extended to the all lattice vectors (infinite) of direct lattice.
k	Lattice vector defining a point in the reciprocal lattice.
A_μ	Coordinate of an atom in the reference cell.
$a_{\mu i}$	Variational coefficients. They multiply the BF; the sum over μ is limited to the number of basis functions.
d_j	Coefficients of the primitive Gaussians in the contraction, fixed for a given basis set.
α_j	Exponents of Gaussians in the contraction.

Table 4-1. Definition of variables.

The coefficients d_j and exponents α_j are defined in the input file. It should be noted that all the electrons, including core and valence, are considered explicitly in the

calculations. Since the Gaussian type basis sets are localized on the atoms, it is quite efficient to compute the relevant Coulomb and exchange integrals. There are fewer variables to be optimized when using a localized basis set as opposed to using the plane wave basis set, and there is no need to invoke the pseudopotential approximation. For $YTiO_3$, the atomic basis sets for Y, Ti and O atoms are taken from the tabulation found in http://www.tcm.phy.cam.ac.uk/~mdt26/crystal.html. The most important factor in a localized basis set calculation is the choice of appropriate basis sets. The basis sets should be flexible enough to correctly reproduce the change of the electron distribution under ambient and high pressure conditions. However, there is always a compromise between the size (or flexibility) of the basis sets and the computational requirements (such as storage, SCF convergence and CPU time). In this study, double zeta valence basis sets augmented with diffuse functions of higher angular momentum are expected to give reasonable results on all properties to be computed.

In view of the large amount of computational resources required, we compute the electronic structure at four selected pressures using the structures determined from previous LDA+U calculations. We have checked this protocol on the structure of $YTiO_3$ at ambient pressure via the calculation of the forces acting on the atoms in the crystal. Even without full geometry optimization, the residual forces are found to be acceptably small.

4.3 Optimal Mixing Parameter for the Hybrid Functional Method

As explained in Section 1.6, the hybrid functional approximation for the exchange-correlation energy E_{xc} is often improved by mixing some exact exchange E_X,

$$E_{XC} = (1 - A)E_X^{LDA} + AE_X^{HF} + E_C^{VWN} \ . \tag{4.4}$$

In equation 4.4, A is the weight of the exact HF exchange. For A = 0, there is no Hartree-Fock exchange term and therefore it is just the pure DFT. For A = 1, there is no LDA term and it corresponds to the pure HF. For the calculations, we have chosen the Dirac-Slater exchange functional [14] and the WVN correlation functional [16].

The procedure in finding the optimal mixing parameter A at a given pressure is similar to the LDA+U calculations. For example, at 0 GPa, to reproduce the experimental band gap energy, trial calculations are performed on the following mixing parameters, 0.13, 0.14, 0.145, 0.15, 0.17, 0.20, 0.40 and 0.80. The resulting band gap energies are plotted against the mixing parameters in Figure 4-3. It is found that when A = 0.145, the hybrid functional calculation gives the same band gap energy of 0.66 eV found from experiment. Therefore at 0 GPa, the optimal hybrid mixing parameter is A = 0.145. In Figure 4-3, it is also shown that the band gap energy increases with increasing mixing parameter. This can be easily understood by considering that the HF method overestimates the band gap. With the increase of mixing parameter, the effect of HF will also increase, thus resulting in an increase of the band gap.

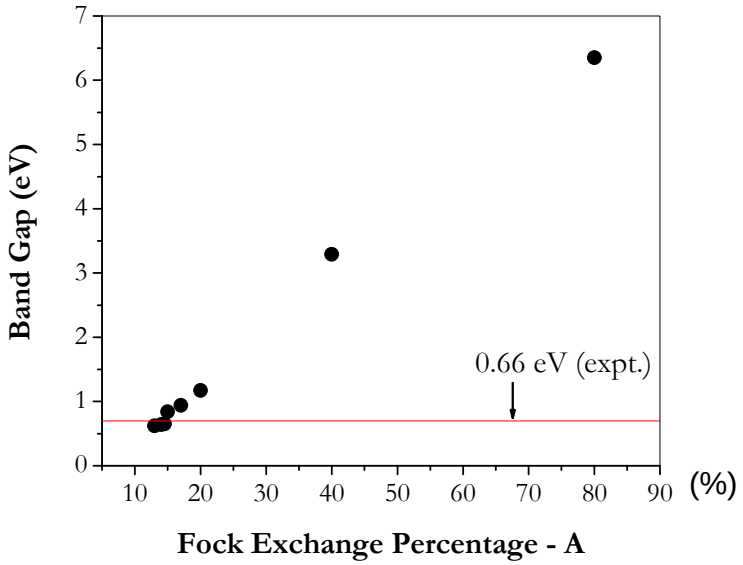

Figure 4-3. Band gaps calculated with different mixing parameters (A) at 0 GPa (horizontal line indicates the experimental bad gap of 0.66 eV).

Similar calculations are performed at 8, 16 and 25 GPa. The results are summarized in Table 4-2.

Pressure (GPa)	**0**	**8**	**16**	**25**
optimal mixing parameter (A)	0.145	0.140	0.130	0.085

Table 4-2. Optimal mixing parameters for $YTiO_3$ at different pressures.

In Table 4-2, it is shown that the optimal mixing parameter decreases with increasing pressure. In other words, the Hartree exchange term becomes less important with increasing pressure. This observation is not unexpected. Similar to the case of the LDA+U method, the on-site Coulomb parameter U becomes smaller as the pressure is increased. Again, the reason is due to the increase in orbital overlap and the system becomes more metallic at high pressure.

The data reported in Table 4-2 are fitted to a third order polynominal relating the optimal mixing parameter A with the pressure P. The expression of the fitted curve is

$$A(P) = 0.145 - 0.00141P + 1.67\times10^{-4}P^2 - 8.57\times10^{-6}P^3 . \qquad (4.5)$$

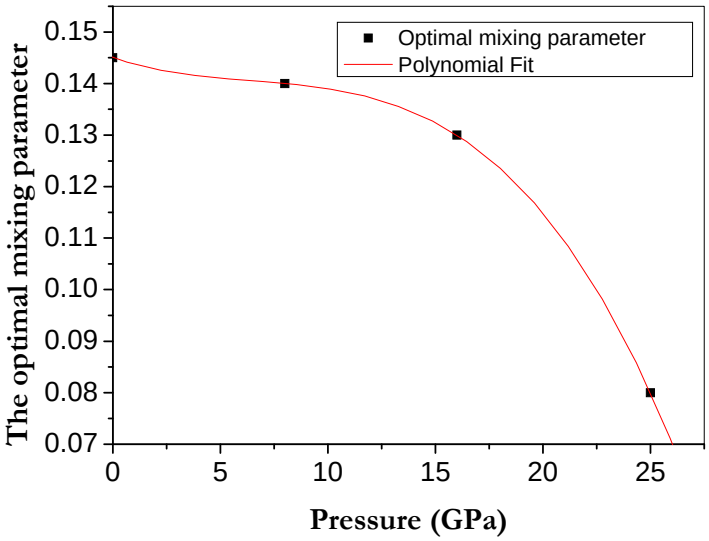

Figure 4-4. Optimal mixing parameters at different pressure.

It is interesting to note that extrapolation of mixing parameter to A = 0 gives a pressure of 31 GPa which is, incidentally, close to the predicted metallization pressure from experiment and from LDA+U calculations.

As mentioned in section 1.2, HF is a mean field theory. Since the HF theory does not contain electron correlation, it often overestimates the band gap energy. The DFT on the other hand includes electron correlation in its theoretical foundation. However, the form of exact exchange-correlation functional E_{XC} is unknown. This is the major obstacle in DFT. In general, DFT tends to underestimate the band gap. Therefore, the hybrid functional method, through the mixing of the appropriate amount of HF exchange and DFT correlation, should be a sound starting point for a good numerical procedure for the accurate prediction of the electronic structure of correlated systems. Unfortunately, as demonstrated here, unlike the highly successful B3LYP

parameterization of the hybrid functional for isolated molecules, there does not appear to be a universal mixing parameter for condensed matter systems. Previous work [1] of Iberio de P.R. Moreira and his collaborators has shown that a mixing parameter of 0.35 is appropriate for several strongly correlated systems. This value, however, failed to reproduce the correct band structure of $YTiO_3$. Drawing on all the experience, a weak conclusion that an optimal mixing parameter for hybrid functionals should be less than 0.35 may be reached.

4.4 Band Structures of High Pressure $YTiO_3$

In Figure 4-5 to 4-8, the calculated band structures of $YTiO_3$ at 0, 8, 16 and 25 GPa, computed with the corresponding optimal mixing parameters, are summarized.

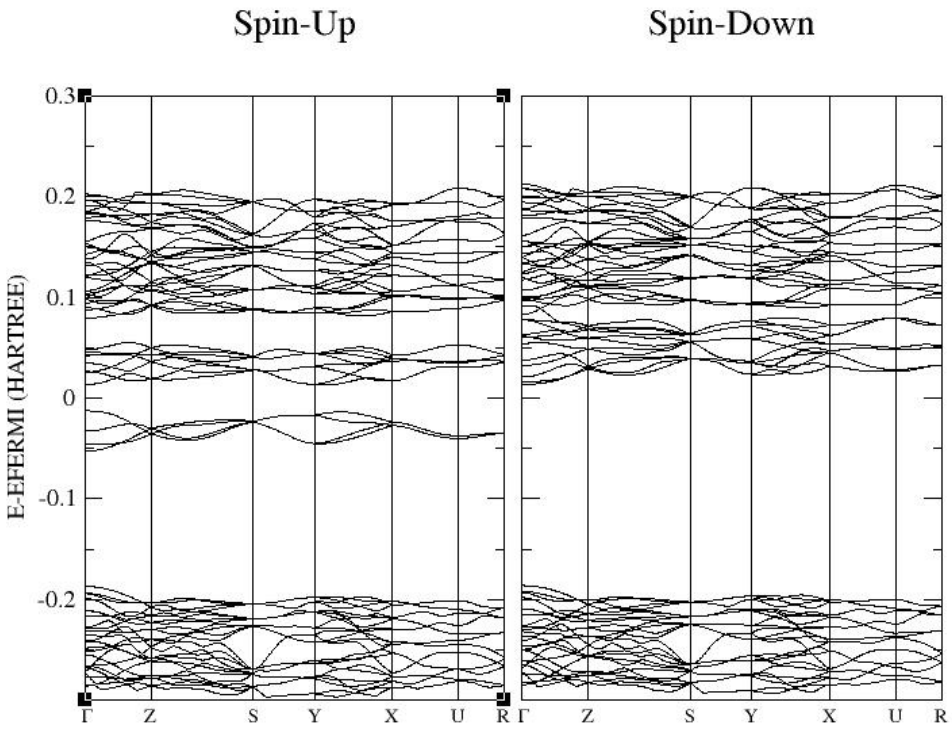

Figure 4-5. Band Structure of $YTiO_3$ using a mixing parameter A = 0.145 at 0 GPa.

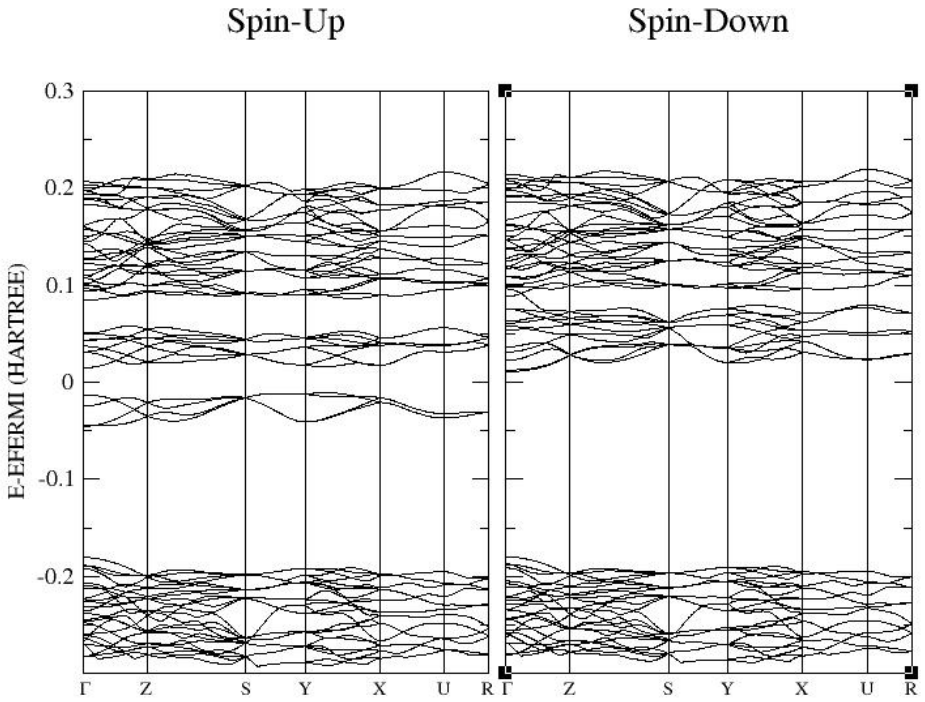

Figure 4-6. Band Structure of $YTiO_3$ using a mixing parameter A = 0.140 at 8 GPa.

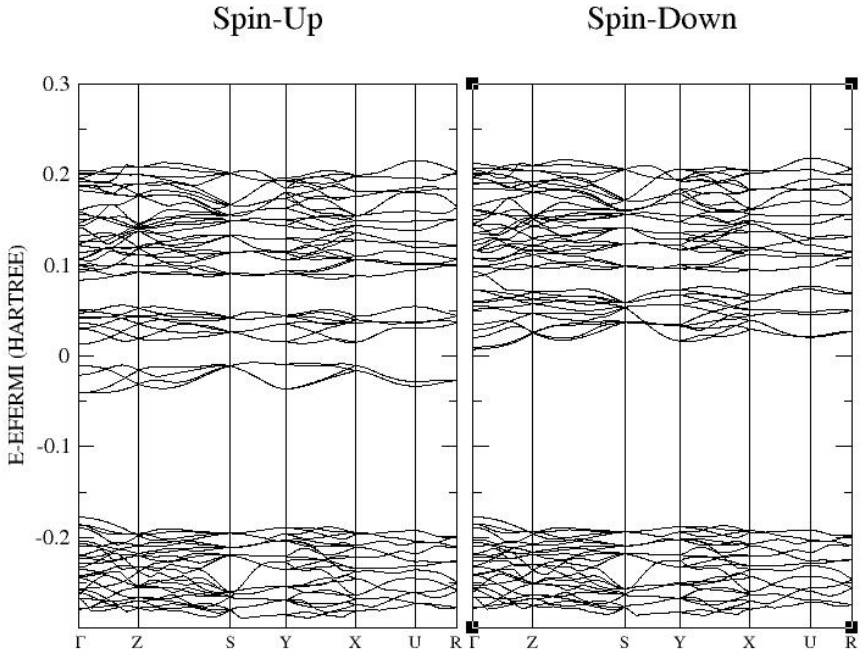

Figure 4-7. Band Structure of $YTiO_3$ using a mixing parameter A = 0.130 at 16 GPa.

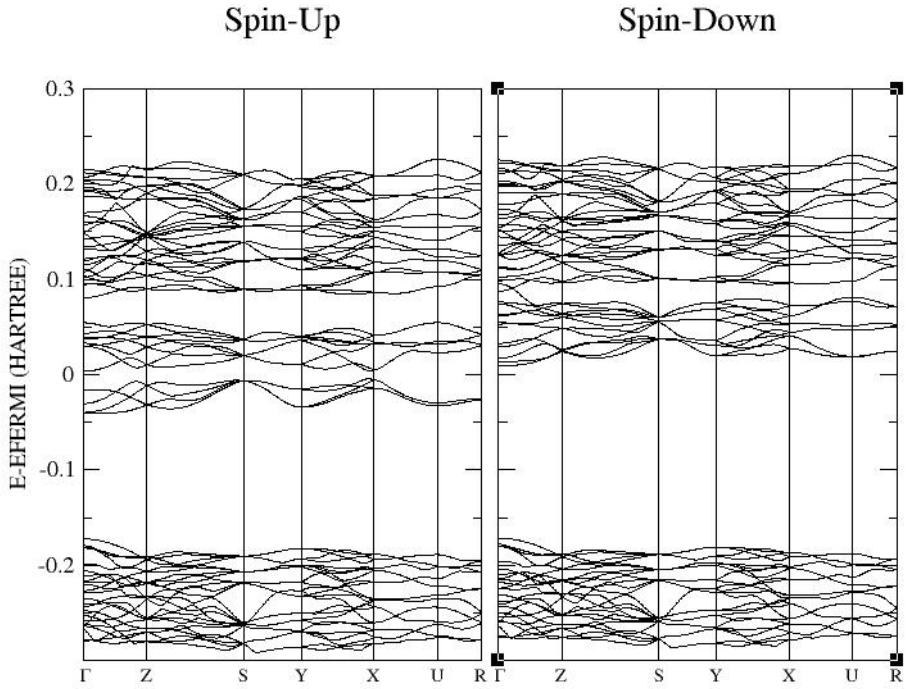

Figure 4-8. Band Structure of $YTiO_3$ using a mixing parameter A = 0.085 at 25 GPa.

The band structures clearly show that, unlike the spin-up states, there are no occupied bands between -0.05 and 0 Hartree in the spin down states. The isolated and narrow electronic band just before the valence band edge (E = 0) in the spin-up states belongs completely to the spin polarized Ti 3*d* orbitals.

Finally, we compare the calculated and experimental band gap energies at 0, 8, 16 and 25 GPa in Table 4-3.

Pressure (GPa)	**0 (A = 0.145)**	**8 (A = 0.14)**	**16 (A = 0.13)**	**25 (A = 0.085)**
Calculated band gap (eV)	0.653	0.542	0.423	0.204
Experiment (eV)	0.660	0.548	0.397	0.201

Table 4-3. A comparison of calculated and experimental band gap energies at different pressures.

A polynomial fit of the calculated band gap energies with pressure is given by

$$E(P) = 0.653 - 0.0159P + 4.12\times10^{-4}P^2 - 1.98\times10^{-5}P^3 . \qquad (4.6)$$

Equation (4.6) can be used to estimate the pressure at the closure of the band gap. The estimated pressure is 31 GPa which is in complete agreement with the experimental result [26] and the result obtained using the LDA+U method.

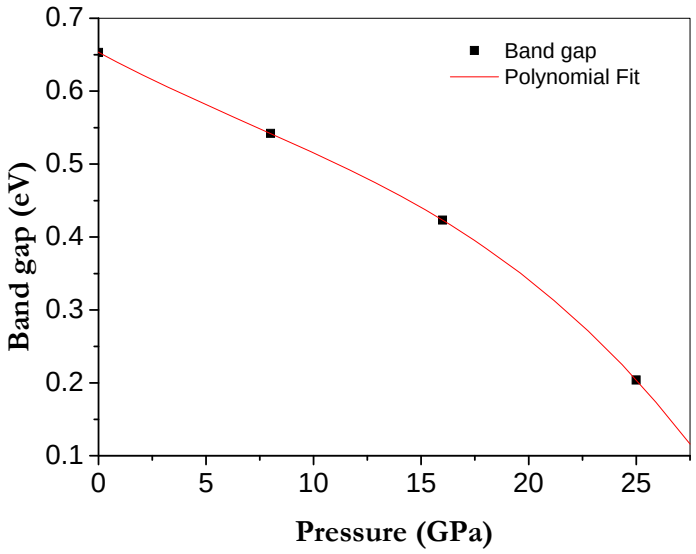

Figure 4-9. Calculated band gap at different pressures.

4.5 Total and Projected Density of States

Similar to the LDA+U calculations, a detailed analysis of the total and projected density of states helps to characterize the nature and the estimation of the occupancy of the relevant orbitals contributing to the valence bands. Figures 4-10 to 4-13 show the total and projected density of states of the Ti 3*d* orbitals at different pressures.

In these figures, the vertical lines indicate the top of the valence bands. From those figures, two bands are found below 0 eV. The Ti-O band is located between -8 and -5 eV. The lower Ti 3*d* t_{2g} band extends from -1.3 eV to the top of the valence band (0 eV). In the Ti-O bonding band, the occupancies of the spin-up and spin-down bands are also identical. The isolated spin-up bands are entirely due to spin-polarized lower Ti 3*d* t_{2g} states.

The general total and projected density of states (PDOS) profiles of the Ti atom obtained by the hybrid functional method are similar to LDA+U method reported earlier. There are subtle differences which will be discussed in the next chapter where the results obtained by both methods are compared. It suffices to say that the Ti 3*d* valence band is relatively narrow (band width is ~1 eV) and is well separated from the Ti-O band by 3 eV. The band width of the Ti-O and Y-O bonding band extends from -5 to -8 eV. This is about 1 eV smaller than the LDA+U prediction.

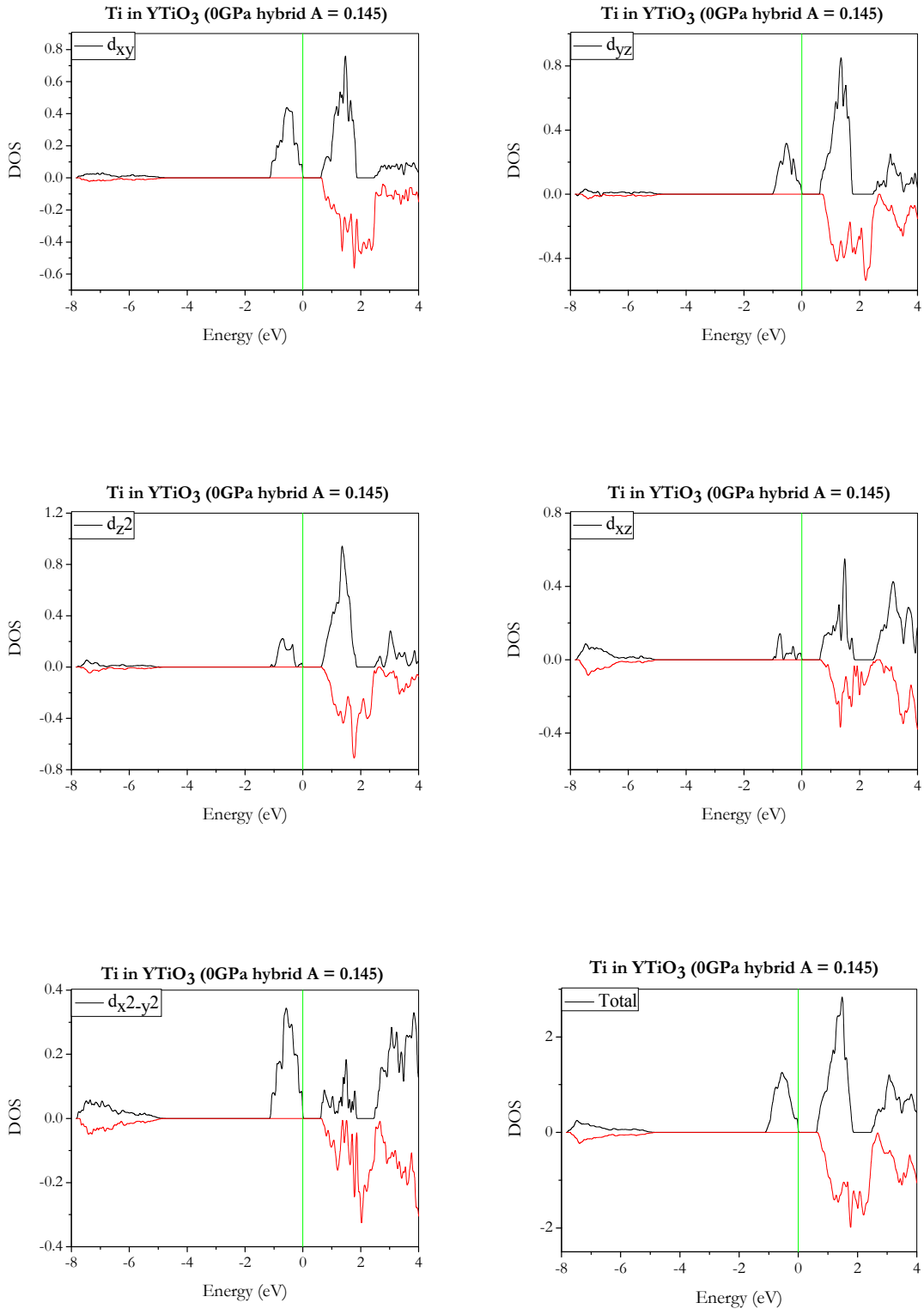

Figure 4-10. PDOS of Ti in $YTiO_3$ at 0 GPa using A = 0.145.

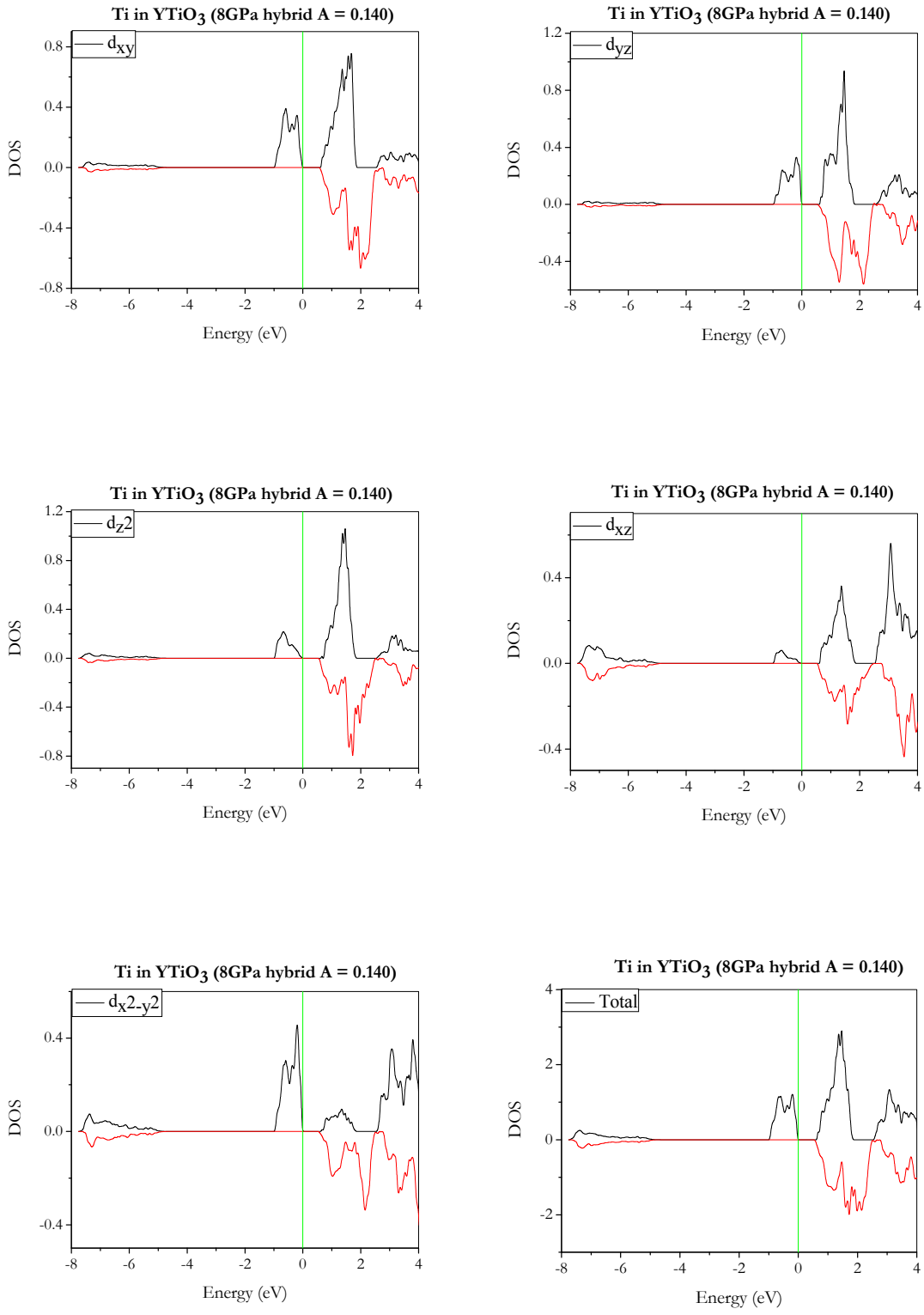

Figure 4-11. PDOS of Ti in $YTiO_3$ at 8 GPa using A = 0.140.

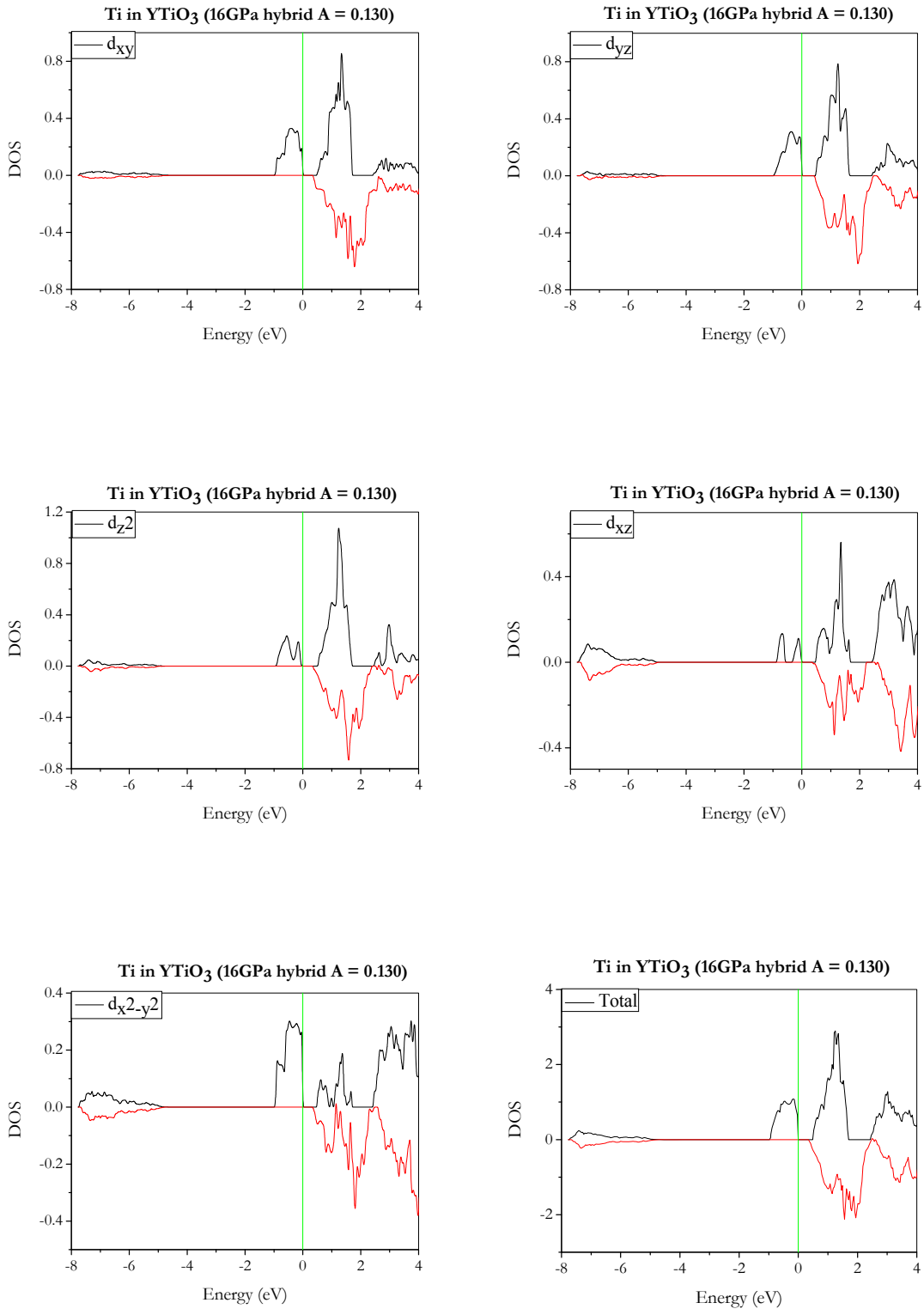

Figure 4-12. PDOS of Ti in $YTiO_3$ at 16 GPa using A = 0.130.

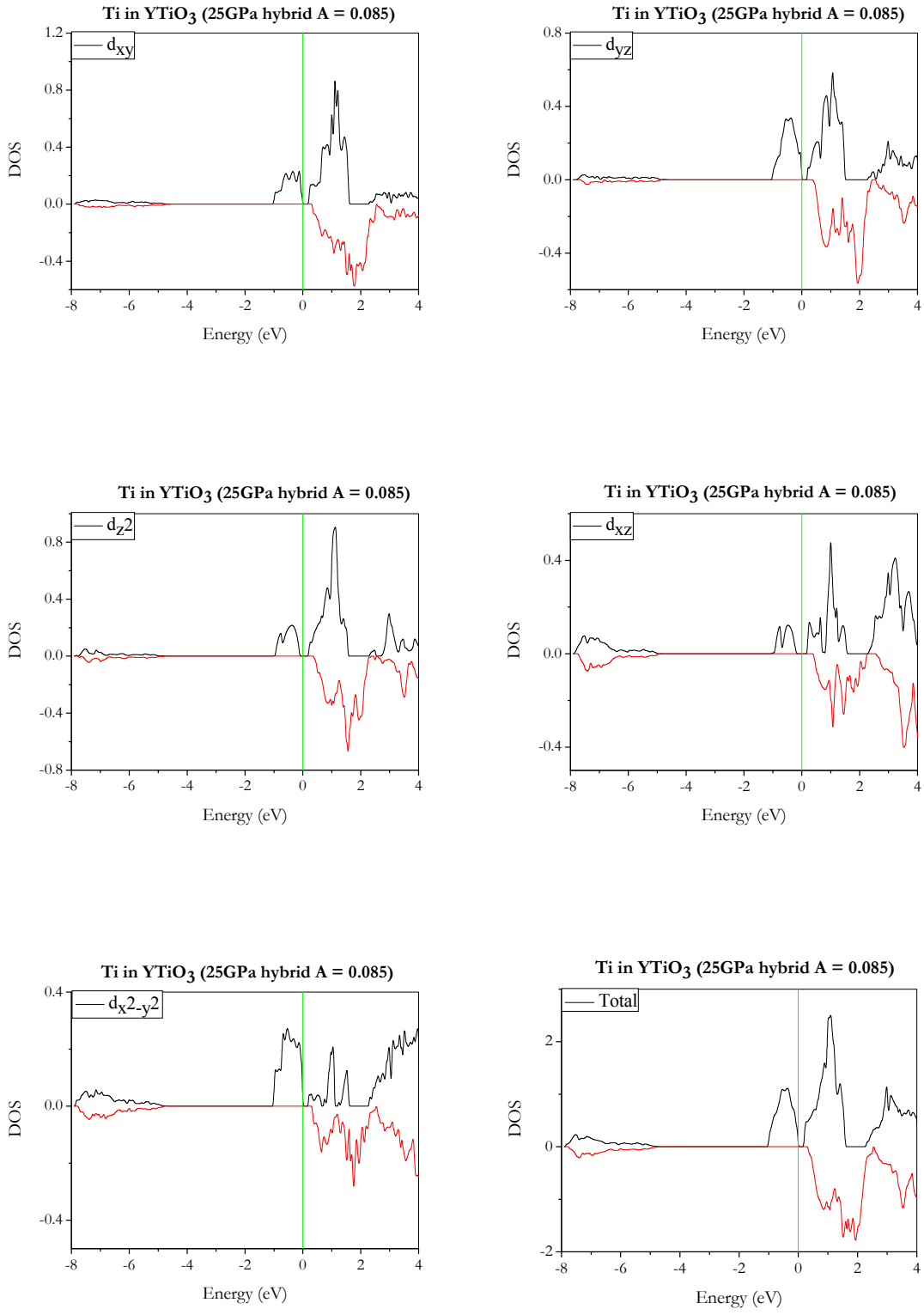

Figure 4-13. PDOS of Ti in $YTiO_3$ at 25 GPa using A = 0.085.

Integrating of the PDOS of the isolated lower Ti 3*d* t_{2g} spin-up band in the energy window from -2 to 0 eV gives the electron occupancies of the individual *d* orbitals. The results at different pressures are shown in Table 4.4.

	0 GPa	**8 GPa**	**16 GPa**	**25 GPa**
d_{xy}	0.263	0.218	0.209	0. 153
d_{yz}	0.160	0.177	0.187	0. 214
d_{z^2}	0.104	0.107	0.112	0.125
d_{xz}	0.043	0.029	0.046	0. 060
$d_{x^2-y^2}$	0.208	0.221	0.212	0. 195
summation	0.778	0.752	0.766	0.747

Table 4-4. Electron occupancy of Ti 3*d* states at different pressures.

From Table 4-4, d_{xy}, d_{yz}, d_{z^2} and $d_{x^2-y^2}$ are the main contributors to the electron occupancies of Ti-*d* bands. The electron occupancy of the d_{xy} orbital decreases with increasing pressure, whereas the electron occupancies of the orbitals d_{yz} and d_{z^2} increase with increasing pressure. The results obtained here are in general agreement with the LDA+U calculation (see Table 3-5).

Chapter 5

Comparison of LDA+U and Hybrid Functional Methods

It is well-known that the two most popular electronic theories, the HF and DFT methods, both have their own shortcomings. In general, HF overestimates the band gap energy but DFT underestimates it. To overcome the problem of emphasizing delocalization of the valence electrons in DFT, we have employed the LDA+U correction. We have also explored the recently proposed hybrid functional method which mixes part HF exchange with part DFT correlation. In this chapter, the performance, efficiency and description of the electronic structure of $YTiO_3$ will be discussed.

The results reported in Chapters 3 and 4 show that, by adjusting the relevant U and A parameters, both the LDA+U and hybrid functional methods can reproduce the observed band gap energies of $YTiO_3$ at different pressures. We have analyzed the electronic structure from the calculated band structures and density of states (PDOS). Here we compare the electronic structures predicted by the two methods in detail.

First, the occupied valence band at 0 GPa, computed with both approaches, is discussed. For convenience, the energy at the top of the valence band is set arbitrarily to 0 eV. As shown in the relevant figures, within the energy window from 0 to -8 eV, there are two distinct bands in the PDOS. The high energy band with a smaller band width is derived mainly from the Ti 3*d* orbitals. The broad and lower energy band can be assigned to Ti-O bonding orbitals. It should be noted that in the methods, there is no

net spin polarization in the Ti-O band as both the spin-up and spin-down band profiles are almost identical. However, the widths of the valence bands are obviously very different. In the LDA+U scheme, the width of the Ti-O band is 3.8 eV. In comparison, the Ti-O width calculated using the hybrid functional method is 3 eV which is 0.8 eV smaller. A broader band width indicates that the "covalency" of Ti-O bonding predicted by the LDA+U method is larger than that of the hybrid functional method. In contrast, the calculated lower Ti 3*d* t_{2g} band width of 0.5 eV by LDA+U is smaller than the 1 eV width obtained by the hybrid functional method. The rather narrow lower Ti 3*d* t_{2g} band predicted by the LDA+U method is a result of the on-site Coulomb repulsion which has a tendency to localize the *d* electrons. On the other hand, the *d* electrons are not as localized as predicted by the hybrid functional method.

It is also noted that the "pseudo-gap" energies, the energy difference from the top of the Ti-O band to the bottom of the Ti 3*d* band, are also quite different between the two approaches. The calculated pseudo-gap in LDA+U is about 2.7 eV, which is 0.9 eV smaller than that obtained from the hybrid functional method of 3.6 eV. A larger band width indicates that stronger Ti-O interactions are predicted by the hybrid functional method. Taken in all, there are quantitative differences in the description of chemical bonding between the LDA+U and hybrid functional methods. The results indicate that the hybrid functional method tends to prefer more ionic Ti-O interactions. This interpretation is consistent with the smaller Ti-O band width and larger Ti 3*d* to Ti-O pseudo-gap energy as compared to the LDA+U. At the same time, the lower Ti 3*d* t_{2g} band obtained from the hybrid functional method seems to experience a larger crystal field since that band width is almost double that predicted by the LDA+U method.

It should be noted that there is insufficient theoretical evidence to unambiguously indicate the reliability of both methods. The theoretical investigation invites further experimental studies, particularly on the measurement of the valence band X-ray photoelectron spectra in order to make a judicial comparison with the calculated density of states.

We now proceed to analyze the lower Ti 3*d* t_{2g} band in more detail. As indicated in the calculation of the PDOS, the lower Ti 3*d* t_{2g} band is nearly 100% spin polarized. The PDOS calculated with the LDA+U method (Figure 3-7) showed that the lower Ti 3*d* t_{2g} band has split into two bands. The splitting, however, is not as clear in the hybrid functional results. Because in $YTiO_3$ the local oxygen arrangement around the Y atom is not ideally octahedral, the formal degeneracy of the t_{2g} band is broken. Furthermore, this splitting is also associated with covalent interaction with the oxygen atoms.

The PDOS of the valence band of $YTiO_3$ under pressures calculated by the LDA+U and hybrid functional methods can be analyzed in a similar manner. A summary of the main results is given in Table 5-1.

Width (eV)	**0 GPa**		**8 GPa**	
	LDA+U	**Hybrid**	**LDA+U**	**Hybrid**
Ti-O	3.8	3	3.6	3
Lower Ti 3*d* t_{2g}	0.5	1	0.5	1
pseudo-gap	2.7	3.6	3	3.7
Width (eV)	**16 GPa**		**25 GPa**	
	LDA+U	**Hybrid**	**LDA+U**	**Hybrid**
Ti-O	4.1	3	4.2	3
Lower Ti 3*d* t_{2g}	0.6	1	0.7	1
pseudo-gap	3	3.7	3	3.6

Table 5-1. Band widths of Ti-O, lower Ti 3*d* t_{2g} and pseudo-gap below the top of valence band.

At 8, 16 and 25 GPa, (see Figure 3-8, 3-10, 3-11, 4-11 ~ 4-13), the widths of lower Ti 3*d* t_{2g} bands are almost constant at 1 eV from hybrid functional calculations. In comparison, the widths of the those bands obtained from LDA+U calculations of 0.5,

0.6 and 0.7 eV at 8, 16 and 25 GPa, respectively, are slightly dependent on the pressure. A similar trend is also observed in the Ti-O band width. The Ti-O band widths are again predicted to be constant at 3 eV from hybrid functional calculations. In comparison, the LDA+U Ti-O widths at 8, 16 and 25 GPa are 3.6, 4.1 and 4.2 eV respectively, showing increasing band width with pressure. It is interesting to note that both methods predict that the "pseudo band gap" between the Ti-O and Ti 3*d* bands remains nearly constant with pressure. The pseudo-gaps at 8, 16 and 25 GPa predicted by LDA+U are 3 eV and those by the hybrid functional are ~ 3.7 eV. From the description above and Table 5-1, it is shown that at 8, 16 and 25 GPa, the hybrid functional calculations predict smaller Ti-O bands and larger pseudo-gaps. Similarly at 0 GPa, the hybrid functional method predicts more ionic Ti-O interactions at higher pressures.

We now turn to the discussion on the electronic structure of the unoccupied (empty) states. In general, the profiles of the PDOS are very similar between the two computational methods. At 0 GPa, from Figures 3-7 and 4-10, the PDOS of the spin-up and spin-down states are not identical. Similar observations are also made at higher pressures. This observation indicates that spin polarization will be very important in the excited states of $YTiO_3$. In the ensuing discussion, we shall focus on the higher Ti 3*d* t_{2g} DOS. The e_g bands are located more than 2 eV above the valence bands and will not be discussed here.

At 0 GPa, the width of the empty Ti 3*d* t_{2g} of spin-up calculated by the LDA+U method is 1.1 eV and the width of higher Ti 3*d* t_{2g} band calculated by the hybrid functional method is 1.2 eV, 0.1 eV larger than the LDA+U method. Furthermore, the empty Ti 3*d* t_{2g} band widths of spin-down are 1.0 eV and 2.0 eV calculated by LDA+U and hybrid functional methods, respectively. The corresponding higher Ti 3*d* t_{2g} band width of spin-down calculated by the hybrid functional method is twice of that calculated by the LDA+U method. At higher pressures, the widths of Ti 3*d* t_{2g} empty bands are given in the Table 5.2.

Width (eV, above band edge)	0 GPa		8 GPa	
	LDA+U	**Hybrid**	**LDA+U**	**Hybrid**
Higher Ti 3*d* t_{2g} (spin-up)	1.1	1.2	1.3	1.2
Higher Ti 3*d* t_{2g} (spin-down)	1.0	2.0	1.1	2.0
Width (eV, above band edge)	**16 GPa**		**25 GPa**	
	LDA+U	**Hybrid**	**LDA+U**	**Hybrid**
Higher Ti 3*d* t_{2g} (spin-up)	1.3	1.2	1.4	1.4
Higher Ti 3*d* t_{2g} (spin-down)	1.2	2.1	1.3	2.2

Table 5-2. Band width of the higher (empty) Ti 3*d* t_{2g} band in the spin-up and spin-down state.

In the LDA+U calculations at 0 GPa, the empty d_{xy} spin-up states split into two bands. Similarly, the spin-down states also split into two bands. The other 3*d* bands (d_{yz}, d_{z^2}, d_{xz} and $d_{x^2-y^2}$) show only one visible peak. In general, the band width of the spin-up state is slightly larger than the spin-down states (see Table 5-2). The hybrid functional calculations gave similar patterns in the Ti 3*d* DOS. However, it is obvious that the higher Ti 3*d* t_{2g} band widths are larger than those predicted by the LDA+U method. The spin-up PDOS of the d_{xy} orbital seems to be composed of a single band. However, the spin-down state splits into two bands as observed in the LDA+U calculation. The remaining Ti 3*d* bands show a structure similar to the corresponding LDA+U calculation.

At 8 GPa, although the hybrid functional predicts that the spin-down band width is larger than that from LDA+U and the spin-up band width is slightly smaller than that from LDA+U, the profiles of the PDOS are very close. In fact, at pressures above 16 GPa, the band profiles of the *d* states from both the LDA+U and hybrid functional methods become more similar. At the highest pressure (25 GPa), the calculated higher

Ti 3*d* t_{2g} band width from the hybrid functional method is much broader; however, the general profiles are still fairly close to that calculated by the LDA+U method.

The unoccupied Ti 3*d* t_{2g} band widths of spin-up calculated from the hybrid functional method are almost constant at 1.2 eV, as indicated in Table 5-2. The band broadens slightly to 1.4 eV at 25 GPa. The unoccupied Ti 3*d* t_{2g} band widths of spin-up from LDA+U show a gradual increase from 1.1, 1.3, 1.3 and 1.4 eV at 0, 8, 16 and 25 GPa, respectively. In conclusion, this is only a very slight difference in the unoccupied Ti 3*d* t_{2g} band widths of spin-up calculated by the LDA+U and hybrid functional methods at all pressures.

Tables 3-5 and 4-4 summarize the Ti 3*d* occupancies. The general trend is very similar between the LDA+U and hybrid functional methods. The d_{xy}, d_{yz} and $d_{x^2-y^2}$ are the main contributors to the occupation of the Ti 3*d* t_{2g} set. The total Ti 3*d* occupancy is around 0.7 *e*. The difference in the absolute values calculated from LDA+U and hybrid functional methods is very slight and can be attributed to the different *k*-point sets and integration schemes used. In LDA+U method, the tetrahedron integration method is used while the Fourier-Legendre interpolation scheme is used in the hybrid functional method [48].

From the description given above, it is shown that even though both the LDA+U and hybrid functional methods can reproduce the band gaps of $YTiO_3$, details of the electronic structure and the description of the chemical bonding are quite different. The LDA+U method seems to favour a larger degree of covalency. The hybrid functional method, on the other hand, favours more ionic bonding. Results from this investigation inevitably lead to the question - since the description of the chemical bonding is dependent on the method of calculation, which method is more reliable? So far we have only limited experimental results – the measured band gap energies as a reference. There is no sufficient experimental evidence in the literature on $YTiO_3$ and, as a matter of fact, on other systems to make an informed and judicial selection of either method. However, the experience gained in this investigation clearly shows that LDA+U is a

much more computationally efficient method than the hybrid functional method. The evaluation of Coulomb and exchange integrals which are needed in the exact exchange formalism demands substantial computational resources on disk storage, memory size and CPU time. Moreover, the self-consistent convergence scheme used in the hybrid functional calculations needs to greatly improve in order to be competitive with the plane wave method used in the LDA+U method.

Chapter 6

Summary and Perspectives

To give an overview on the state of the art on the treatment of correlation effects, the archetypal case of NiO is briefly discussed here. To illustrate the difference in predicting the electronic band gap, the Ni (3*d*) and O (2*p*) electron density of NiO calculated by LDA (b) [49], LDA+U (a) [49], HF (d) [50] and B3LYP (hybrid functional (c)) [51] are shown in Figure 6-1. NiO has an antiferromagnetic ground-state. Therefore the DOS can be divided into spin-up (α) and spin-down (β) components. It is obvious the LDA predicted band gap is very small (0.4 eV). Furthermore, the width of the t_{2g} orbitals situated at the top of the valence band is only 3 eV which is very small. In comparison, the $t_{2g} - e_g$ separation predicted by the HF method is almost 19 eV (0.7 Hartree in Figure 6-1 (d))! The predicted energy gap is obviously too large. Moreover, the t_{2g} band width is approximately 9 eV which is in serious disagreement with the LDA result. On the other hand, the calculated LDA+U DOS is very different from the LDA result. Using a U of 8.0 eV, the calculated band gap has increased to 3.4 eV, while the width of occupied Ni 3d band increased to 7 eV. The hybrid B3LYP functional method reduces the band gap substantially from the HF value. The calculated band gap of 4.2 eV is in closer agreement with the LDA+U prediction. The calculated occupied Ni 3*d* band width of 7.7 eV is also close to the LDA+U result. However the band profiles of DOS calculated by the LDA+U and B3LYP methods are not exactly the same. This indicates that details of the electronic structure predicted by both methods are not identical.

In photoemission experiment [52], the width of the valence band is reported to be about 7.5 eV. Combining the data obtained from reverse photoelectron spectroscopy, the band gap was estimated to be about 4.3 eV [53]. Evidently, both LDA+U and B3LYP calculated band gaps are in better agreement with experiment over their LDA and HF counterparts. However, the agreement is still not quantitative. Incidentally, a similar pattern also emerges from the present study on $YTiO_3$ as will be briefly discussed below.

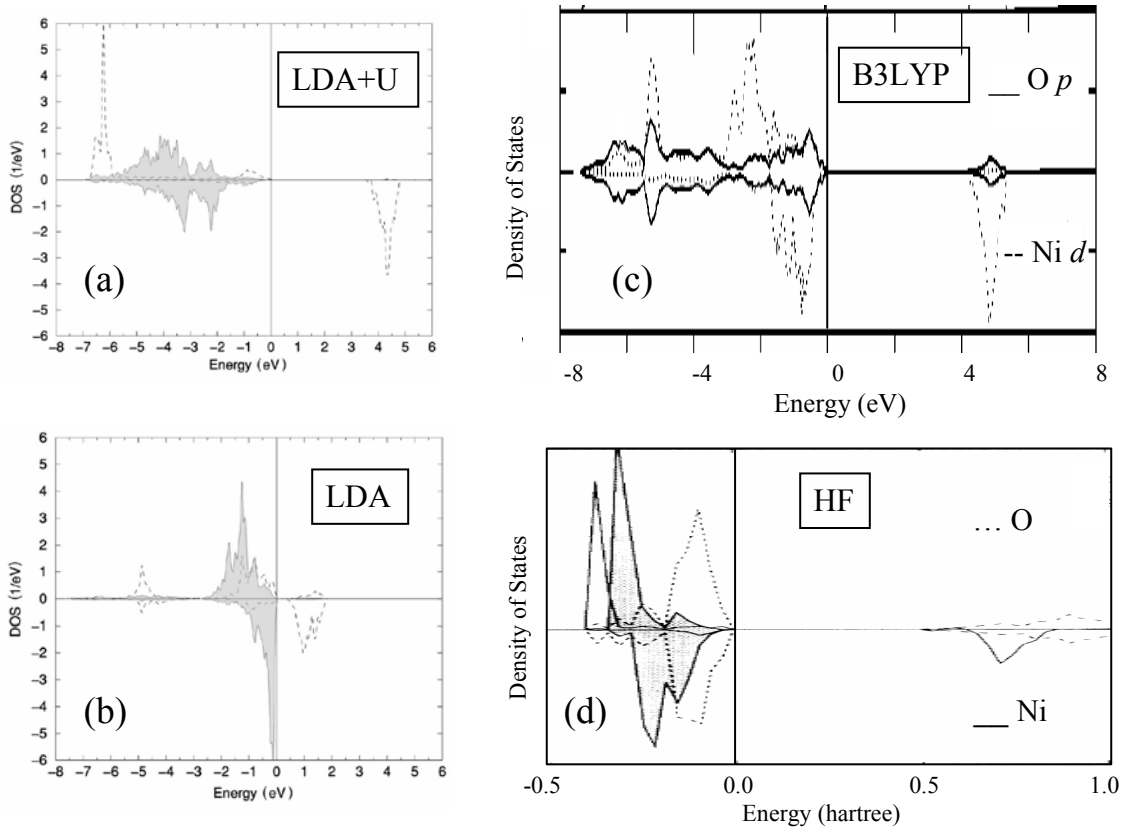

Figure 6-1. PDOS of NiO for (a) LDA+U, (b) LDA, (c) B3LYP and (d) HF.

In this work, two theoretical methods have been investigated, i.e., the LDA+U and hybrid functional methods, for the description of electronic structure of highly correlated system using $YTiO_3$ as a model system. The project is motivated by recent accurate experimental band gap energy measurements by synchrotron IR (infrared) and structure determination from X-ray powder diffraction and the suggestion of a novel

orbital reordering transition at high pressure. In addition, several computational studies using different theoretical techniques are already available for comparison. To achieve this goal, we have performed extensive calculations using these two methods.

We found that the experimental band gap can be reproduced by varying the appropriate U and A parameters in LDA+U and hybrid functional methods, respectively. However, details of the electronic structure are quite different between the LDA+U and hybrid functional calculations indicating there are significant differences in the description of the nature of chemical bonding. Moreover, fully geometry optimized LDA+U calculations failed to reproduce the anomaly observed in the experimental structure at 13 GPa [26]. We conclude that there is no orbital reordering transition in $YTiO_3$.

A conclusive evaluation on the reliability of the LDA+U and hybrid functional methods cannot be reached in this investigation mainly due to a lack of experimental information for direct comparison. This investigation, however, invites future experimental studies on the electronic properties of $YTiO_3$ and other related systems. For example, the recent advances in charge-compensation in the detection of photoelectrons from insulating systems enable accurate measurements of the valence band from X-ray photoelectron spectra [54]. These spectra are invaluable for the direct comparison with the calculated electronic density of states of the occupied bands. For the characterization of empty states, X-ray photoemission experiments will be most useful. On the theoretical aspect, a future direction is to explore new methods for the *ab initio* prediction of the U parameter. Higher level approximations like the DMFT maybe a good model to treat correlation effects. This method is still under development and many things need to be understood before the method can be employed for general computation.

In conclusion, this is an ambitious research project. The validation of an efficient and easily implemented computational method for accurate prediction of the electronic structure and electronic properties of transition metal oxides will be a valuable

contribution to the computational physics and material science communities. Results reported here make the essential first step and a small contribution to the continuing efforts in this direction.

References

[1] I. de P.R.Moreira, F. Illas, and R.L. Martin, Phy. Rev. B 65, 155102 (2002).

[2] J. Muscat, A. Wander and N.M. Harrison, Chem. Phys. Lett. 342, 397 (2001).

[3] A. Szabo and N.S. Ostlund, Modern Quantum Chemistry, Wiley (1989)

[4] E. Schrödinger, Ann. Phys. (Leipzig) 78, 489 (1926).

[5] D.R. Hartree, Proceedings of the Cambridge Philosophical Society, 24, 89 (1927-28).

[6] V.A. Fock, Z. Physik 61, 126 (1930).

[7] J.C. Slater, Phys. Rev. 34, 1293 (1929).

[8] L.H. Thomas, Proc. Cambridge Phil. Roy. Soc. 23, 542 (1927).

[9] E. Fermi, Rend. Acad. Naz. Lincei 6, 602 (1927).

[10] P. Hohenberg and W. Kohn, Phys. Rev. 136, B864 (1964).

[11] R.M. Martin, Electronic Structure – Basic Theory and Practical Methods, Cambridge University Press, P123-125 (2004).

[12] W. kohn and L.J. Sham, Phys. Rev. 140, A1133 (1965).

[13] P.A.M. Dirac, Proc. Cambridge Phil. Soc., 26, 376 (1930).

[14] J.C. Slater, Phys. Rev. 81, 385 (1951).

[15] E. Wigner, Phys. Rev. 46, 1002 (1934).

[16] S. Vosko, L. Wilk and M. Nusair, Can. J. Phys. 58, 1200 (1980).

[17] D.M. Ceperley and B.J. Alder, Phys. Rev. Lett. 45, 566 (1980).

[18] J.P. Perdew and A. Zunger, Phys. Rev. B 23, 5048 (1981).

[19] J.P. Perdew, K.Burke and M. Ernzerhof, Phys. Rev. Lett. 77, 3865 (1996).

[20] A.I. Liechtenstein, V.I. Anisimov and J. Zaanen, Phys. Rev. B 52, R5467 (1995).

[21] M. Cococcioni and S. de Gironcoli, Phys. Rev. B 71, 035105 (2005)

[22] A.D. Becke, J. Chem. Phys. 98, 1372 (1993).

[23] A.D. Becke, J. Chem. Phys. 88, 1053 (1988).

[24] A.D. Becke, J. Chem. Phys. 98, 5648 (1993).

[25] Perger W.F., Chem. Phys. Lett. 368, Number 3, 319 (2003).

[26] I. Loa, X. Wang, K. Syassen, H. Roth, T. Lorenz, M. Hanfland and Y.L. Mathis,

cond-mat/0504383 (2005).

[27] H. Fujitani and S. Asano, Phys. Rev. B 51, 2098, (1995).

[28] H. Sawada and K. Terakura, Phys. Rev. B 58, 6831, (1998).

[29] H. Sawada, N. Hamada and K. Terakura, Physica B 237, 46 (1997).

[30] E. Pavarini, S. Biermann, A. Poteryaev, A.I. Lichtenstein, A. Georges, and O.K. Andersen, Phys. Rev. Lett. 92, 176403 (2004).

[31] R. Hoffmann, Solids and Surfaces: A Chemist's View on Bonding in Extended Structures, VCH Publishers, Inc. (1988).

[32] H. Bethe, Ann. Physik, 5, 325 (1929).

[33] J.H. Van Vleck, Phys. Rev. 41, 208 (1932).

[34] J.H. Van vleck, J. Chem. Phys. 3, 803 (1935).

[35] F.A. Cotton, J. Chem. Educ. 41, 466 (1964).

[36] C.C. J. Roothaan, Rev. Mod. Phys. 23, 69 (1951).

[37] G.G. Hall, Proceedings of the Royal Society, London, A205, 541 (1951).

[38] J.A. Pople and R.K. Nesbet, J. Chem. Phys. 22, 571 (1954).

[39] T. Tsuchiya, R.M. Wentzcovitch, C.R.S. da Silva and S. de Gironcoli, Phys. Rev. Lett. 96, 198501 (2006).

[40] P.E. Blochl, Phys. Rev. B 50, 17953 (1994).

[41] G. Kresse and D. Joubert, Phys. Rev. B 59, 1758 (1999).

[42] M.C. Payne, M.P. Teter, D.C. Allan, T.A. Arias and J.D. Joannopoulos, Rev. Mod. Phys. 64, 1045 (1992).

[43] D. Vanderbilt, Phys. Rev. B 41, 7892 (1990).

[44] D.A. Maclean, H. NG, and J.E.Greedan, J. Solid State Chem. 30, 35 (1979).

[45] E. Pavarini, A. Yamasaki, J. Nuss, and O.K. Andersen, N.J.Phys. 7, 188 (2005).

[46] S. Okatov, A. Poteryaev and A. Lichtenstein, Europhys. Lett. 70 (4), 499 (2005).

[47] C. Pisani, R. Dovesi and C.Roetti, 48, Hatree-Fock Ab Initio Treatment of Crystalline Systems, Springer-Verlag Berlin Heidelberg (1988).

[48] P.M.W. Gill, B.G. Johnson and J.A. Pople, Chem. Phys. Lett. 209, 506-512 (1993).

[49] A.B. Shick, A.I. Liechtenstein and W.E. Pickett, Phys. Rev. B 60, 10763 (1999).

[50] M.D. Towler, N.L. Allan, N.M. Harrison, V.R. Saunders, W.C. Mackrodt and E. Aprà, Phys. Rev. B 50, 5041 (1994).

[51] X.B. Feng and N.M. Harrison, Phys. Rev. B 69, 035114 (2004).

[52] V.I. Anisimov, I.V. Solovyev, M.A. Korotin, M.T. Czyż yk and G.A. Sawatzky, Phys. Rev. B 48, 16929 (1993).

[53] N.F. Mott, Metal-Insulator Transitions (Taylor and Francis, London, 1974).

[54] V.P. Zakaznova-Herzog, H.W. Nesbitt, G.M. Bancroft, J.S. Tse, X. Gao and W. Skinner, Phys. Rev. B 72, 205113 (2005).